TRACING VISUAL AND ACOUSTIC SIGNATURES OF MECHANICAL BEHAVIOR OF COMPOSITE MATERIALS

by
BENGISU YILMAZ

Submitted to the Graduate School of Engineering and Natural Sciences
in partial fulfillment of
the requirements for the degree of
Master of Science

Sabanci University

January 2017

TRACING VISUAL AND ACOUSTIC SIGNATURES OF MECHANICAL BEHAVIOR OF COMPOSITE MATERIALS
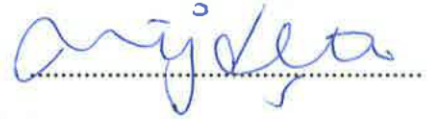
APPROVED BY:

Assoc. Prof. Dr. Melih Papila

(Thesis Advisor)

Assoc. Prof. Dr. Gullu Kiziltas Sendur

(Thesis Co-advisor)

Assoc. Prof. Dr. Mujdat Cetin

Assoc. Prof. Dr. Demirkan Coker

Assist. Prof. Dr. Elif Ozden Yenigun

DATE OF APPROVAL: 06/01/2017

Nothing in life is to be feared, it is only to be understood.
Now is the time to understand more, so that we may fear less.

Marie Sklodowska-Curie

to my family...

ACKNOWLEDGEMENTS

TRACING VISUAL AND ACOUSTIC SIGNATURES OF MECHANICAL BEHAVIOR OF COMPOSITE MATERIALS

Bengisu YILMAZ

M.Sc. Thesis, January 2017

Thesis Advisor: Assoc. Prof. Melih PAPILA

Thesis Co-Advisor: Assoc. Prof. Gullu KIZILTAS SENDUR

ABSTRACT

Fiber-reinforced advanced composite materials are widely used in applications of various engineering fields such as aerospace, marine, transportation, and energy. They offer high stiffness and strength along with substantial weight saving potential and allow intriguing design options for superior performance. Despite their remarkably growing use and adaptation into engineering design, the complexity of mechanical behavior of the composite materials, in particular strength and failure, is still a challenge leading to broadening research efforts. This thesis is an effort to address how composite engineers can associate the material characteristics and mechanical behavior of composites using visual and acoustic imaging/recording. Two case studies of structural laminated composites exemplify the potential use of the information obtained specifically from, micro-computed tomographic imaging and general purpose microphone recordings supplemented by video microscopy to seek their correlations with the traditional mechanical test data.

The first case focused on the effect of meso-architectural, self-arrangement of fiber bundles with different yarn numbers on the mechanical behavior of non-crimp glass

fiber reinforced composites. The visual inspection of anomalies (like the void presence) and in-situ deviations from ideal yarn structures are characterized by using micro-focus computed tomography. Results reveal that the yarn number is directly affecting the tensile behavior of composites in terms of bundle/inter-bundle size, micro-void presence, waviness, and crimping.

The second case study aims to show how basic mechanical testing can be supplemented by a general purpose noise reducing microphone and video microscope. The method is simple, affordable, easy to incorporate, yet capable of collecting useful information. The acoustic signatures of the six different cross-ply orthotropic carbon fiber reinforced composites are investigated. In-situ characterization of the progressive failure events is presented as minor, intermediate, major and ultimate with unique sound profiles.

KOMPOZİT MALZEMELERİN MEKANİK DAVRANIŞLARININ GÖRSEL VE AKUSTİK İZLERİNİN İNCELENMESİ

Bengisu YILMAZ

Yüksek Lisans Tezi, 2016

ÖZET

Elyaf takviyeli ileri kompozit malzemeler; havacılık, denizcilik, ulaşım ve enerji gibi çeşitli mühendislik alanlarında yaygın olarak kullanılmaktadır. Yüksek sertlik ve mukavemet gösteren ileri kompozit malzemeler, olası ağırlık avantajları ile yüksek performanslı sıradışı tasarımlara olanak sağlarlar. Mühendislik tasarımlarındaki kullanım ve adaptasyon oranlarındaki dikkate değer artışa rağmen, bu malzemelerin karmaşık mekanik davranışları, özellikle mukavemet ve kırılım, halen araştırma çabalarını genişleten bir konudur. Bu tez çalışması kompozit mühendislerinin, kompozit malzemelerin karakteristik özelliklerini ve mekanik davranışlarını görsel ve akustik görüntüleme / kayıt yöntemleri ile nasıl ilişkilendirebileceği üzerine bir çabadır. Yapısal kompozitlerin mekanik özelliklerini incelemek için iki vaka çalışması yapılmıştır. İlk vaka çalışmasında mikro-bilgisayarlı tomografi görüntülerinin, ikinci vaka çalışmasında ise video mikroskopi destekli mikrofon kayıtlarının geleneksel mekanik test verileri ile, korelasyonları incelenmişlerdir.

İlk vaka çalışması, farklı iplik numaralı elyaf demetleri ile düzenlenmiş lamine kompozitlerin mezo-yapılarının mekanik davranış üzerindeki etkilerine odaklanmıştır. Özellikle, hasar almamış kıvrımsız cam-elyaf ile güçlendirilmiş kompozitlerin mikro ve mezo ölçekteki anomalileri mikro-bilgisayarlı tomografi ile araştırılmıştır. Üç boyutlu görüntülerin incelenmesi ile anomalilerin miktarının, kıvrımsız elyaf demetlerinin

boyutunun ve demet arası boşlukların etkisinin mekanik davranışlarını yoğun şekilde etkilediği gözlenmiştir.

İkinci vaka çalışması, temel mekanik testin genel kullanım düşük gürültülü mikrofon ile video mikroskopunun nasıl desteklenebileceğini göstermeyi amaçlamaktadır. Önerilen yöntem basit, kolayca kullanılabilir ve düşük maliyetli olmasının yanı sıra yararlı bilgileri kaydedebilme yetisine sahiptir.Altı farklı çapraz katlı ortotropik karbon elyaf destekli kompozitin mekanik davranış/kırılma gösterici akustik işaretleri, test sırasında kaydedilen ses verileri ve dijital mikroskop görselleri yardımı ile kademeli kırılma mekanizmalarını karakterize etmek için kullanılmıştır. Mekanik test sırasındaki kademeli kırılma olayları, kendine has ses profilleri ile korelasyonlu olarak, küçük, orta, büyük ve nihai olarak karakterize edilmiştir.

LIST OF SYMBOLS AND ABBREVIATIONS

∥	Loading direction parallel to the material coordinate system
⊥	Loading direction is transversal to the material coordinate system
µCT	Micro-focus computed tomography
0º	Degree of orientation of fiber which is parallel to the material coordinate system
2D	Two dimensional
3D	Three-dimensional
90º	Degree of orientation of fiber which is transversal to the material coordinate system
ACFM	Alternating current field measurement
AE	Acoustic Emission
DIC	Digital image correlation
EC	Eddy current testing
EM	Electromagnetic methods
EN	Euler number
f_{max}	Maximum frequency
f_s	Sampling frequency
Hz	Hertz (SI dimension of frequency -one cycle per second)
kHz	Kilohertz
kV	Kilo-volt
mA	Mili-ampere
MFL	Magnetic flux leakage
MHz	Megahertz
MIL	Mean intercept length
MPa	Mega-pascal
NCF	Non-crimp fiber
NDT	Non-destructive testing
RFT	Remote field testing
ROI	Region of interest
TEX	The weight in grams of a kilometer of yarn

UD   Unidirectional

V_f Fiber volume fraction inside composite materials

VOI   Volume of interest

VT/VI   Visual testing / Visual Inspection

XCT   X-ray based computed tomography

CONTENTS

LIST OF FIGURES

xvi

LIST OF TABLES

1 INTRODUCTION

1.1 General Introduction

In various engineering applications, such as aerospace, marine, transportation and energy, fiber-reinforced advanced composite materials are widely used. The advanced composite materials allow engineers to create intriguing designs due to the advantage of high stiffness and strength with critical weight saving potential. Given composites are remarkable engineering materials, the complexity of the mechanical behavior of the composite materials, in particular strength and failure, is still a challenging and growing research area. While emerging technologies in manufacturing allow engineers to make use of composites more reliably and efficiently, characterization techniques help to establish a deeper understanding of their behavior. This thesis is an attempt to address how composite engineers can correlate the material characteristics and mechanical behavior of composites using visual and acoustic non-destructive testing methodologies. In the following chapters, two applications of non-destructive testing for structural laminated composites have been analyzed in order to understand their relationships with conventional mechanical testing.

More specifically, in this study, specimens under tension have been investigated to understand the load transfer behavior through the laminae. Laminated composites are purposely designed with different stacking sequences. The primary focus of the study is to understand the meso-architectural behavior of composites by the help of advanced characterization techniques. Two case studies of structural laminated composites exemplify the potential use of the signatures obtained specifically from, micro-computed tomographic imaging and general purpose microphone recordings

supplemented by video microscopy to seek correlations with the traditional mechanical test data.

The first case focused on the effect of meso-architectural, self-arrangement of fiber bundles of different yarn numbers on the mechanical behavior of laminated composites. Notably, the anomalies of the pre-damaged non-crimp glass fiber-reinforced composites in the micro and mesoscale were investigated via micro-computed tomography. Also, the effect of the mesostructure on pre-damage composites containing five different lay-up sequences was evaluated. The relationships among the anomalies, meso-architecture, the mechanical strength values, and fracture modes were reported. The 3D image analysis shows that the amount of anomalies, the inter-bundle size, and bundle width of the NCF yarns affect the mechanical behavior of the composite laminates. The effect of yarn number and associated bundle packing/interactions on the tensile behavior of non-crimp fiber reinforced laminates is investigated. Four different yarn numbers, representative of fiber linear density, (300, 600, 1200, and 2400 TEX) of glass fiber in the form of unidirectional (UD) non-crimp fabrics (NCF) are analyzed. All the glass fiber UD NCFs have the same ply areal weight of 300 g/m^2. Composite laminates were made by vacuum bagged infusion of vinyl ester resin system into the stacked NCFs. Unidirectional, cross-ply and quasi-isotropic stacking sequences of $(0)_8$, $(0/90)_{2S}$, and $(0/45/-45/90)_S$ respectively, were produced at a fixed fiber volume fractions (V_f) and then evaluated under tensile loading. The meso-architecture of manufactured laminates are analyzed using micro-focus computed tomography (μCT) to further detect the void presence and in-situ deviations from ideal yarn structures (e.g. yarn waviness and crimping). Results reveal that the yarn number is directly affecting the behavior of NCF laminates under tension in terms of bundle/inter bundle size, micro-void presence, waviness, and crimping.

The second case study aims to show how the mechanical behavior of laminated fiber-reinforced composites containing various lay-up sequences is affected under tension. The acoustic signatures of the six different cross-ply orthotropic carbon fiber reinforced composites are investigated to characterize the progressive failure mechanisms by in-situ sound collection in conjunction with a digital video microscope. The progressive failure events during mechanical testing are marked as minor, intermediate, major and ultimate correlated with the unique sound profiles. The simplified method is not a replacement for acoustic emission; while it is capable of rough characterization of failure events.

1.2   The Mechanical Behavior of Fiber Reinforced Composite Materials

To fully understand the physical phenomenon under the mechanical behavior of laminated composites, the crack formation, propagation, and failure modes should be investigated considering their multi-scale nature of these inhomogeneous materials. Because the interaction within the multi-scales is known to play a significant factor in failure and fracture mechanism of composites [1]. In fact, the damage formations and mechanisms for composite materials can be categorized inline with the hierarchical classification of characteristic length scales of the material design. The micro-scale length is typically driven by the reinforcing fibers for which diameter is in micrometers. Their collection of tens and hundreds may also be the focus of micro-scale understanding.   On the other hand, meso-scale typically defines the bundles of thousands of fibers and the reinforcement/filler architecture formed by them within a single layer. Repeated collection of a few layers can also be considered under the class of meso-scale characteristics, e.g. non-crimp fabric (NCF) building blocks. And finally, the macro-scale covers lengths from few millimeters to some meters and is associated with the thickness of the laminate or the full dimensions of the composite structure.   In other words, it is for the laminate which is formed by the number of the meso-scale reinforcing layers.   In accordance with this classification, the characteristics and length scale of damages can be categorized as micro-scale, meso-scale, and macro-scale damage formations and are schematically represented in Figure 1.1.
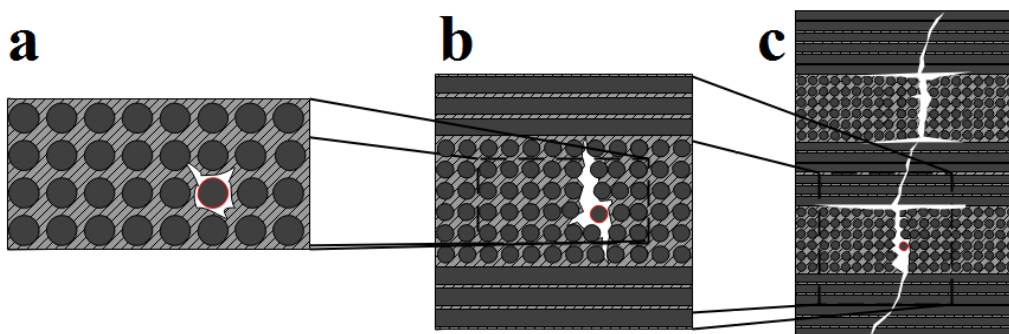
Figure 1.1 From left to right: a) Micro-crack b)Meso-crack c) Macro-crack

One of the key issues in fracture mechanics is the fact that there are always anomalies in real materials. In the case of advanced composite materials, there are also a variety of anomalies or defects that can be associated with the multi-scale characteristics. The most probable anomalies can be listed as voids, fiber undulations, resin-rich regions and misplacements of fibers or fiber bundles inside the composites [2]. They are likely to decrease the strength of the composites or can cause preliminary localized damage formations that can propagate/progress into catastrophic failure.

Arguably the unavoidable type is the void or porosity inside the laminated composites. These are of particular significance when missing consolidation pressure is not sufficient (out-of-autoclave process) combined with the gaseous curing process. The type of porosity sized smaller than the fiber diameters is often called micro-porosity (Figure 1.2a). If the number of micro-pores exceeds a certain limit, it can result in cellular-like micro-structures. In the mesoscale, the void parts, known as mesoporosity, usually result in fiber expose, so that they create regions where fibers or fiber bundles are not supported by matrix components (Figure 1.3). Since pores do not carry any load, the existence of porosity on every scale results in high local stress concentrations leading to a reduction in the total strength. Previous studies indicate that the void percentage, as well as the number of voids inside the laminate, can initiate cracks which cause preliminary failure [3]–[8].
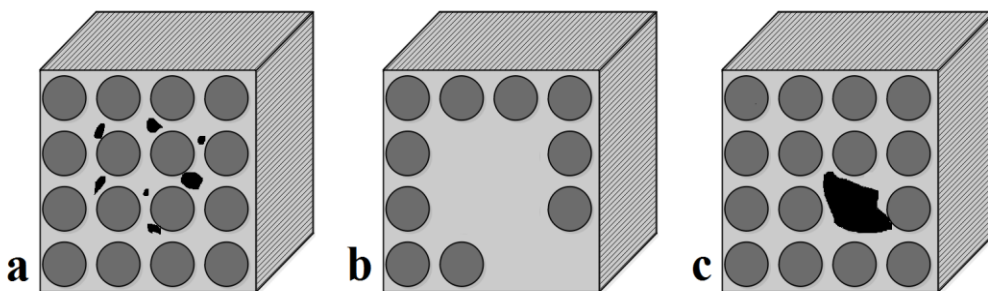
Figure 1.2 Anomalies that can occur in micro-scale unit of fiber reinforced composites from left to right: a) Micro-porosities b) Resin rich regions c) Foreign object causing debonding prone phases and effective fiber-matrix volume change.
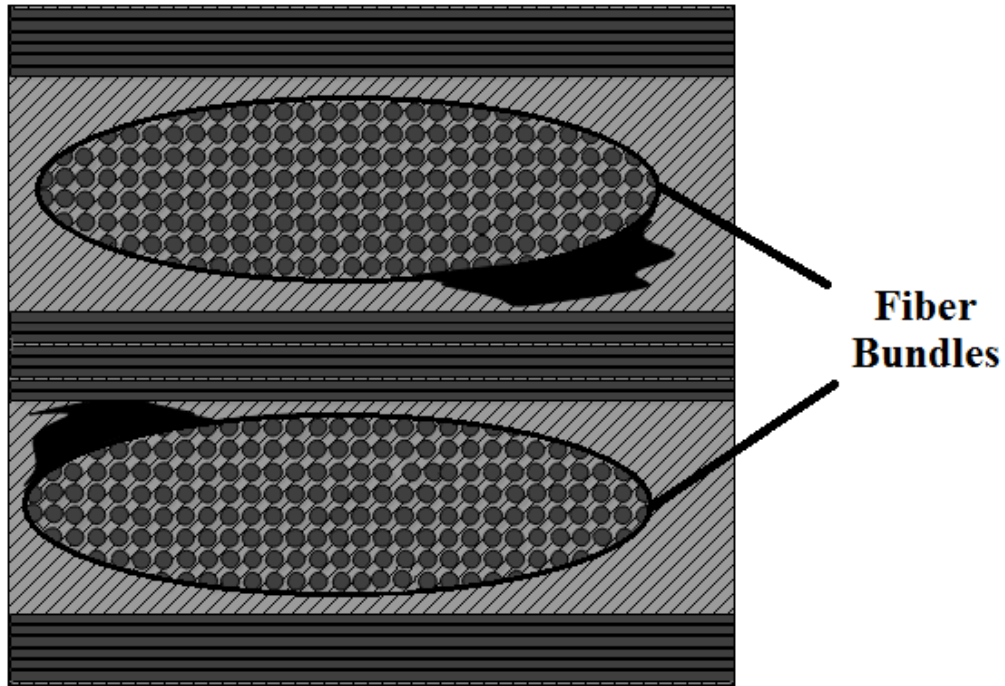
Figure 1.3 Meso-scale void formations/porosities around fiber bundles.

Another type of defect which is commonly observed within fiber-reinforced composites is the undulation of the fibers or fiber groups [9]–[19]. The undulation can be observed in-plane or out-of-plane orientations relative to the thickness direction of the laminate. Undulations occurring through the plane of laminate width (in-plane) are referred as waviness. On the other hand, undulations observed through the thickness direction of the laminate (out-of-plane) are called crimping. The waviness and crimping on the fibers or fiber bundles can cause a dramatic change in the local stress distribution [20]. Schematic illustrations of undulations are shown in Figure 1.4, and the example of preliminary failure due to the undulations is represented in Figure 1.5.
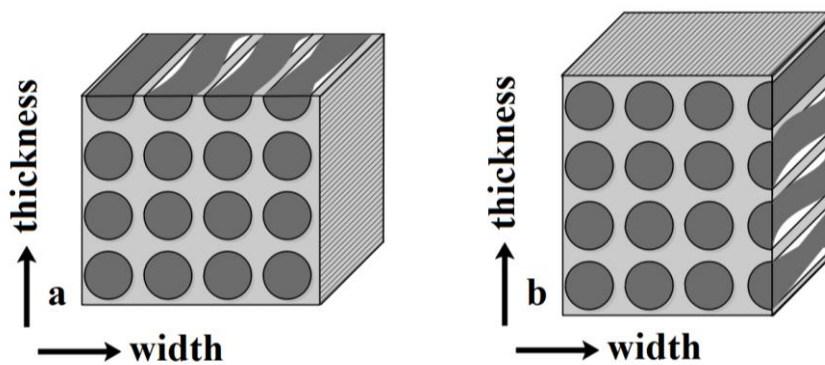
Figure 1.4 Possible undulations in a micro-scale representation of composite materials. a-In-plane (left/waviness) and b-out-of-plane(right/crimping) according to the composite thickness direction.
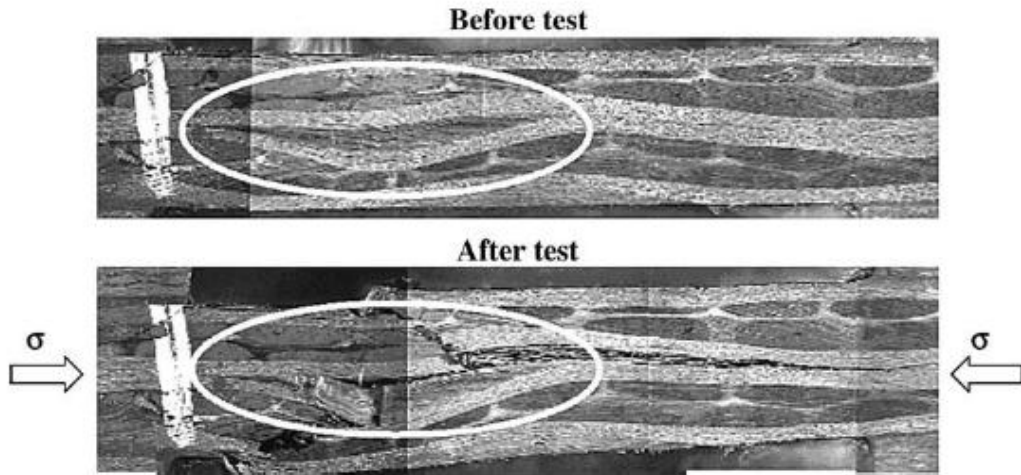
Figure 1.5 Premature failure of expectedly non-crimp composite materials due to out-of-plane fiber bundle undulations [19].

In fiber reinforced composites, in addition to the listed problems, other types of anomalies such as resin rich regions (Figure 1.2b), foreign objects (e.g. dust particles, prepreg-backing paper or plastic pieces, etc., Figure 1.2c) , and fiber knots may be observed. It should be mentioned that in the Figure 1.2 directions of stress components causing the corresponding failure are schematically represented as parallel ($\parallel$) or transversal ($\perp$) subscripts of stress (σ) according to the fiber orientation of the respective composite layer. Overall, defects in the fiber reinforced composites can result in an increase in local high stress spots, substantial changes in the local fiber volume fractions, and preliminary damage initiation sites, eventually affecting macroscopic fracture mechanisms.
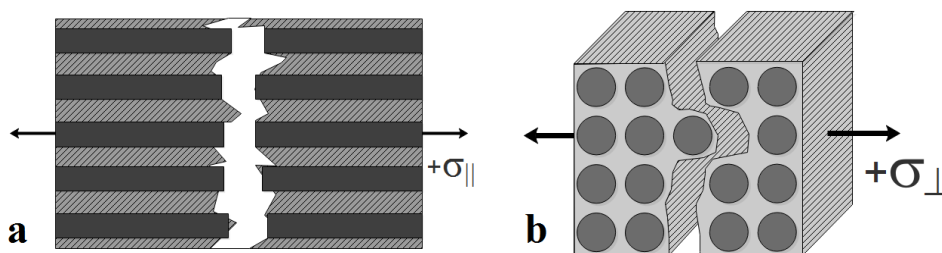
Figure 1.6 a) Fiber breakage due to parallel tensile loading (left). b) Inter-fiber fracture due to transversal tensile loading (right).

The main damage types, from microscale damage to ultimate failure, in unidirectional composites under parallel and transversal stress are specifically explained for further discussions.

6

The ultimate failure of structural composites is typically due to failure of the fibers, since they, reinforcement materials, are the primary load carrying part of the composites. If the individual fibers start to break, the block of fibers or even plies of laminates may fail successively; in other words, overall fiber-breakage is observed as schematically shown in Figure 1.6a. Interfiber fracture is another type of failure often found in the fiber-reinforced composites. It can be observed as the micro-cracks eventually propagate through the ply thickness forming the macro-scale cracks. These macro-cracks can be both of matrix fracture and fracture of the fiber/matrix interface type (Figure 1.6b). Interfiber fracture is often referred to as matrix cracking in macro-scale [21]–[24].

Other failure mechanisms of fiber-reinforced composites are intralaminar delamination (splitting) and interlaminar delamination (inter-ply). The main reason of delamination failure mechanism is out-of-plane loadings: as inter-ply delamination is observed due to weak spots on fiber-matrix adhesion. Splitting is the ply failure within the layer when exposed to high out-of-plane stress [20]. On the other hand, when laminates are subject to uniaxial stresses the individual plies are exposed to different stress levels which may cause fulfilled strain coupling [25].

The aim of this thesis study is to correlate deviations from the ideal characteristics and failure types, with non-destructive testing methods and traditional macro-scale stress-strain analysis. In the first case study, the focus is given to the anomalies of the laminated composites, namely in microscale voids and defects, in mesoscale undulations and inter-laminar interactions of the successive plies. This will be carried out using micro-computed tomography (μCT) technique. The second case study is an effort of in-situ acoustic/audio detection in conjunction with video recording microscope for identification of the failure modes.

1.3   Non-destructive Testing Methodologies for Characterization of Composite Materials

In order to understand the mechanical behavior of composites, non-destructive methods can be incorporated as somewhat unorthodox methods to complement and

enhance the traditional stress-strain analyses of mechanical testing. Contrary to many standard engineering materials, the complexity (heterogeneity and anisotropy) of the mechanical behavior of composites is much higher. Therefore, the research on effective characterization strategies for composites has been an actively expanding research area [20], [26], [27]. The proposed methodologies usually involve additional characterization techniques to accompany the mechanical testing results reporting the macroscopic stress-strain response of composites. Non-destructive testing (NDT) stands for the evaluation of materials to understand mechanical behavior typically without altering/distracting the original features or instantaneous state, and not harming the specimen being evaluated. One of the main advantages of NDT is that it is a cost-effective method for investigation.

Currently, available and well-established NDTs to analyze mechanical behavior of composites can be categorized according to inspection types [28]. In literature, suggested methodologies are listed as visual testing, ultrasonic testing, thermographic testing, radiographic (X-ray based) testing, shearographic testing, electromagnetic testing, acoustic emission and the combination of these methods.

Visual testing (VT) or visual inspection (VI) is one of the basic and often used non-destructive techniques. The most significant advantage of this method is its efficiency in cost and time. Visual testing can be performed on composites in-situ, pre-damage or after damage depending on the inspection equipment. On one hand, in-situ microscopy images can give quantified results on crack propagation and speed, whereas, scanning electron microscopy of damaged specimens helps to identify the fracture modes of composites. Digital image correlation (DIC) is also counted as a visual inspection method, which maps the strain field using a series of sequential images in reference to speckle-type patterns.

Ultrasonic testing systems involve a transmitter, receiver, and current transformer tool in addition to display devices. It is possible to obtain the location and size of defect or crack, with the orientation and characteristic information by ultrasonic testing [29]. Although the speed of scan, resolution, and defect detection capacities are respectively advantageous compared to other NDTs, the construction, mobility and usage of device set-up makes ultrasonic testing challenging task for composites.

Thermography or thermal imaging can detect and monitor in-situ crack initiations and propagations, impact damages and delamination as they create thermal

radiation. That is, the thermal imaging helps to locate the damaged area [28]. The instrument of sufficient sensitivity is expensive and may not be a practical choice for thick samples.

Radiographic testing appears the most commonly used non-destructive testing method for composite materials [30]–[32]. The technique allows the user to detect anomalies and failure mechanisms by transferring x-ray or gamma-ray through the specimens. There are various radiographic testing methods used for understanding the mechanical behavior of composites: film radiography, computed radiography, computed tomography, and digital radiography. Among all, x-ray computed tomography (XCT) is a non-destructive technique that visualizes interior features within specimens with 3D imaging. This effective characterization method can alter the focus size from micro to macro to obtain reliable image data [33]. Due to the radiation level of x-ray, the in-situ experimentation with XCT may require substantially expensive and customized laboratory equipment.

Shearographic testing is a laser optical technique which evaluates the stress and strain concentrations around anomalies of samples [28]. This method is the most noise-free non-destructive technique, so the reliability of the method is very high. On the other hand, the methodology is not effective in the determination of failure and mechanisms.

Electromagnetic testing method inspects the anomalies and evaluates fracture by using magnetic fields, electric current or both. Electromagnetic methods (EM) involve Remote Field Testing (RFT), Alternating Current Field Measurement (ACFM), Magnetic Flux Leakage (MFL), and Eddy Current Testing (EC) [34]. Each technique underlines the fundamental physical phenomenon of electromagnetic response by a different perspective.

Acoustic emission (AE) is a basic testing methodology which collects the acoustic data from the specimen under loading with highly sensitive sensors attached to them [35]–[37]. This technique differs from the other NDTs as the acoustic signal is produced by the specimen itself from the energy release instead of sending external signals such as ultrasound or x-ray. It is possible to detect, characterize and determine the failure mechanisms with AE. The drawback of the testing methodology is that it requires advanced skills, experience and database for correlation of the data and damage types.

In this thesis effort, x-ray computed tomography (micro-CT) is used by scanning undamaged parts of mechanically tested specimens to predict the mechanical behavior of non-crimp glass fiber reinforced laminated composites with specifically designed five different lay-up sequences as $(0)_8$, $(90)_8$, $(0/90)_{2S}$, $(+45/-45)_{2S}$, and $(0/45/-45/90)_{2S}$. In addition, the recently introduced acoustic signal tracking approach in conjunction with a video-recording microscope is applied as in-situ non-destructive inspection to evaluate and characterize the failure mechanism of carbon fiber reinforced composites containing six different stacking sequences. Following chapters explain the relationship of the data obtained from traditional testing and non-destructive inspection.

1.4   Motivation and Contributions

The main motivation of this thesis study is to show the significance of the mesostructural morphology effect on the mechanical behavior of composite materials by non-destructive testing methodologies.

In order to understand the effect of meso-architecture the composite specimens containing different lay-up sequences are investigated under tension. The correlations and deviations from the ideal characteristics and failure types are analyzed with non-destructive testing methods and traditional macro-scale stress-strain analysis.

Specifically, in the first case of this study the focus is given to the anomalies of the laminated non-crimp composites, namely in the form of microscale voids and defects, in mesoscale undulations and inter-laminar interactions of the successive plies. The micro-computed tomography (μCT) technique is used to seek the anomalies and inter-laminar interaction as a non-destructive inspection tool.

X-ray computed tomography is a quite common non-destructive testing methodology to visualize and to quantify defects within composite materials in addition to existing modeling efforts that it has been used for. Studies related to defect investigation of composite materials with X-ray based computed tomography mostly focus on the void presence inside materials and its impact on the mechanical behavior of composites [3], [6], [8], [38]–[40]. Additionally, the deformation of the reinforcement materials in meso-scale (such as fiber bundles and tow shapes) has been

investigated by computed tomography in various studies [31], [41]–[44]. While most of the previous work focused on the visualization and quantification of defects inside composite materials, some followed modeling studies where the models are obtained directly from computed tomography imaging [45]–[48]. In particular, the deviation from the ideal characteristics of non-crimp fabric (NCF) composites is an important research area among composite engineers [15], [18], [49]. However, existing work in the literature incorporating computed tomography rather focuses on the influence of microscale anomalies (such as potential void formation) on the mechanical response of woven fabric/textile composites, and three-dimensional direct modeling of tow/woven architecture.

The first case study of this thesis contributes to the NCF composites literature. It aims to emphasize the significance of the meso-architecture of non-crimp fabric composites on the mechanical behavior of materials by μCT imaging. Limited findings of previous studies related to microscale anomalies such as potential void formation is considered as the potential measures. Non-crimp fabric containing different yarn numbers are investigated according to various post-processing tools to understand the mechanical behavior dependence. The post-processing 3D image parameters are structure separation, structure thickness, degree of anisotropy, number of closed pores and connectivity. Results show that mechanical behavior can be correlated with a set of these parameters. but the correlating set or particular parameter is not the same for all cases and may vary depending on the stacking sequence. That is, no one single parameter can explain the mechanical behavior of composites in general. For instance, the principal eigenvector calculations which are strongly correlated with cross-ply laminate strength can be used to understand waviness and crimping occurred during manufacturing. Or, unidirectional laminate strength of composites consisting of small yarn numbers such as 300 TEX and 600 TEX, mostly depends on the cavity number inside fiber bundles. On the other hand, their failure modes are found correlated with the structure thickness, the structure separation and the cavity number parameters all together. Overall, there is a strong possibility to explain complex mechanical behavior of NCF reinforced laminated composites with a combined method of weighted parameters considering stacking sequence of composite laminates. This is worth and yet to be explored in detail.

Furthermore, in the second case study alternative characterization technique based on in-situ acoustic detection in conjunction with video recording microscope is

presented for detection and categorization of the failure modes. Acoustic emission (AE) methodology stands out as one of the more established methods for in-situ real-time damage monitoring in loaded composite materials [37], [50]–[53]. However, this method requires expensive instrumentation, detailed and profound data analysis which may not be standard and readily available for all composite practitioners with testing interests and needs. In-situ video microscope monitoring in conjunction with the acoustic data collection by a standard microphone is proposed as an easy to implement and cost effective methodology where AE may not be available for use in the categorization of progressive failure events. Particularly, the cross-ply like carbon-reinforced laminated composites containing six different lay-up sequences are investigated in this second case study with the newly introduced acoustic data collection methodology. Progressive failure events are categorized according to the collected in-situ monitoring that has been reported.

2 TRACING VISUAL SIGNATURES OF MECHANICAL BEHAVIOR OF COMPOSITES MATERIALS

2.1 Introduction

This case study involves collaborative work which led to a scientific paper output with the title *Effect Yarn Number on Tensile Behavior of Non-Crimp Glass Fiber (NCF) Composites: Correlated with micro-focus Computed Tomography Analysis, B. Yilmaz, K. Bilge, G. Baser, G. Kiziltas, M. Papila, Composites Part B* which is currently under preparation. To maintain completeness of the presented results and the coherence of the findings, the results of this collaborative work which is of multi-disciplinary nature, related previous work and contributions from other authors are included in this thesis. The details of the most relevant earlier study that focused on the mechanical testing phase and mesoscale stress-strain relationship can be found in [54]. The primary focus of this critical subsequent study in this thesis is on the three-dimensional imaging characterization of composite materials.

Elevated in-plane and out-of-plane mechanical response of composite laminates are the focus of many research activities. As of in-plane properties, very stiff and unyielding composite materials can be obtained by the use of unidirectional (UD) reinforcements. Typically, they are made of prepreg materials. However, the manufacturing of prepreg based composite laminates mostly requires an autoclave process (complex and very specialized-to the part- manufacturing process) and increases the cost substantially. In addition, the storage and usage of prepreg materials are limited with their shelf life [49]. Woven fabric reinforcements which find practical use in their non-prepreg form can lead to improved out-of-plane response and reduced manufacturing costs. However, their biggest problem appears to be the crimping of the

fiber yarns due to the interlacing which significantly reduces the in-plane properties of laminated composite as a result of undulation.

Non-crimp fabrics (NCF) have become an appealing building block for composite design. They are typically obtained by stacking layers of unidirectional yarns of different orientations which are stitched together through their thickness. They offer pre-assembled ply orientations ideally without crimping the fibers and associated one-axis layup that can substantially reduce the labor, scrap and manufacturing costs [55]. As a consequence of the non-crimp nature and despite light stitches, fairly good out-of-plane and in-plane mechanical properties are possible [15], [19], [32], [56]–[60]. A list of the advantages and disadvantages of the structural NCF composites were recently reported in [56] which aimed to provide a perspective on the design of the NCF building block itself, along with its effective implementation in the analysis and design of the structural composites. Due to their promising properties, the detailed investigation of such materials has been carried out by several groups. For instance, Lomov et.al published seven subsequent papers where they investigated the effect of several fabric properties under different loading conditions and made computational approximations on the behavior of multi-axial NCF based composite laminates [61]–[68]. Moreover, Varna [18] and Asp [69] studied the effects of stitching pattern and the lay-up sequence on the composite properties. In line with the experimental works, several computational studies have investigated the failure and damage mechanisms in NCF composites in order to make effective failure analysis [14], [70]–[76].

In a view to acquiring more reliable and realistic modeling of NCF reinforced composites, newly introduced characterization techniques have been used for mechanical behavior investigation. While some of the recent studies compare the traditional x-ray methodology with new approaches like synchrotron radiation [77], [78]; most of the composite material researchers use computed tomography to quantify void content inside specimens [3], [5], [6], [8], [26], [40], [79], [80] and to observe variationsin tow shape [9], [81]. In a broad perspective, although this study only focuses on the pre-damage investigation of composites, computed tomography can be used to identify microscale damage mechanisms in composite materials, damage mechanisms such as cracks and fiber breaks [3], [82]–[87]. Additionally, computed tomography is used to understand the interaction of failure mechanisms in the composite materials [86], [88]. At the next scale, sub-ply level, the failure mechanisms and fracture modes such as delamination and ply cracks can be detected by computed

tomography [86], [87], [89]. Since the type of radiographic testing plays a significant role in application areas (e.g. for thick specimens gamma-rays with short wavelengths, for thin composites x-rays); the resolution, scanning time and complexity of the specimen determines the type of testing needed. In this thesis, micro -computed tomography is used to investigate the microscale and mesoscale defects and to understand meso-architecture and its effects on the mechanical behavior. The importance of fast scanning availability and post-processing features determine micro-computed tomography as an advantageous method for non-crimp glass-fiber composites to analyze yarn number effect. In contrary, the content of the reported work in literature is rather focused on the influence of mesoscale architecture and microscale anomalies (such as potential void formation) on the mechanical response of woven fabric/textile composites.

More specifically, this part of the thesis work aims to demonstrate the effect of textile yarn number on the tensile properties of NCF/Vinyl Ester composite laminates. It should be noted that production of the laminates was purposely carried out using custom made UD NCF of constant ply areal weight and approximately same fiber volume fractions. As a consequence, potential factors on structural/mechanical behavior under tension were narrowed down to the yarn related mesostructure and manufacturing related void presence. Five different laminates with $(0)_8$, $(90)_8$, $(0/90)_{2S}$, $(+45/-45)_{2S}$ and $(0/+45/-45/90)_S$ stacking sequences were manufactured by vacuum assisted resin transfer molding technique as reported in [54]. These laminates were initially tested for fiber volume fractions (V_f) by loss on ignition method. Laminates with close V_f levels were then evaluated non-destructively by μCT analysis. Particular attention was given to the determination of ply by ply in-situ yarn properties/lay-out and the detection of micro-voids. Their overall effect on the tensile performance of NCF composites was also reported. In the mesoscale outlook, yarn number of an NCF composite can also be investigated as an effective factor because of a constant fabric areal weight. Both yarn number and meso-architectural design determine the width of the fiber bundles and the width of the inter-bundle regions. From a meso-mechanical point of view, these two areas act as load carriers (bundles) and stress transfer agents (inter-bundle resin region). This study particularly confirms that in order to obtain non-crimp and waviness free mesostructure, bundle width and inter-bundle size of fiber reinforced composites should be carefully selected. In short, meso-architecture is a predominant factor in determining the strength of lamina.

2.2 Experimental Procedure

2.2.1 Methodology

Composite laminates containing NCF reinforcements with four different yarn numbers labeled as 300, 600, 1200 and 2400 TEX having the same ply areal weight ($300 g/m^2$) were manufactured via vacuum infusion where Vinyl Ester resin was used as the matrix material. Laminates with five different lay-up sequences of $(0)_8$, $(90)_8$, $(0/90)_{2S}$, $(+45/-45)_{2S}$ and $(0/+45/-45/90)_S$ are studied. For simplification of results in their graphical representations, specimens with defined lay-up sequences containing different NCF reinforcements are labeled as given in Table 1. Fracture mode, mechanical performance and three-dimensional image analysis of each laminate comprising eight plies with different yarn numbers were reported.

Table 1: Labels for five different lay-up composites with four different yarn numbers.

Yarn Property	300 TEX	600 TEX	1200TEX	2400 TEX
$(0)_8$	300-UD	600-UD	1200-UD	2400-UD
$(90)_8$	300-T	600-T	1200-T	2400-T
$(0/90)_{2S}$	300-L	600-L	1200-L	2400-L
$(+45/-45)_{2S}$	300-X	600-X	1200-X	2400-X
$(0/+45/-45/90)_S$	300-Q	600-Q	1200-Q	2400-Q

2.2.2 Materials

Four different NCFs each containing E-glass fibers with different yarn numbers that are stitched with synthetic yarn were custom made by Metyx Composites Ltd.;

properties of fibers and bundles are reported in Table 2. Fiber bundle size and inter-bundle region size in dry fabric form are shown in Figure 2.1. All of the dry fabrics (with different lay-up sequences) were impregnated with Crystic VE-676-03 unsaturated vinyl ester resin supplied by Scott Bader Co. Ltd. The areal weights of all composite laminates were kept tat 300g/m2. Composite laminates were cut using water jet into small specimens according to test specimen dimensions.

Table 2 Bundle width, inter-bundle distance and fiber diameter information of four different yarn numbers.

Yarn Property	300 TEX	600 TEX	1200 TEX	2400 TEX
Bundle width [µm]	1000	2000	3000	4000
Bundle-to-bundle distance [µm]	400	800	1200	4000
Fiber Diameter [µm]	14	15	16.5	17.5
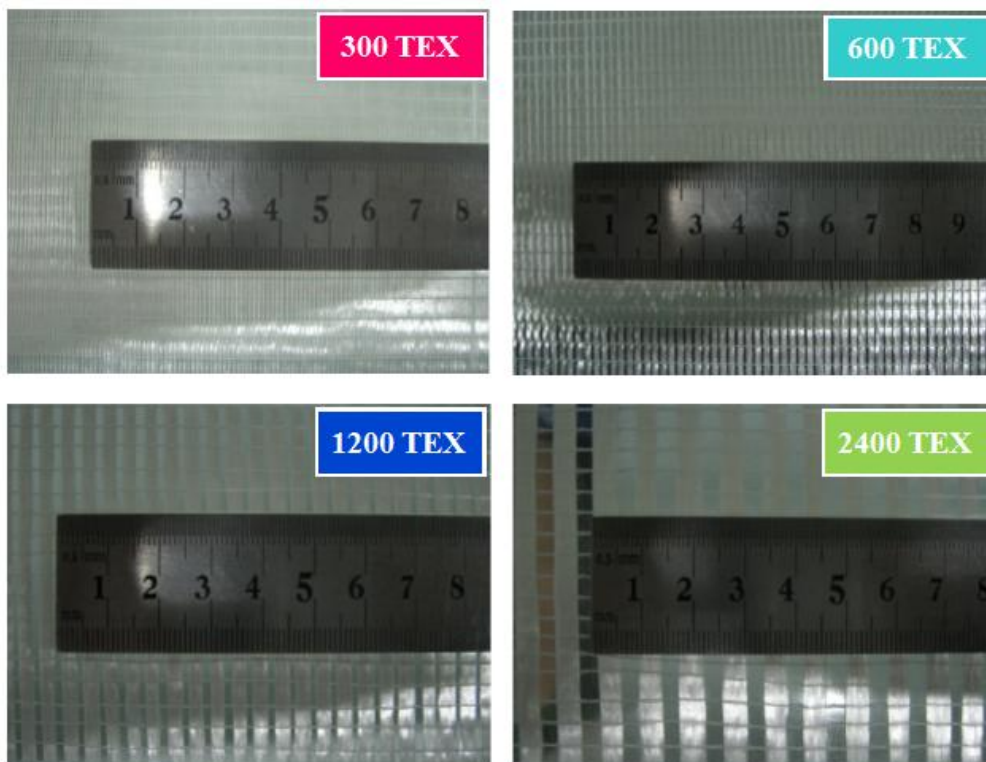
Figure 2.1 Images of dry fabrics containing four different yarn numbers.

2.2.3 Imaging by X-ray Computed Tomography

Obtaining three-dimensional gray-scale images of composite specimens is a challenging task. X-ray computed tomography is a well-established radiographic non-destructive testing methodology, but the selected parameters can significantly affect the image quality. In order to reduce and eliminate user-induced effects on the characterization technique, the inspection should be done according to the specification declared for the interested specimen. One should note that the given parameters herein only are applicable to the glass fiber reinforced vinyl ester composite samples.

In the first step of non-damaged composite characterization by micro-computed tomography, the specimens should be prepared with specific dimensions to focus on the desired features. The next step is the actual scanning with micro-computed tomography. In this study, 25mm x 25mm specimens of manufactured laminates have been scanned with Skyscan1172 high-resolution micro-computed tomography (μCT) equipment at Sabancı University Nanotechnology and Application Center. While using Skyscan1172, user-friendly software is available to control scanning parameters. The scanner is equipped witha Hamamatsu C9300 11MP camera connected to the computer and allows for scanning at three scanning resolutions of 1K (1000x 668 pixels), 2K (2000x1336 pixels) and 4K (4000x2672 pixels) to obtain the two-dimensional image. By changing the distance between the camera and the specimen, image pixel size can be adjusted. Also, the x-ray source voltage, current, and power affect the image quality. The raw images are created by exposing the specimen to x-ray source with a particular exposure time and collecting the transferred signal (Figure 2.2). Aluminum, copper or combined filters are available for use in the system. The signal is saved in chosen image format by the connected computer system. Then the specimen is rotated by selected step size, and another raw image is captured. The controller should take the x-ray attenuation coefficient of the sample into consideration when choosing acquisition parameters. In this study, X-rays are generated with an electron accelerating voltage of 81kV with a tungsten reflection and a beam current of 124 mA. The camera is set to 1K, and the distance between the object to the source is specified as 256 mm to create images with 25.9-micrometer pixel size. The chosen exposure time is 480 milliseconds and rotation step is 0.7 degree. The raw images are saved until the 360-degree full rotation is completed.
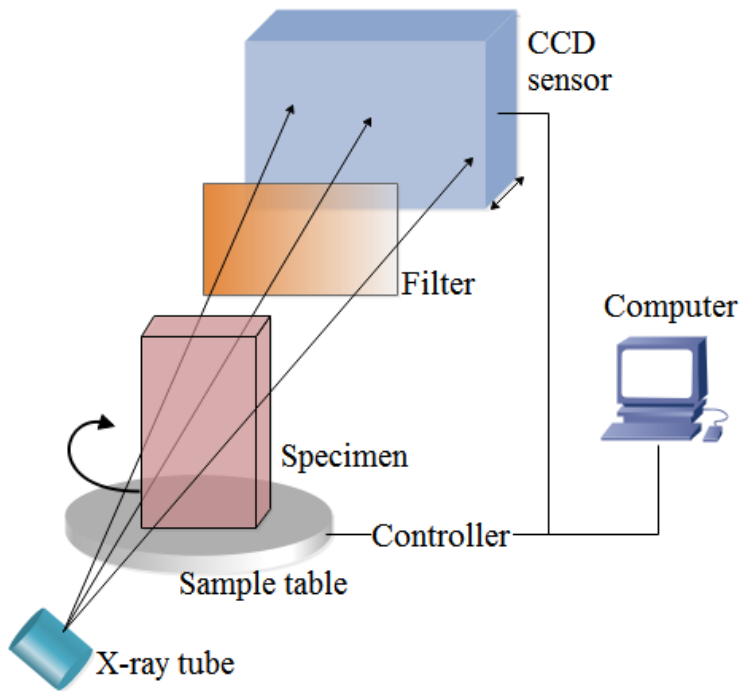
Figure 2.2 Schematic explanation of how x-ray computed tomography works.

After image acquisition is completed, the two-dimensional projection images of the object taken by µCT should be reconstructed. The reconstruction process has to be optimized with parameters such as ring artifact correction, beam hardening, misalignment, and smoothing. The cross-sectional gray-scale images are aligned with the selected parameters and reconstructed in order to prevent an undesired sinogram image as shown in Figure 2.3. In this study, NRecon (version: 1.6.9.4) software which applies modified Feldkamp's back-projection algorithm [90] is used in reconstruction of the images that are collected by the Radon transform. Furthermore, Dataviewer (version: 1.5.1) software is used to save rotated cross-sectional images in a Cartesian coordinate system in-line with the material coordinate system of composite samples.

Segmentation is another important step to analyze three-dimensional images. Since reconstructed and rotated images contain gray-scale color values, the analysis of objects is not directly applicable with simple software. There are several well-established statistical image segmentation methods for 3D images [91]. However one of the most basic and commonly used methods is pixel value based segmentation. In this thesis study, reconstructed three-dimensional objects, containing gray-scale values for each voxel (3D pixel), have been segmented (binarized) by using peak-valley histogram

thresholding method and were analyzed via CT-An (CT-Analyser, version: 1.14.4.1) program. For consistency of data, the range of the threshold for specimens was kept constant for all three-dimensional images. Prior to three-dimensional analysis, nine different region of interest (ROI) have been selected for analysis purposes (eight different ROIs for ply-by-ply analysis and one for overall laminate analysis as depicted in Table 3).
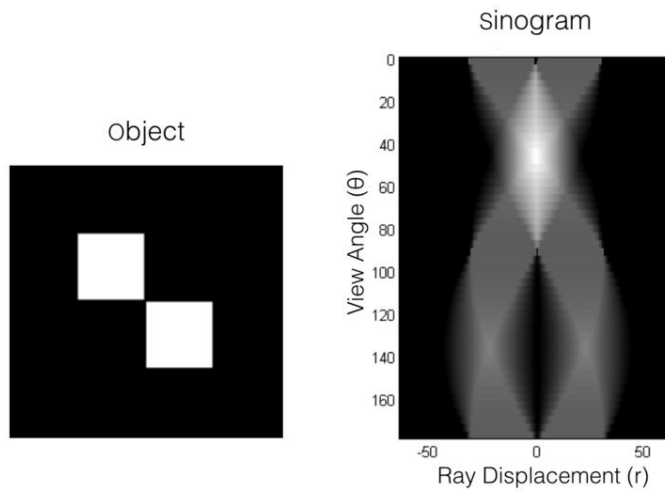
Figure 2.3 Sinogram image at right, obtained as a result of rotation of the left side object by 180-degrees through CT with Radon transform.

Table 3: Labels of various regions of interest analyzed with 3D image processing.

Region of Interest (ROI)	Unidirectional Composite $(0)_8$	Transversal Composite $(90)_8$	Cross-ply Composite $(0/90)_{2S}$	In-plane shear Composite $(+45/-45)_{2S}$	Quasi-isotropic Composite $(0/+45/-45/90)_S$
Laminates	UD-$(0)_8$	T-$(90)_8$	L-$(0/90)_{2S}$	X-$(+45/-45)_{2S}$	Q-$(0/+45/-45/90)_S$
Ply -1	UD-(0)-1	T-(90)-1	L-(0)-1	X-(+45)-1	Q-(0)-1
Ply -2	UD-(0)-2	T-(90)-2	L-(90)-2	X-(-45)-2	Q-(+45)-2
Ply -3	UD-(0)-3	T-(90)-3	L-(0)-3	X-(+45)-3	Q-(45)-3
Ply -4	UD-(0)-4	T-(90)-4	L-(90)-4	X-(-45)-4	Q-(90)-4
Ply -5	UD-(0)-5	T-(90)-5	L-(90)-5	X-(-45)-5	Q-(90)-5
Ply -6	UD-(0)-6	T-(90)-6	L-(0)-6	X-(+45)-6	Q-(-45)-6
Ply -7	UD-(0)-7	T-(90)-7	L-(90)-7	X-(-45)-7	Q-(+45)-7
Ply -8	UD-(0)-8	T-(90)-8	L-(0)-8	X-(+45)-8	Q-(0)-8

2.2.4 Three-Dimensional Image Analysis

Image analysis output parameters that were used for analysis purposes and are referred to in the results of the thesis work are listed below.

Structure Separation: This parameter refers to the average diameter of the numerous spherical objects that can maximally fit into the empty spaces in-between each three-dimensional segmented object inside region of interest [92]. The standard deviation of the diameters indicates the variability in the object separation. In the case studies, structure separation represents the one-dimensional average distance of the segmented bundles from other bundles. Structure separation is calculated statistically by CT-An within specified ROIs.

Structure Thickness: Similar to structure separation; structure thickness is the calculated average diameter of the various spheres that can fit into the objects inside ROI. The standard deviation of the diameters indicates the variability in the object thickness. In this study, structure thickness represents the dimensional average thickness of bundles viewed as three-dimensional objects. Structure thickness is also calculated statistically by CT-An within specified ROIs.

Number of closed pores (Cavity Number): As a part of the stereological analysis of the three-dimensional image, cavity number –in other words, the number of closed pores- has been calculated by the help of CT-An. A closed pore is a connected assemblage of black voxels that is fully surrounded on all sides in 3D by white voxels, and the cavity number represents how many closed pores are present in the selected region of interest. Given that each laminate had the same areal weight, similar fiber volume fractions, and close fiber diameters, the experimental assumption was that each ply contained an equal number of fibers which have been arranged in different meso-architectures. Hence, the counted number of closed pores inside each ROI was normalized by the corresponding object volume (object herein is referred as the total volume occupied by fibers). This approach isolates the sole effect of yarn number on the presence of manufacturing related micro-voids.

Connectivity: As a part of three-dimensional image analysis, connectivity which is calculated by the help of CT-An, indicates the redundancy of connections inside ROI. Redundant connectivity is derived from Euler number [93]. Euler number is calculated in terms of the numbers of voxel volumes (a_3), faces (a_2), edges (a_1), and corners (a_0) of

white parts which have a neighbor that had the white voxel region. In order to eliminate the position of ROI surface, Euler number on the 3D structure is calculated as follows:

$$EN = \sum(-1)^i a_i = a_0 - a_1 + a_2 - a_3$$

Euler number is a primary topologic measure for bone strength [92] which is calculated as the number of objects plus the cavity number inside bone minus the number of connections that must be broken to split the bone into two parts.

$$EN = Number\ of\ Objects - Connectivity + Cavity\ Number$$

As explained in Odgaard's study [93], these two equations lead to connectivity measurement on 3D structures as follows:

$$Connectivity = Number\ of\ Objects - Euler\ Number + Cavity\ Number$$

The connectivity of three-dimensional structures usually indicated as Connectivity Density (connectivity value per volume) since the connectivity value is dependent on the object volume and ROI volume [92].

In the case of fiber bundle reinforced composite materials, this value represents the meso-architecture effect on the composite since the binarized structure shows only bundles inside ROI. In other words, the mesostructure connectivity is calculated with the use of the connectivity parameter in this study.

Principal Eigenvector in Fiber Direction: Manufacturing related bundle waviness (local deviations in bundle directions) and crimping (in the thickness direction) defects are analyzed/quantified by the determination of principal eigenvector in the running fiber direction within a given ply.

The predominant object alignment inside ROI is determined by using mean intercept method [94] in Cartesian coordinate system and is reported as principal eigenvectors of the 3D image. The matrix for principal eigenvectors is generally represented as follows:

$$\begin{matrix} E_1 \\ E_2 = \\ E_3 \end{matrix} \begin{bmatrix} e_{xx} & e_{xy} & e_{xz} \\ e_{yx} & e_{yy} & e_{yz} \\ e_{zx} & e_{zy} & e_{zz} \end{bmatrix}$$

where the first row of the matrix stands for principal eigenvector on the predominant object direction; second and third rows stand for other two orthogonal components of the principal eigenvector. The predominant object alignment is correlated with the material coordinate system in the composite material terminology: the fiber direction (1) it is representing the predominant orientation of the composite samples. In the ideal case, where perfectly aligned rods are placed inside ROI; X is the direction of the fiber,

Y is the width of the composite, and Z is the thickness of composite; the corresponding eigenvector matrix is calculated as the 3-by-3 identity matrix. The principal eigenvector is denoted by placing the fiber direction to the first subscript of the vector components. In general, the principal eigenvector can be represented as

$$E_{principle} = [\, e_{1x} \ e_{1y} \ e_{1z} \,]$$

where 1 stands for the dominant fiber direction in the material coordinate system and X-Y-Z refers to the Cartesian coordinate system. Each value of the vector demonstrates the alignment of objects in the corresponding Cartesian direction viewed from the fiber direction. In this study, the Cartesian coordinates are converted to make the ROI selection easier. Hence, direction X represents composite thickness; Y is along the composite width (in-plane 90º), and Z orientation denotes fiber orientation (in-plane 0º) (Figure 2.4) when a unidirectional lay-up is concerned.
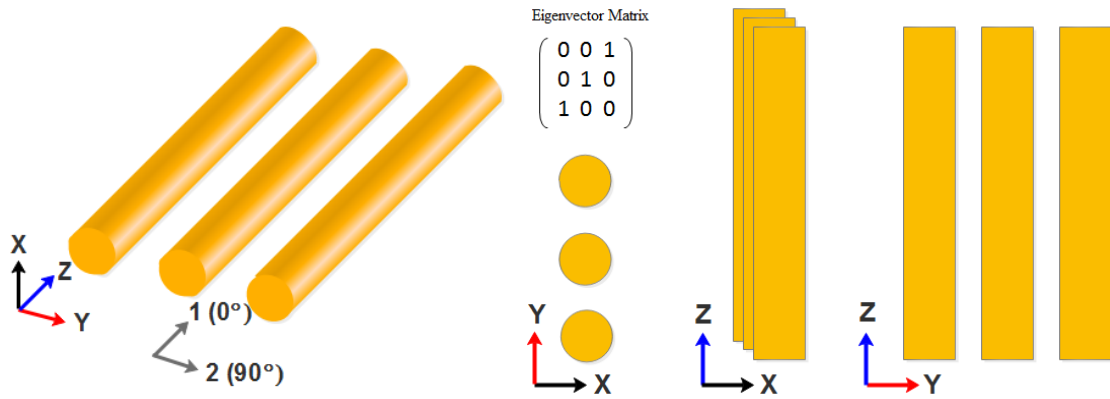
Figure 2.4 Ideal placement representation of fiber bundles (yellow cylinders) in a single UD layer with directions of coordinate and correlation of composite fiber directions (left). Cross-sectional images for ideally placed one layer fiber bundles with relative eigenvector values (right).

The cross-sectional images of 3D reconstructed data are saved on transversal direction (X-Y) direction with Dataviewer. Therefore; in this study, the principal eigenvector for unidirectional composite is representing the orientation as viewed from the Z-axis (Z as 1 in material coordinate system). The values of principal eigenvector (e_{zx} e_{zy} e_{zz}) should be [0 0 1] for perfectly aligned unidirectional fiber bundles. The first value of eigenvector, e_{zx} being e_{1x} displays how bundle orientation changes in the thickness direction of the composite. The deviation on e_{zx} counts the level of crimping that occurred during manufacturing for 0º plies. The second value of eigenvector, e_{zy} being e_{1y}, shows how the orientation of objects changes with

23

composite width. The deviation on e_{zy} is caused by the waviness of fiber bundles in the plane of plies. The third value of eigenvector, e_{zz} being e_{1z}, when different than one, shows bundle orientation changes in- or out- of the ply.

On the other hand, the principal eigenvector calculated for the 90° plies is in line with the second row of matrix since the predominant object alignment is in Y direction (Y now as 1 in material coordinate system). The values of principal eigenvector (e_{yx} e_{yy} e_{yz}) should be [0   1   0] for perfectly aligned unidirectional fibers within the 90° plies. As X direction denotes composite thickness, the value of e_{yx} represents the change of 90° plies in the direction of thickness. The deviation on e_{yx}, being e_{1x}, is caused by the crimping of fiber bundles. The second term, e_{yy} being e_{1y}, demonstrates if bundle orientation on fiber direction changes at all (when different than unity, caused in- and/or out-of the plan of the respective ply). The third value of eigenvector, e_{yz} being e_{1z}, shows the deviations from the Z direction while fibers lie in Y direction. The deviation on e_{yz} is now a result of the waviness of fiber bundles in the 90° plies. As a result of these axis conventions with respect to the fiber orientation, the quantified waviness and crimping on the composite samples can be and are reported via principal eigenvector calculation (Figure 2.11, Figure 2.28, Figure 2.40 and Figure 2.52). The second and third eigenvector components of principal eigenvector matrix are not reported in the study because they correspond to the orthogonal components of principal eigenvectors.

Anisotropy: As another post processing property, the degree of anisotropy of the structures inside ROI is calculated by CT-An. The algorithm behind the anisotropy evaluations depends on mean-intercept-length (MIL) measurement [37]. In addition to principal direction that is used for principal eigenvector calculation, imaginary lines rotate through 3D structure by the chosen sensitivity in order to calculate anisotropy. According to statistical analysis that passes through the structure in 3D, the longest mean intercept length divided by the shortest mean intercept length vector gives the degree of anisotropy of the interested object [92]. In the representations, the lower the degree of anisotopy value, the higher the isotopy for the corresponding sample.

2.2.5 Mechanical Testing and Fiber Volume Fraction Determination

Tensile tests of prepared composite specimens were performed as described in ASTM D3039 test standards [95]. Test samples were subjected to uniaxial tension with a constant displacement rate of 2mm/min. Corresponding stress-strain values were recorded for maximum tensile strength and elastic modulus determination, both in transverse and longitudinal directions with respect to the fiber orientation (Y and Z of the µCT analysis, respectively). A micro-extensometer was used for displacement measurement. For determination of fiber volume fraction in the obtained composite laminates, loss on ignition method described in ISO1887 test standards was used [96].

2.3 Results and Discussion

Several post-processed built-in parameters inside image analysis software are calculated to understand and relate to the tensile behavior of composite samples. Each of these parameters is shown in divided color coded bar-plot graphs to compare the yarn property effect. In the bar plots; the horizontal axis of the chart represents the ROI, and the longitudinal axis indicates the post-porossed property with given units. In addition to post-processed 3D image parameters listed as structure separation, structure thickness, cavity number, connectivity, principal eigenvector and connectivity density; for each specimen, stress-strain curves and the photographs of the damaged specimen are presented. Yarn property of samples and failure modes are explicitly shown in the figures for easier interpretation.

A significant effort was originally put to keep fiber-matrix volume fraction (V_f) the same and produce laminates with equal ply-areal weights to be able to observe effects of yarn number in an isolated fashion. The loss-on-ignition test results showed that samples have reasonably close fiber volume fractions of 50-52 percent (Figure 2.9c, Figure 2.20c, Figure 2.26c, Figure 2.38c, Figure 2.50c). The constant ply-areal weights and similar fiber volume fraction characteristics allow for a reliable analysis of the yarn number effect on the tensile behavior of specimens.

2.3.1 Tensile Performance of Unidirectional Composite Laminates $(0)_8$

In selected region of interests, the bundle and inter-bundle dimensions were statistically measured as the post-processed built-in properties of structure separation and structure thickness respectively. Among calculated properties, the average structure separation of separate ply-by-ply and laminated unidirectional composites are displayed with standard deviation values as one-sigma error bars in Figure 2.5. The inter-bundle distance values given in Table 2 are also considered for image correlation. Specifically, separated lay-up specimens with 300TEX yarn number display on average the highest values in contrast to the lowest value displayed by its laminated composite form.

On the other hand, structure thickness values that are obtained by a similar procedure are reported in Figure 2.6. Based on structure thickness plot, laminas labeled UD-(0)- 3, 4, 5, and 8 demonstrate increasing structure thickness behavior as yarn number increases. Laminas labeled UD-(0)-, 1, 7, and UD-(0)$_8$ (whole laminate of 8 plies) images show that specimens with 300 TEX yarn property have the lowest and samples with 2400 TEX have the highest structure thickness, respectively. Also, samples with 600 TEX yarn numbers display slightly higher structure thickness than 1200 TEX samples. The unusual behavior of lay-up labeled UD-(0)-2 and UD-(0)-6 is interpreted as outlier behavior because the specimens with 300 TEX and 600 TEX yarn numbers could not be separated due to the ROI selection imperfection as apparent in Figure 2.13 and Figure 2.14. Overall, structure separation and structure thickness analysis suggest that the in-situ mesostructure of fiber bundles was preserved after impregnation but overall a direct clear association between structure thickness and separation of the ply-by-ply laminas and the mechanical tensile behavior of the composite could not be made The latter is most likely a consequence of the manual split up of the laminate samples into ply-by-ply ROI's and the interface uncertainties of adjacent plies clearly visible in their micro-CT images.

As an additional post-processing property so as to explain the tensile behavior of unidirectional composites, the cavity numbers for unidirectional composite samples were calculated with different ROI selections. Figure 2.9a shows the cavity number per volume inside bundles for samples with four different yarn numbers. The correlation between 3D-image analysis and mechanical performance of the composite laminates was identified in [3] as the number of closed pores inside the laminates rather than the

void percentage of specimens. According to this proposed correlation, samples having small cavity number should perform better in a conventional mechanical test. Moreover, meso-architecture of yarns is investigated by quantifying the fiber-volume fraction of the randomly chosen cross-sectional images of laminates (Figure 2.17). The ideal conditions and their fiber-volume fraction calculations are given for comparison purposes. Also, reconstructed 3D images are shown in Figure 2.13, Figure 2.14, Figure 2.15 and Figure 2.16.

According to these results, mechanical performance under longitudinal tension was found to be dependent on the yarn number (Figure 2.9d). Ultimate tensile strength of laminates reinforced with NCF having 600TEX yarn number was superior to the others whereas for samples with 2400 TEX fibers the performance of the composites decreased drastically. On the other hand, the observations that the laminates of 300 TEX glass fibers have lower tensile strength than the 600 TEX glass fibers suggests that the inter-bundle distance, bundle-bundle distance, and interactions should play a key role in an efficient load transfer and higher strength. This may be considered as a meso-architectural self-design/arrangement effect or tuning during lamination followed by consolidation under vacuum.

The specimens having small yarn numbers (e.g. 300 TEX), despite finer meso-architecture may cause inadvertently manufacturing defects due to the resin flow anomalies during infusion process as some fibers inside the closed-packed bundle may not get impregnated enough. The specimens of 300 TEX call for the most closed-packed configuration among other yarn numbered samples based on their connectivity density demonstrating the highest values in Figure 2.10. Since fiber bundles have been aligned in one direction in the unidirectional composites, connectivity density values can be viewed as representative numbers of the overall inter-bundle distances when interpreted in an opposite fashion.

For the specimens with high yarn numbers like 1200 TEX and 2400 TEX, the bundle architecture inside laminates and crimping seem to be much more crucial as far as the mechanical strength is concerned. Since the purpose of the NCF woven as reinforcement inside composite laminates is to minimize fiber undulation effects if not create undulation free fabrics, the ideal bundle placement should be in order. However, during the manufacturing process, bundle layers are placed and packed to obtain desired fiber volume fractions and create an effective consolidation of the laminate. As it is seen

in Figure 2.17 and quantified in Figure 2.11, the most knitting-like effect (just because of the self arrangement of the layers on one another) is observable on yarn property of 2400 TEX composite laminates. Due to the undulation effect and tow displacement in the plane of the adjacent loose plies of 2400 TEX yarn number distinct plies could not be effectively identified as indeed 8 separate layers. Therefore, the specimen was investigated as 1-2, 3-4, 5-6 and 7-8 dual sets together (Figure 2.16). Since the load transfer capability of the large yarn number specimens depends mostly on meso-architecture of the bundles inside laminate, such as the 1200 TEX and 2400 TEX specimens, the resin flow driven manufacturing defect effects are not as significant as they are in the small yarn number samples like 300 TEX and 600 TEX. However, it should be noted that both the mesostructure of bundles as well as the manufacturing process to produce samples with minimal amount of void (corresponding to resin rich regions) have an impact on the tensile behavior of 1200 TEX and 2400 TEX non-crimp composite laminates.

While fracture mode of laminates with 300 and 2400 TEX NCF has been of ply-splitting type, for 600 and 1200 TEX NCF composites the failure mode was a catastrophic failure (Figure 2.9b). This failure mode difference is also associated with the strength differences of laminates. Hence, it can be noted that the load transfer capability between fibers and bundles was not as efficient for 300 and 2400 TEX NCF composites for a variety of different reasons. While 300 TEX suffered defects due the bundle voids and bundle-to-bundle interaction, 2400 TEX were prone to lose individual fiber packing. Both may induce the critical matrix cracking parallel to the fibers during the early stages of the tensile test giving rise to a major ply splitting failure. On the other hand, for laminates with 600 and 1200 TEX NCF, load transfer was more efficient and catastrophic failure occurred.

The mechanical strength of the laminated composites with 600 TEX is superior to 300 TEX specimens correlating well with their reduced number of cavities as displayed by their ROIs for 600 TEX when compared to the 300 TEX. Additionally, it is clear that the wide structure separation (inter-bundle distance) with the architectural placement of fiber bundles for 300 TEX may lead to new matrix cracking through the lamina width during load transfer. Since the bundle and matrix placement is tuned relatively well in 600 TEX and 1200 TEX, their failure occurred at higher energy levels and in a catastrophic mode by displaying a relatively higher mechanical strength under unidirectional tension than the 300 TEX and 2400 TEX yarn numbers.
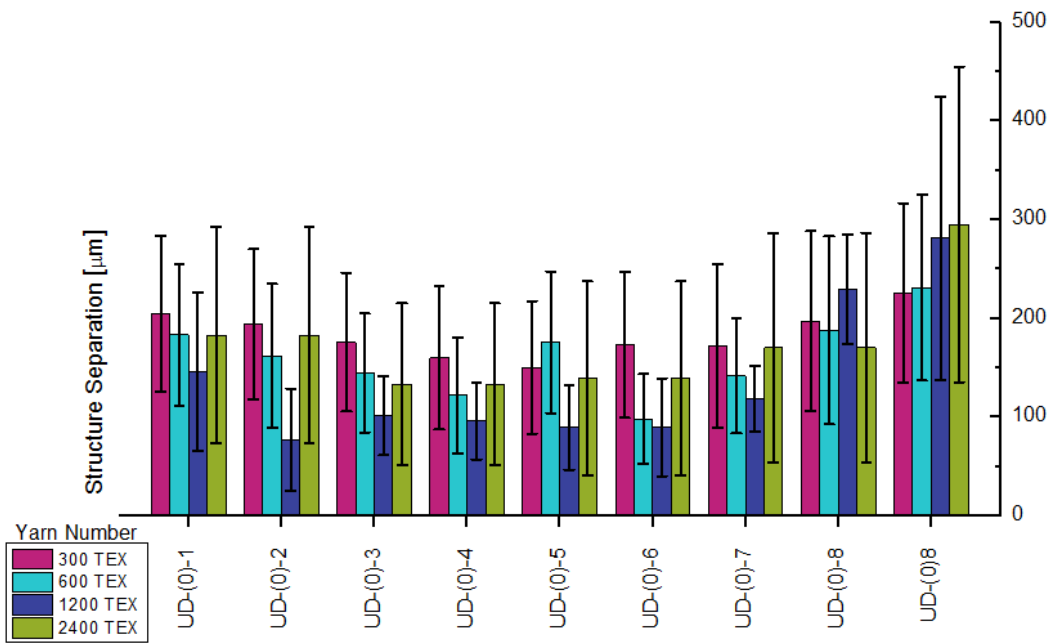
Figure 2.5 Average structure separation representation of unidirectional laminate and lay-ups with standard deviation values included.
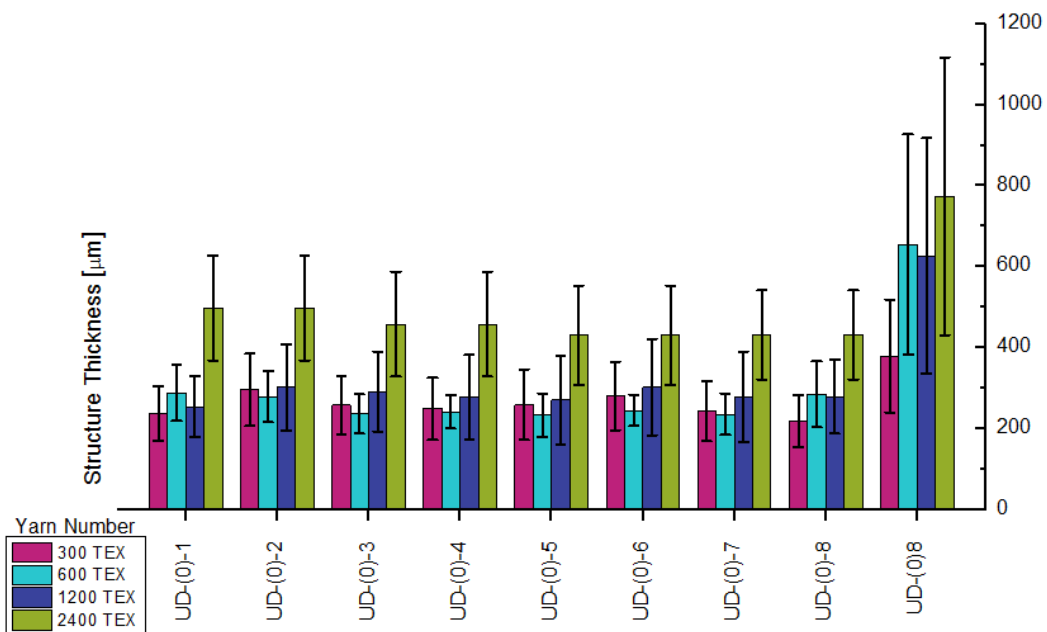
Figure 2.6 Average structure thickness representation of unidirectional laminate and lay-ups with standard deviation values included.

Table 4 Tensile strength, tensile modulus and V_f results of unidirectional laminated composites.

Yarn Number (TEX)	V_f (%)	Tensile Strength (MPa)	Tensile Modulus (MPa)
300	52	758.1±4.1	38.5±0.4
600	52.5	**928.8±12.5**	38.8±0.2
1200	50	793.8±11.4	39.1±0.5
2400	51	654.6±21.5	39.2±0.6
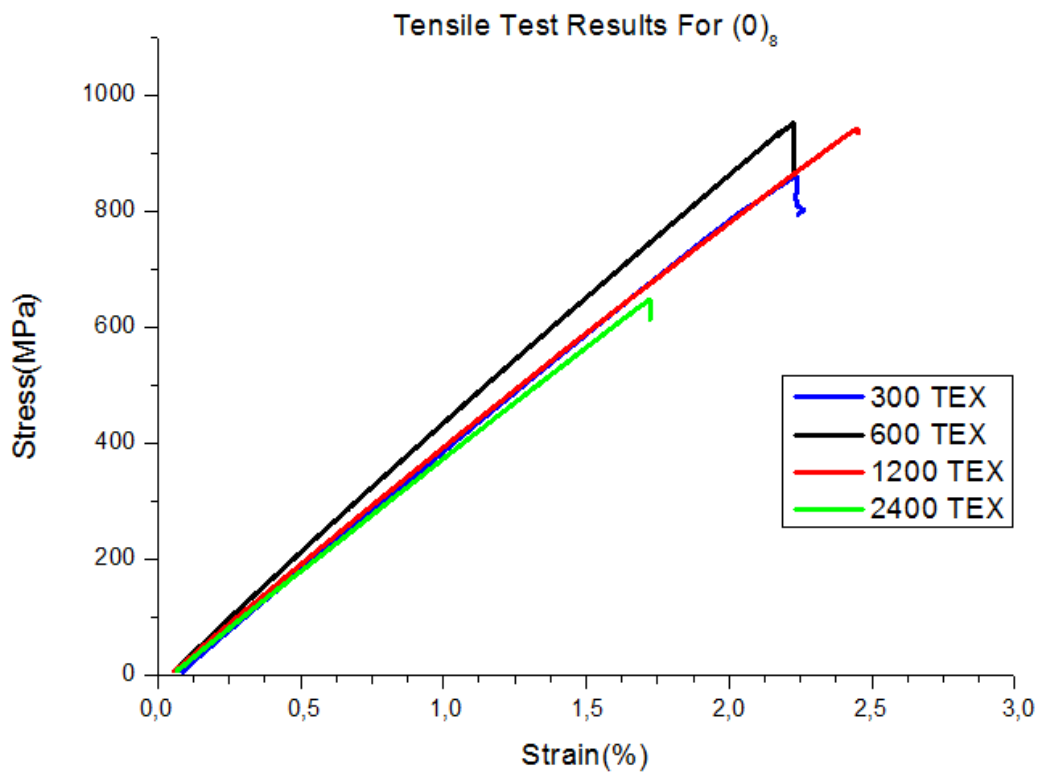
Figure 2.7 Stress-strain curves of unidirectional laminated composites under tension.

Figure 2.8 Failure modes and images of unidirectional laminated composites after failure.

Figure 2.9 The normalized cavity number of unidirectional composite samples with different ROIs.
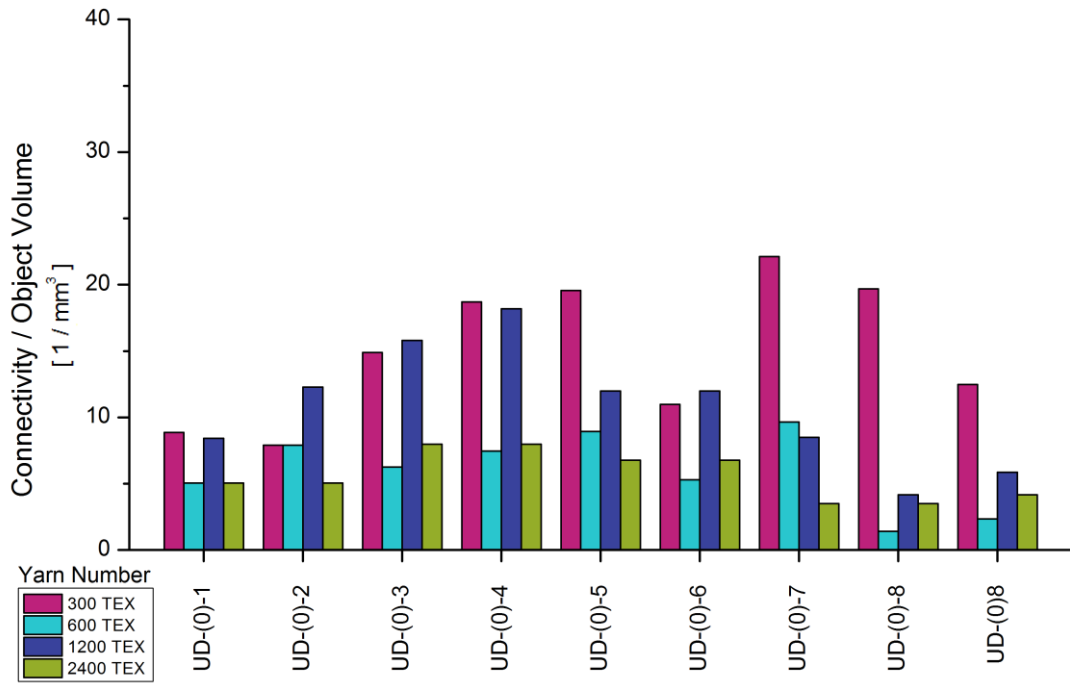
Figure 2.10 Connectivity density of unidirectional laminates and lay-ups.
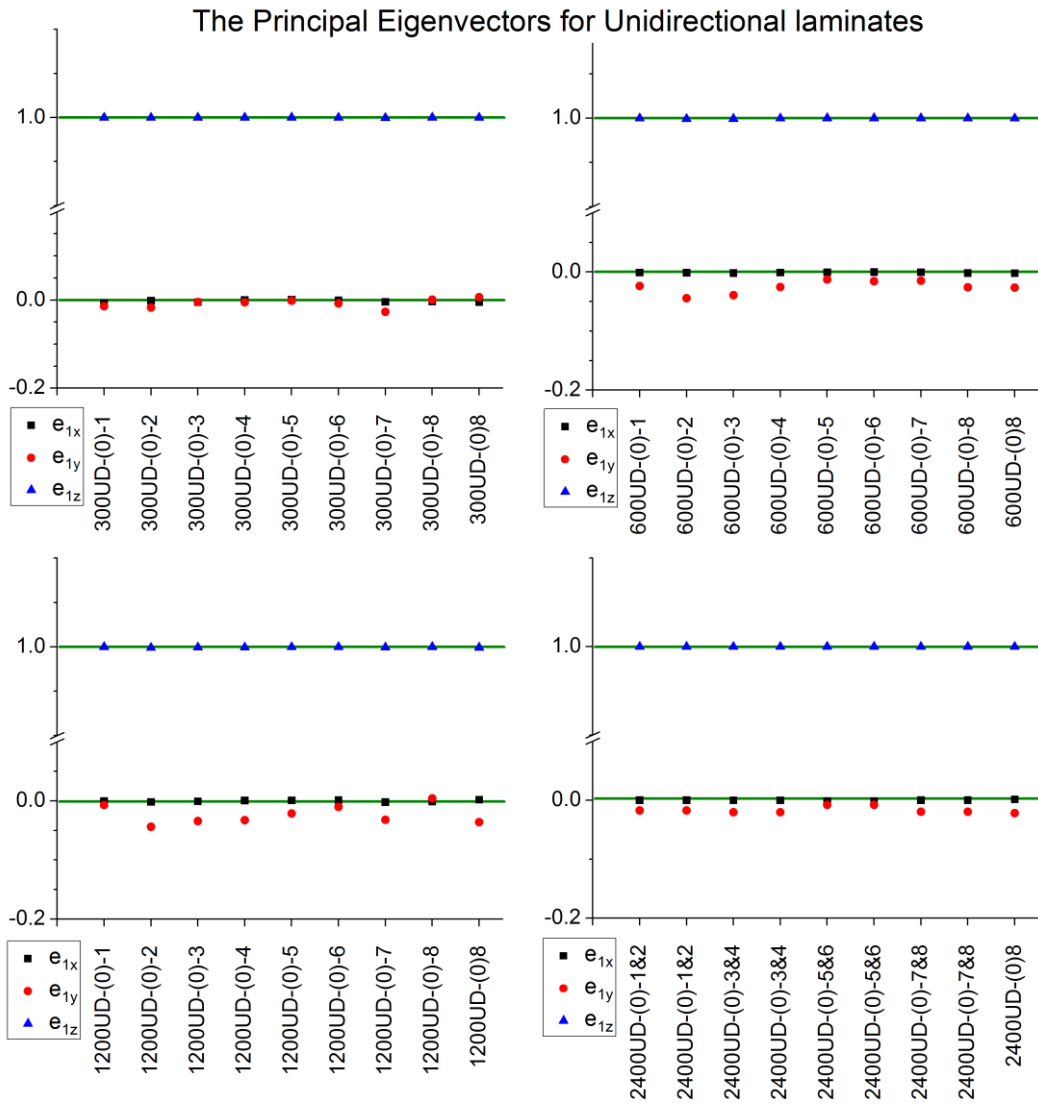
Figure 2.11 Principal eigenvectors of unidirectional laminates and lay-ups.
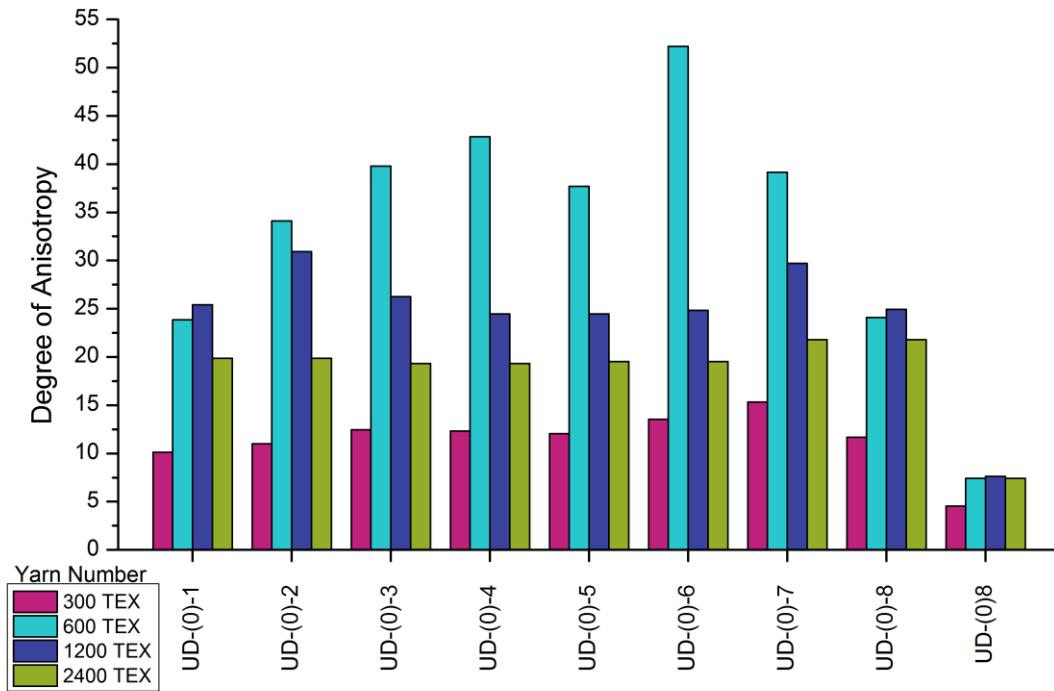
Figure 2.12 Calculated degree of anisotropy of unidirectional laminates and lay-ups.
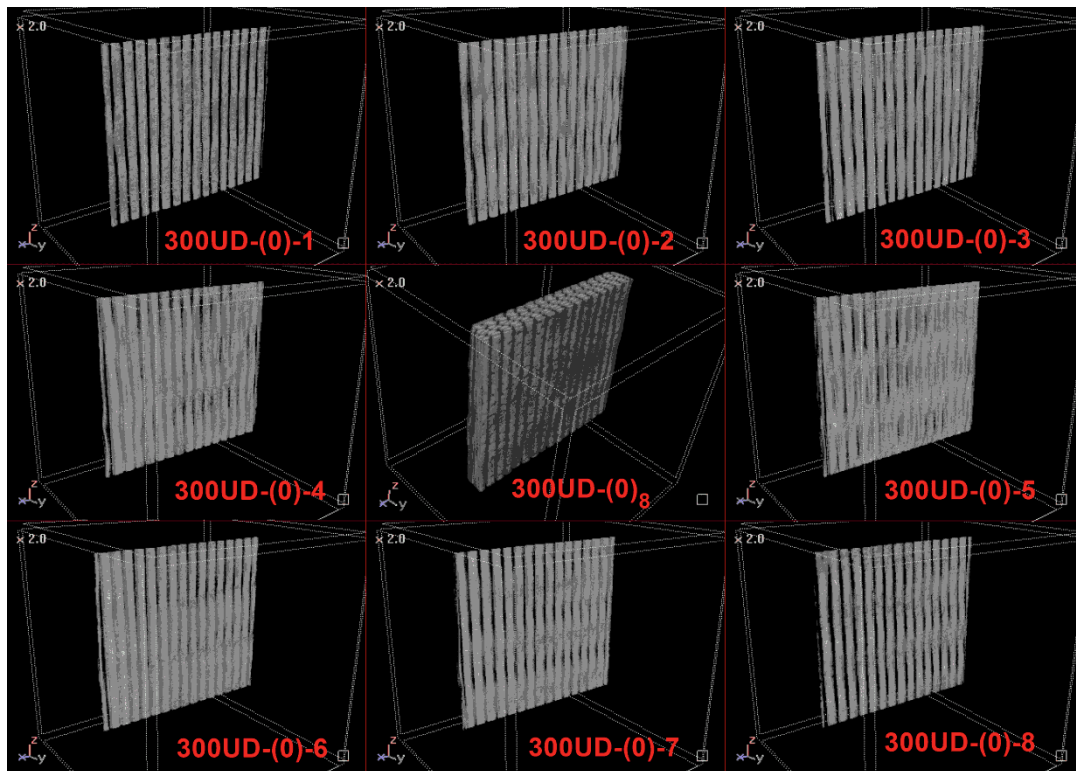
Figure 2.13 Reconstructed 3D images of unidirectional 300 TEX specimen labeled as plies and laminate.
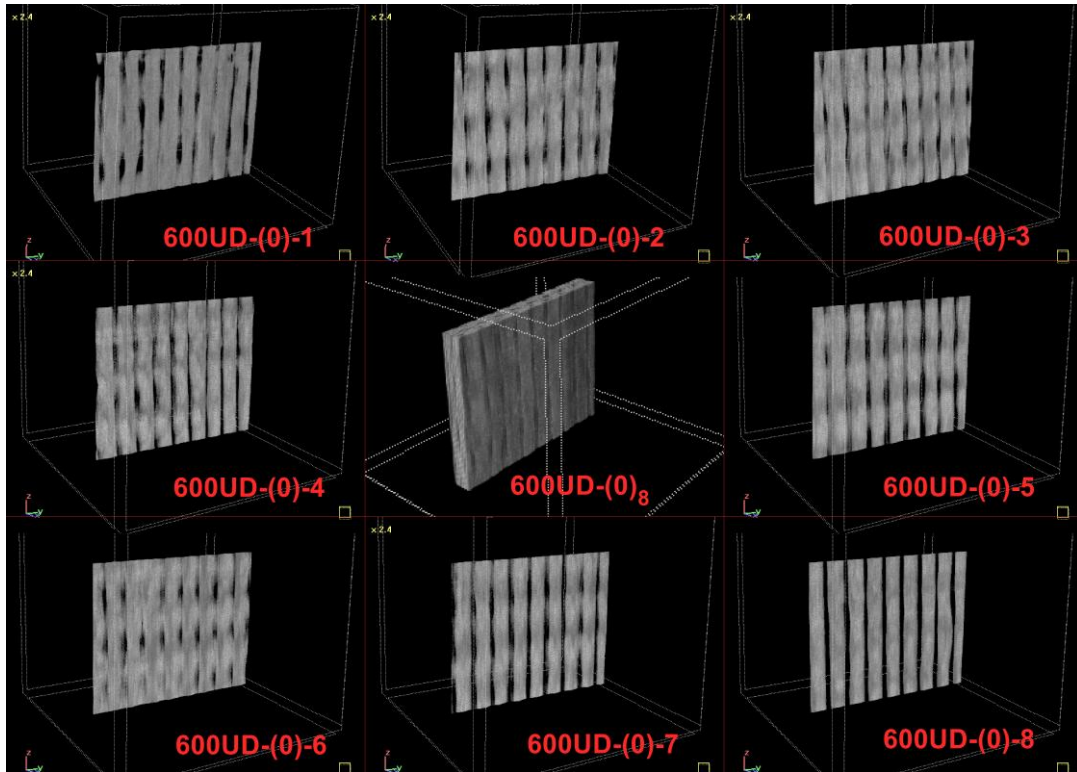
Figure 2.14 Reconstructed 3D images of unidirectional 600 TEX specimen labeled as plies and laminate.
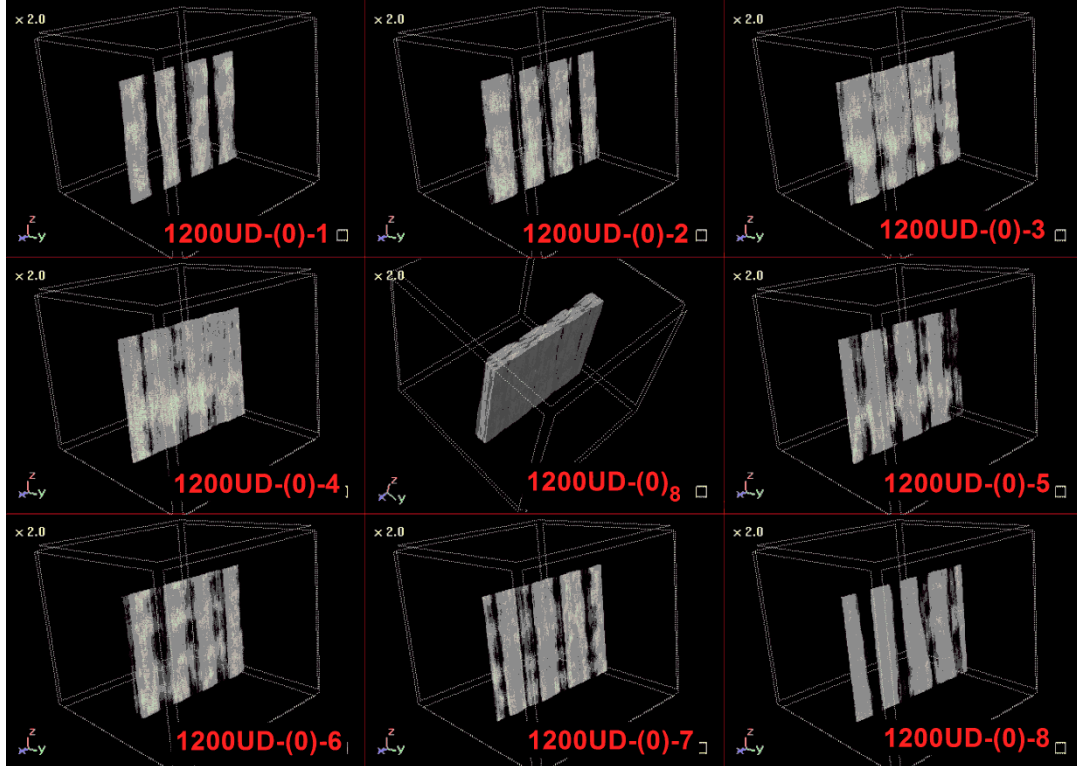
Figure 2.15 Reconstructed 3D images of unidirectional 1200 TEX specimen labeled as plies and laminate.
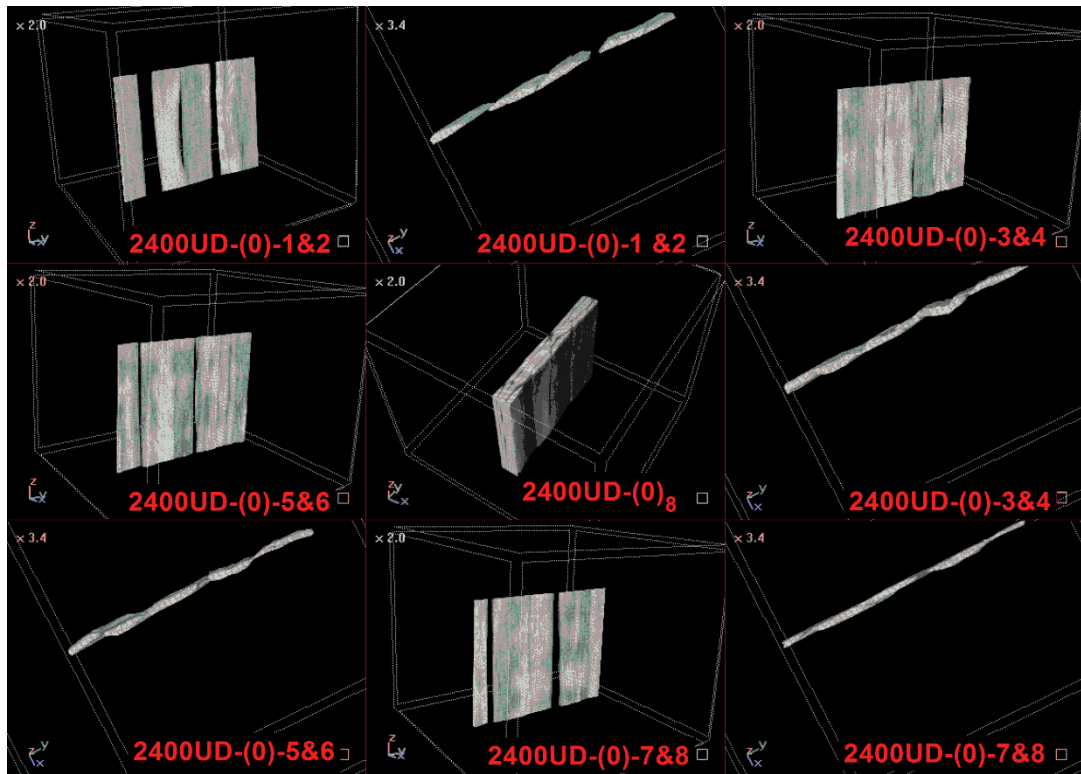
Figure 2.16 Reconstructed 3D images of unidirectional 2400 TEX specimen labeled as plies and laminate.
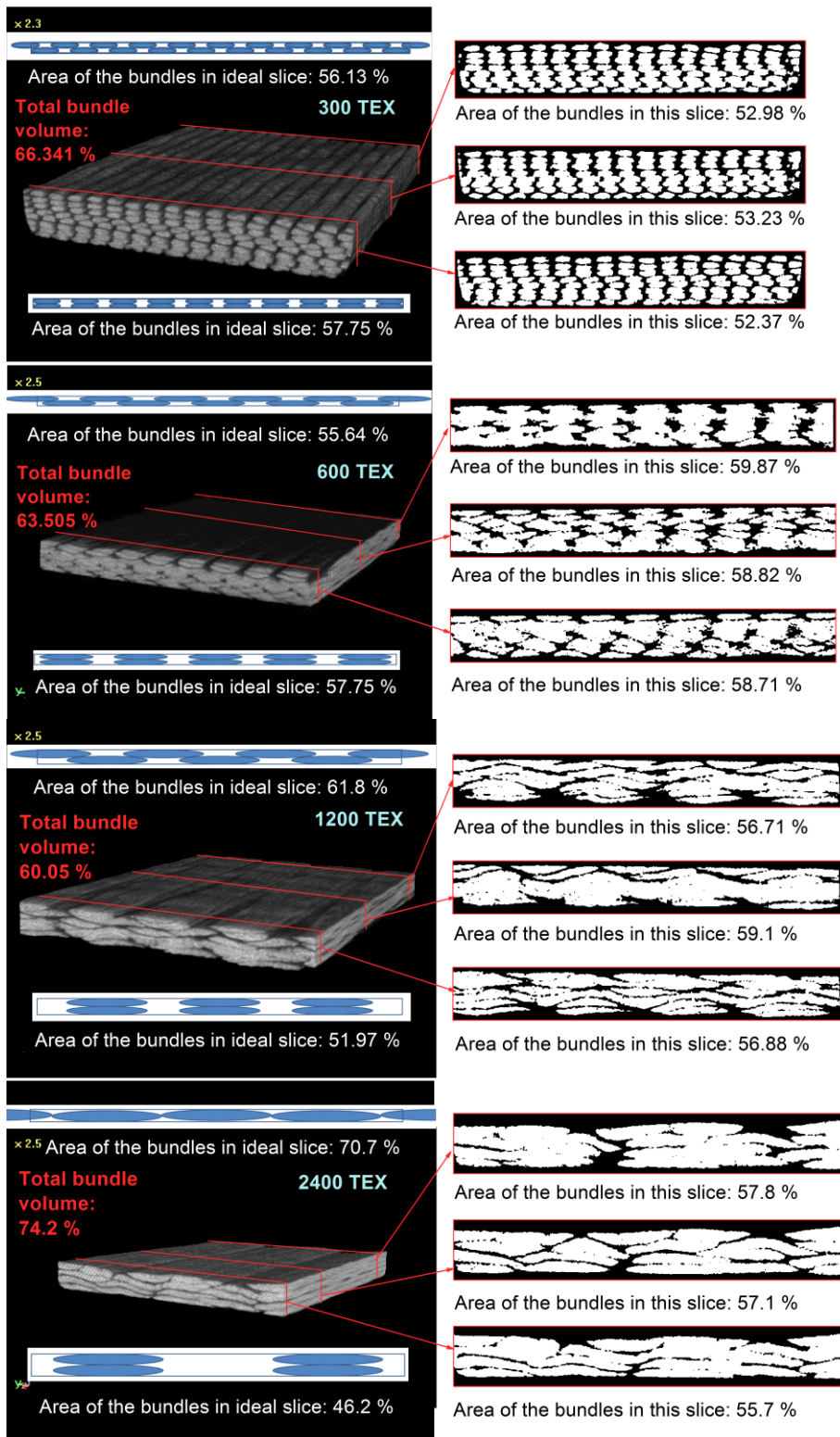
Figure 2.17 Randomly chosen binarized cross-sectional images of unidirectional samples and their ideal mesostructure. Area and volume of bundle percentages calculated from images are indicated.

2.3.2 Transverse Tensile Performance of Composite Laminates $(90)_8$

During image analysis, $(90)_8$ images have been obtained by rotating images of $(0)_8$ specimen by 90º since the manufactured plates are the same for $(0)_8$ and $(90)_8$. However, to understand the mechanical performance of laminate with new segmentation parameters, only matrix parts of the composite have been saved and analyzed. The reason for changing the segmentation is that the load carrying capacity under transverse tension of UD specimens is governed by the matrix constituent where the effect of yarn numbers can be assumed to be merely insignificant.

Contrary to the longitudinal tension results, under transverse loading the performances of all of the laminates were nearly identical (Figure 2.20). Confirming the expected behavior, the effect of reinforcement is observed to be almost negligible under this load condition. Hence, the final failure usually occurs due to matrix failure in $(90)_8$ lay-up under tension.

The void formation inside matrix is related to the decrease in mechanical strength of $(90)_8$ laminates. The results for the cavity number inside resin component are presented for each layer of the ply-by-ply ROI's (Figure 2.20). No particular pattern could be determined to suggest the superiority of a particular yarn number. Total pore space inside resin of the laminates is also calculated: supporting the close values of tensile modulus and tensile strength of the T-$(90)_8$ specimens where total voids inside the matrix components show flatter behavior than the cavity number calculations presented for the ply-by-ply configurations where the bundles were treated as void as well (Figure 2.21).

Table 5 Tensile strength, tensile modulus and V_f results of $(90)_8$ laminated composites.

Yarn Number (TEX)	V_f (%)	Tensile Strength (MPa)	Tensile Modulus (MPa)
300	52	39.5±1.2	5.4±0.4
600	52.5	38.8±1.0	5.9±0.3
1200	50	39.1±1.5	5.8±0.2
2400	51	39.2±1.5	5.6±0.3
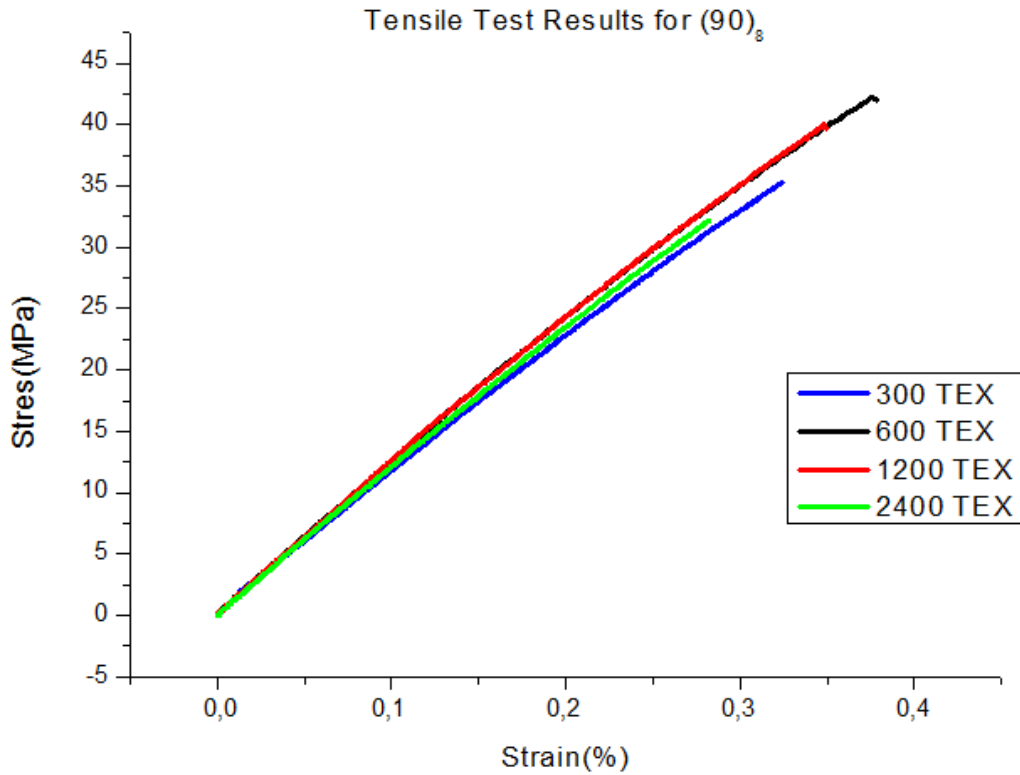
Figure 2.18 Stress-strain curves of (90)₈ laminated composites under tension.
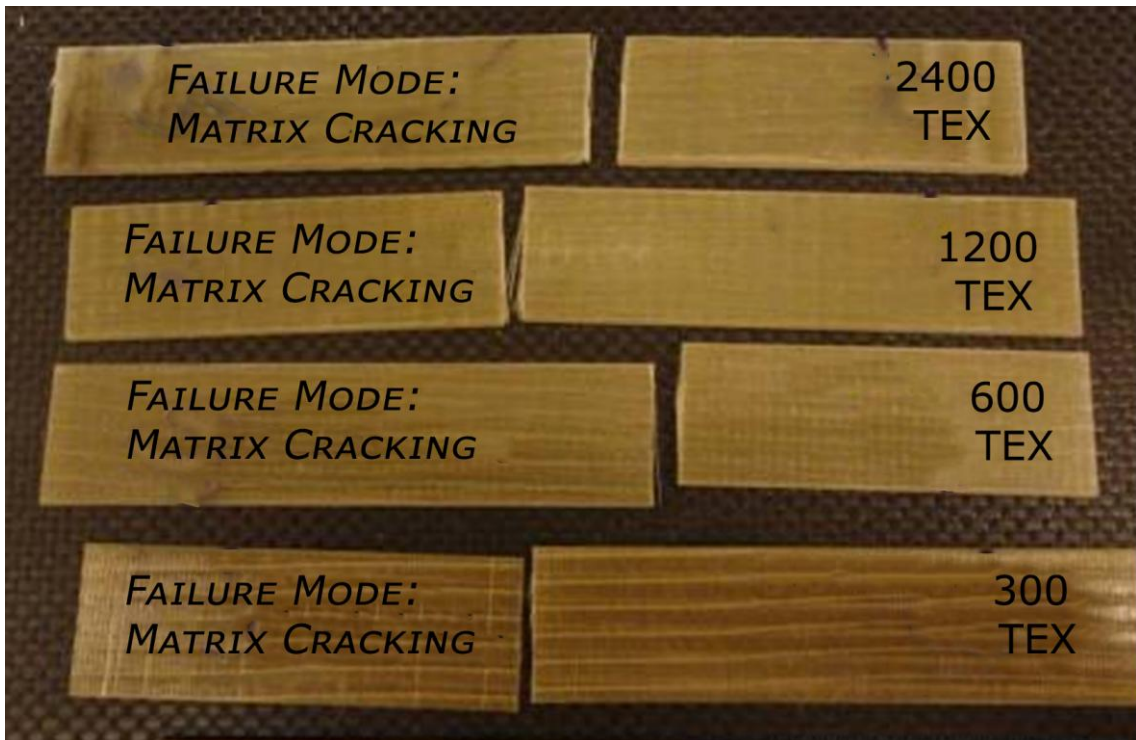
Figure 2.19 Failure modes and images of (90)₈ laminated composites after failure.

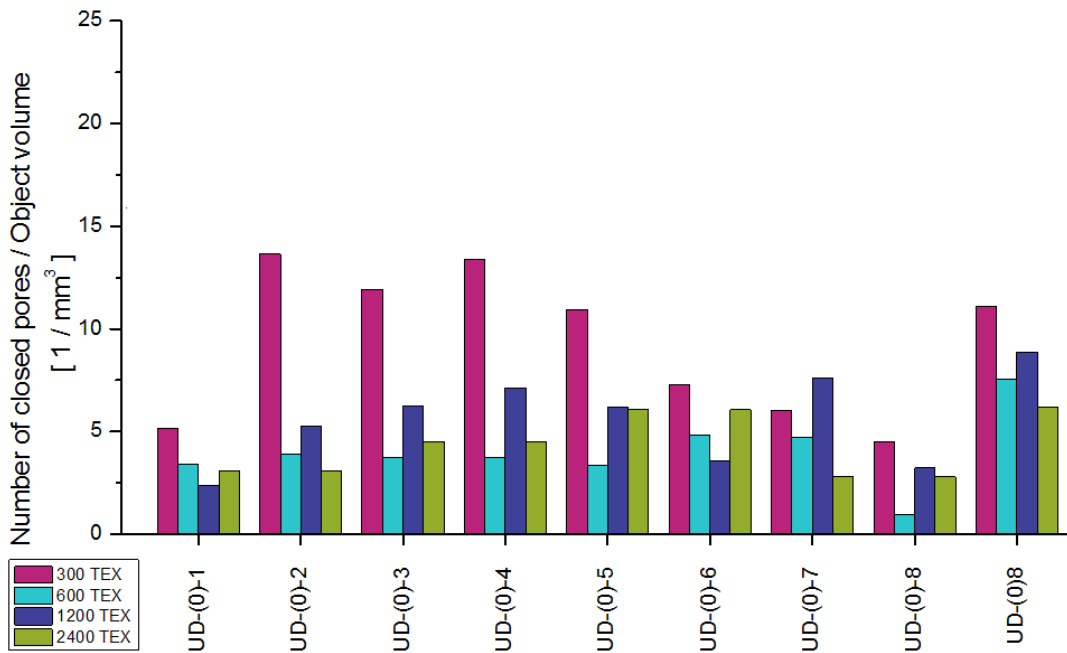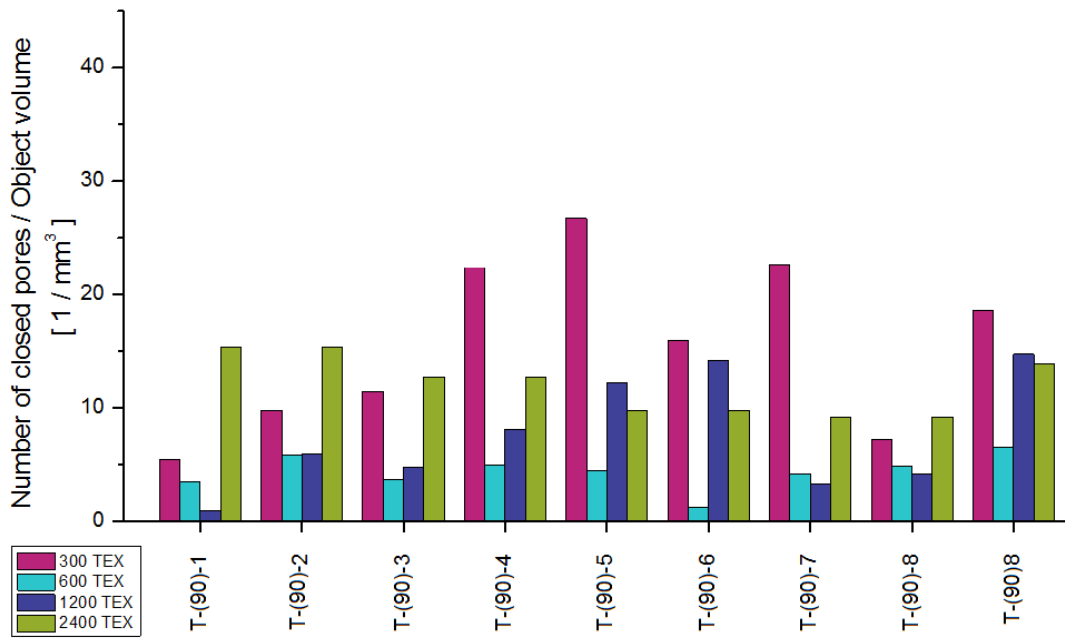Figure 2.20 The normalized cavity number inside the matrix of $(90)_8$ samples with different ROIs.
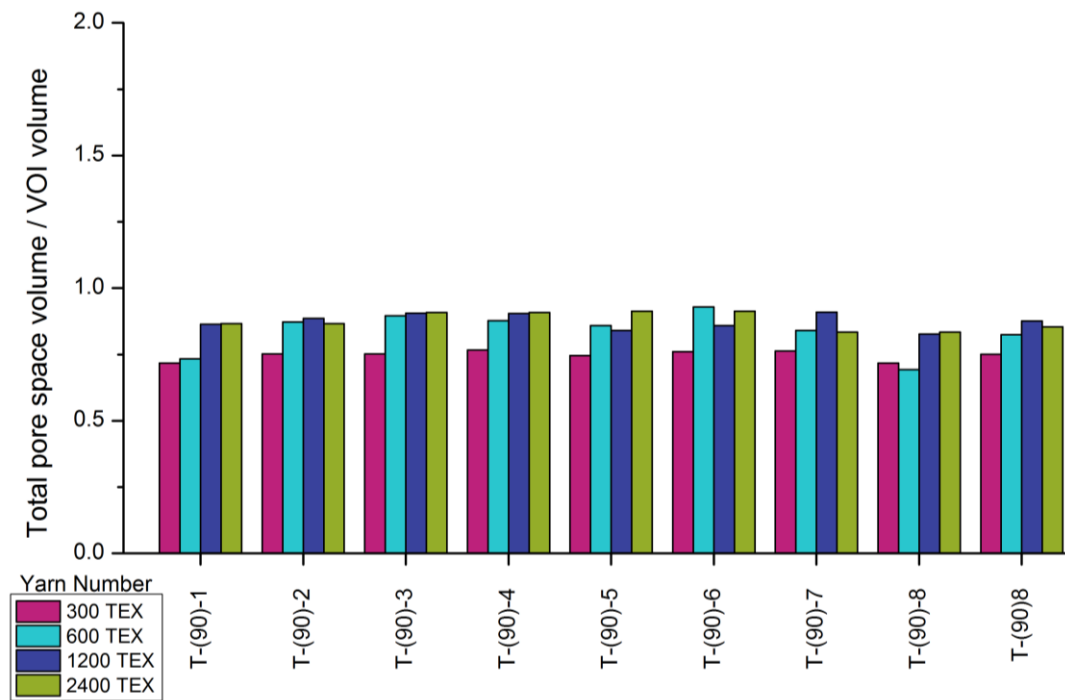
Figure 2.21 Total void (close and open pore space) volume (per total volume of interest) inside matrix part of $(90)_8$ laminated composites.

2.3.3   Tensile Performance of Cross-Ply Laminates (0/90)$_{2S}$

Tensile behavior of cross-ply laminates is investigated with various test techniques to understand the yarn number effect. The loss-on-ignition test results (Figure 2.26c) indicates that the (0/90)$_{2S}$ samples have similar fiber volume fraction and constant ply-areal weight which proves the comparison of the yarn effect on this samples to be reliable. Additionally, the cavity number which was one of the main post-processing features obtained from three-dimensional image analysis is calculated to correlate it with mechanical strength (Figure 2.26a). The cavity number of L-(0/90)2S is the lowest for the 600 TEX yarn number specimen, and the same behavior is observed for separated laminas with 0º direction. On the other hand, 90º plies are showing relatively different behavior than the 0º plies. More specifically, since the infused resin flow front moving direction was not parallel to the bundle direction, their normalized cavity numbers are higher than 0º plies on average as also noted in the study of Sisodia [40].

In addition to the cavity number calculation, eigenvector matrices for 3D images were investigated to understand the mesostructure. In detail, the principal eigenvector graph (Figure 2.28) presents that the waviness and crimping factor of ply-by-ply and laminated cross-ply composite samples. As discussed in the methodology section, if the fiber bundles were ideal rods inside the resin section, the calculation would yield the same result as discussed in methodology section: [0 0 1] eigenvector for 0º plies and [0 1 0] eigenvector for 90º plies. The misalignments in- and out- of planes of 0º and 90º plies were quantified by the principal vector values as discussed in methodology section (Figure 2.28 and Table 7). The eigenvector analysis suggests that the waviness in 0º plies is on average higher than the 90º plies. On the contrary, quantified average crimping is greater in the 90º plies than the 0º plies. Ply-by-ply analysis of the principal eigenvectors indicates that the lowest waviness and crimping is observed in 600 TEX yarn number specimens. As it is seen in Figure 2.28, the quantified waviness of unidirectional plies is sorted from highest to lowest value as 2400 TEX, 1200 TEX, 300 TEX and 600 TEX. Also, in the unidirectional case, the crimping occurs mostly in the 1200 TEX samples. Considering 90º plies, the waviness is dominant in 1200 TEX where the crimping is not as high as 2400 TEX and very close to the lowest crimping observed in 600 TEX specimens. The largest crimping and waviness is seen in the 2400

TEX specimens for 90º plies. Overall, the effect of yarn number is clearly seen on the fiber/bundle undulation as in-plane waviness and out of plane crimping. These disadvantages as observed in the laminates may lead to load transfer obstacles, complicated stress states of the bundles despite the simple one dimensional loading, leading to loss of mechanical strength, and eventuallly to preliminary failure.

Behavior under tension and initiation of failure in the $(0/90)_{2S}$ laminates were associated with the transverse cracking and as a result fiber/bundle failure at the center part of the specimen were observed. As it can be seen from Figure 2.26d, damage marks on the $0°$ plies were much more visible for the laminates of 600 TEX where the load transfer to these plies was found efficient when compared to other laminates with different yarn numbers. As a result, 600 TEX laminates were superior in strength for this sequence. A similar failure characteristic was observed for 300 TEX NCF composites while for specimens with 1200 and 2400 TEX NCF these failure marks were smaller than 600 TEX samples.

The cavity numbers within ROIs are supporting the hypothesis that strength is negatively correlated with the number of closed pores inside the specimens; in particular for 300TEX and 600 TEX specimens. This correlation leads to the conclusion that the presence of pores, accompanied by a high cavity number, causes a decrease in mechanical strength. Furthermore, the relationship between 1200 TEX and 2400 TEX in terms of cavity numbers is an indication of similar cavity existence inside their laminates; with a higher cavity number observed for 0 plies in 2400 TEX specimens and 90º plies in 1200 TEX specimens. As it seen in Figure 2.26, their mechanical strength and damage based performance are very similar, although 1200 TEX specimens are slightly superior to 2400 TEX. Along these lines, 300 TEX plies and laminate have the largest number of closed pores inside the object volume despite their mechanical strength being superior to 1200 TEX and 2400 TEX samples. The reason behind this unintuitive observation is attributed to the meso-architecture of bundles inside the laminates that allow undulation of bundles for 1200 and 2400 TEX specimens but not for 300 TEX specimens as justified with their eigenvector calculations. In other words, meso-architecture and collective arrangement of the bundles may be more dominant in driving the resulting fracture mode and strength of specimens.
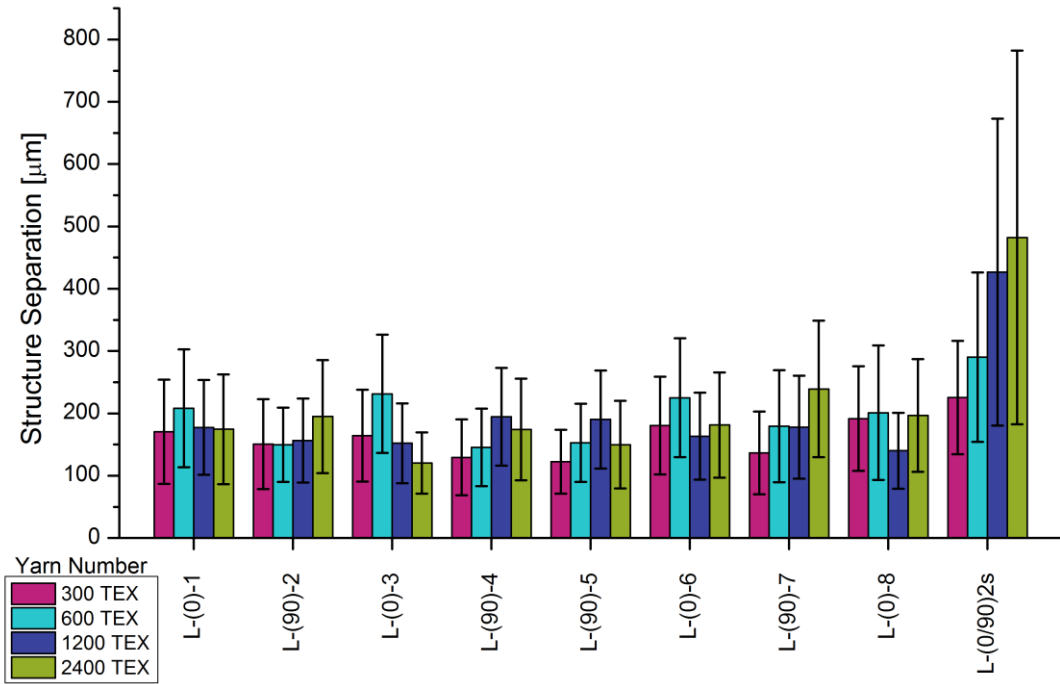
Figure 2.22 Average structure separation representation of cross-ply laminate and lay-ups with standard deviation values included.
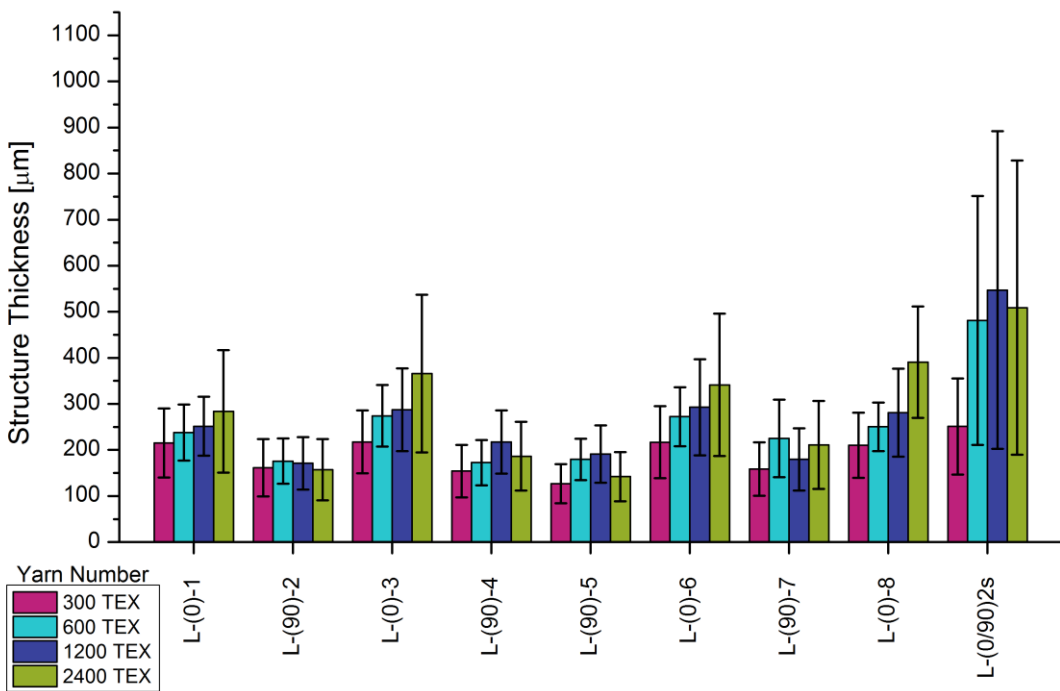
Figure 2.23 Average structure thickness representation of cross-ply laminate and lay-ups with standard deviation values included.

Table 6 Tensile strength, tensile modulus and V_f results of cross-ply laminated composites.

Yarn Number (TEX)	V_f (%)	Tensile Strength (MPa)	OHT Strength (MPa)
300	52.5	421.8±5.6	267.5±15
600	50	**503.6±6.7**	**315.9±13.6**
1200	49	357.9±5.3	265.7±17.6
2400	48	326.5±6.9	207.6±17.3
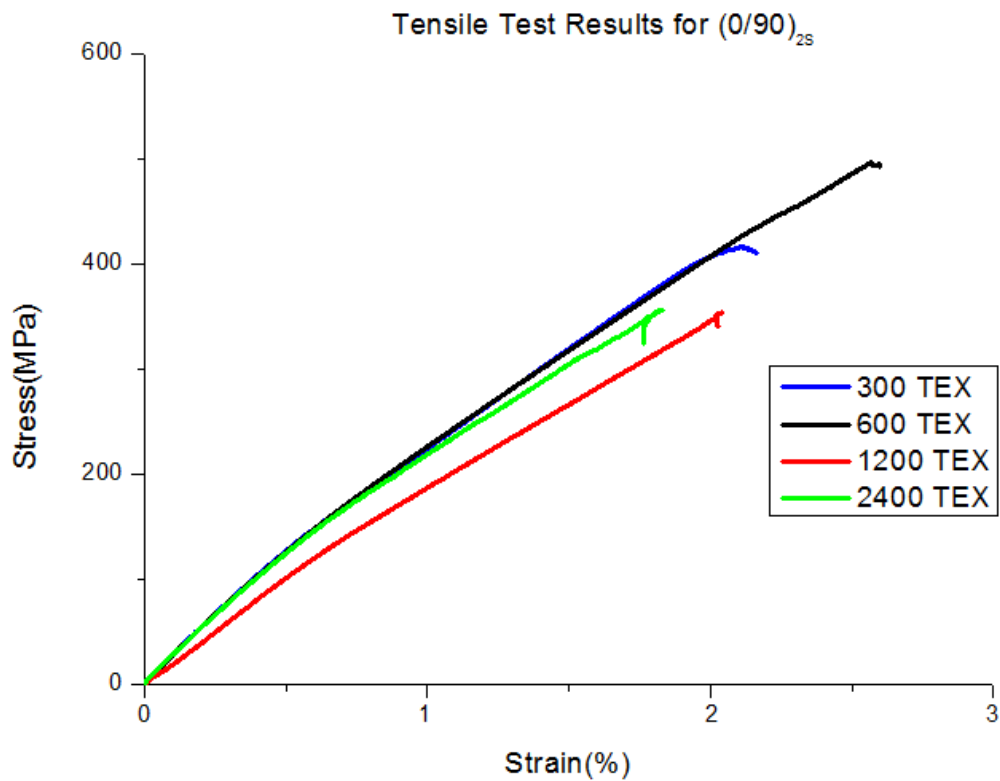
Figure 2.24 Stress-strain curves of cross-ply laminated composites under tension.
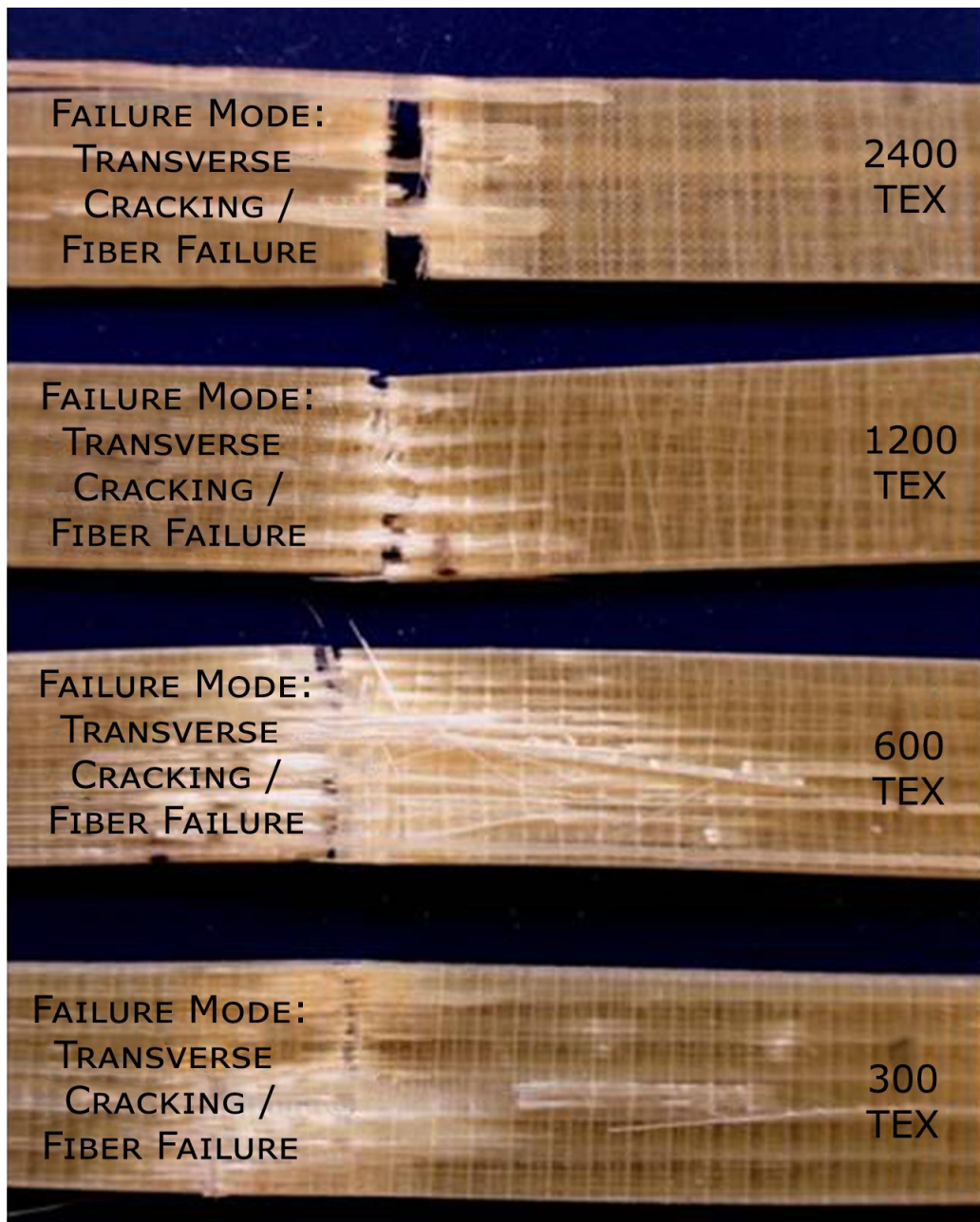
Figure 2.25 Failure modes and images of cross-ply laminated composites after failure.
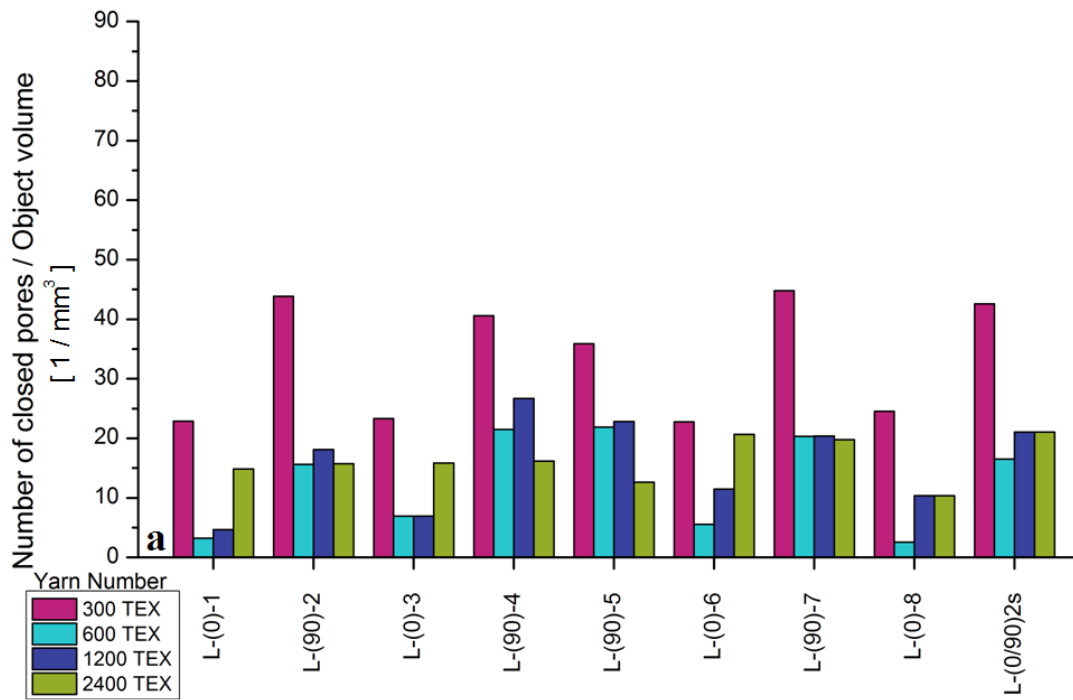
Figure 2.26 The normalized cavity number of cross-ply composite samples with different ROIs.
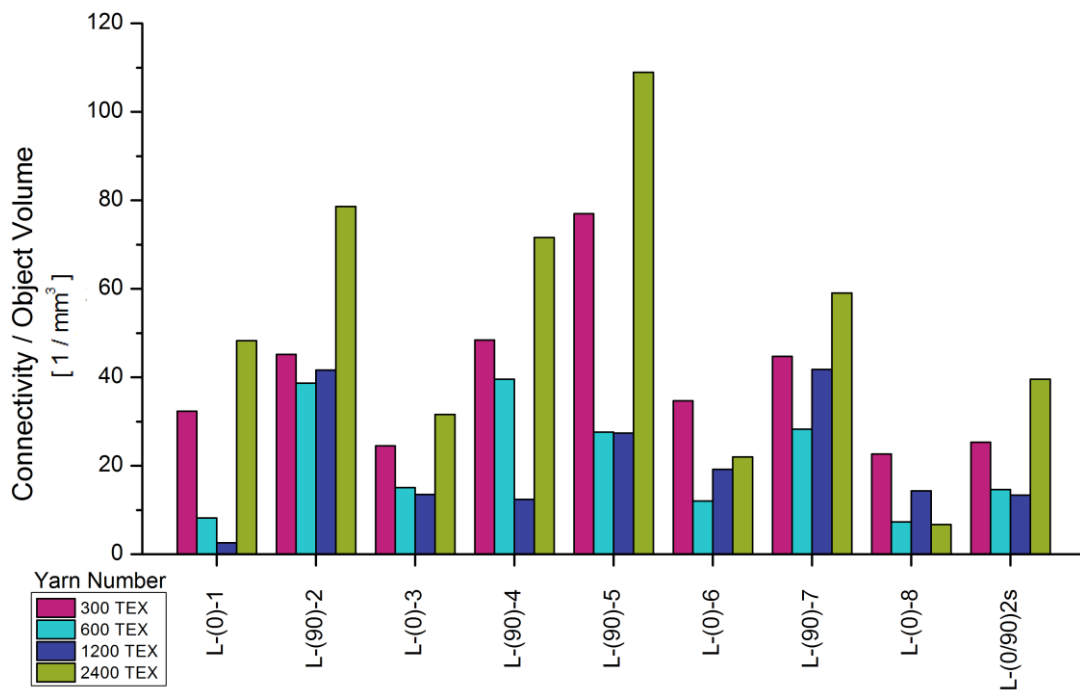
Figure 2.27 Connectivity density of cross-ply laminates and lay-ups.
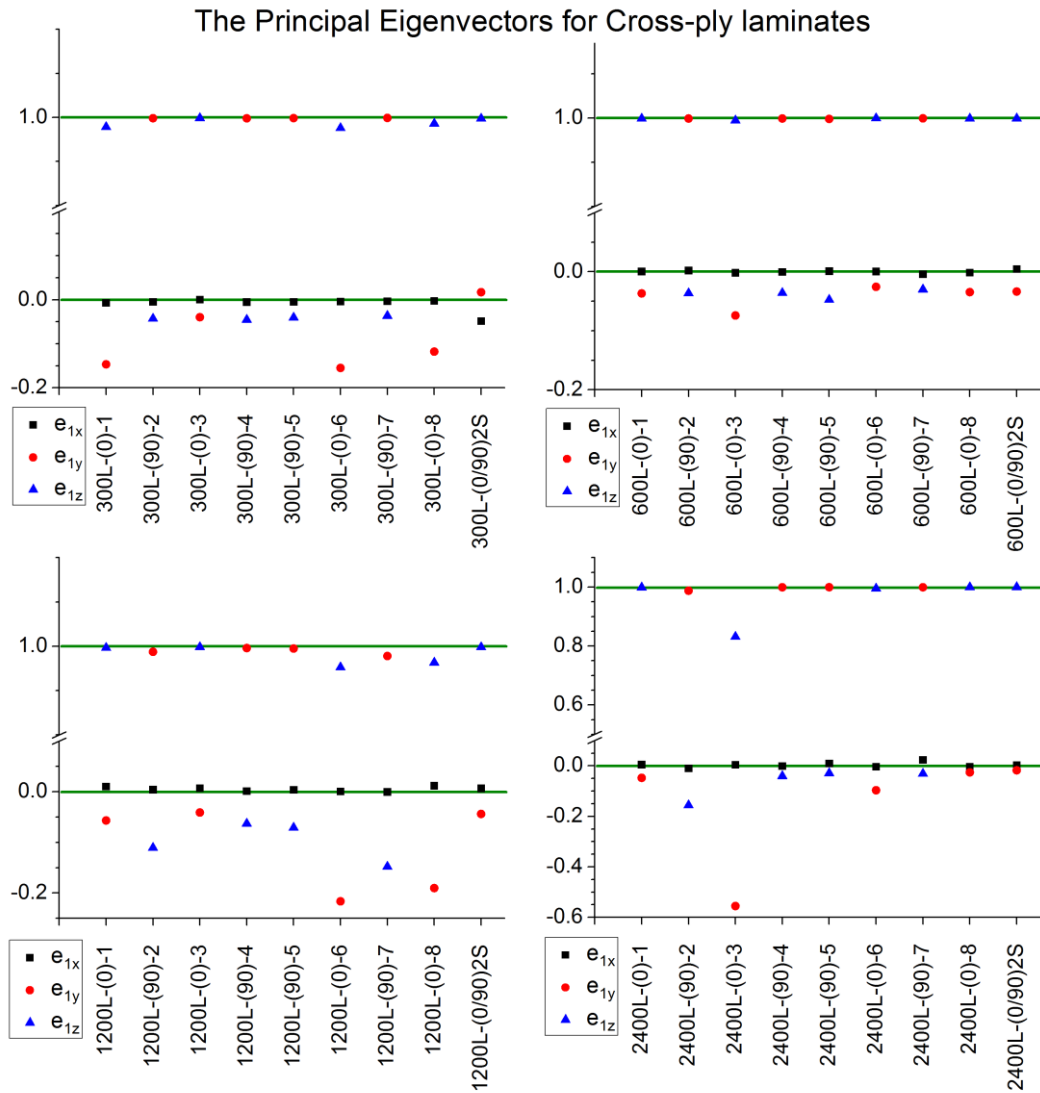
Figure 2.28 The principal eigenvectors of for cross-ply laminates and lay-ups.

The principal eigenvector components deserve further discussion. Recalling the vector of prime interest being $[e_{1x} \ e_{1y} \ e_{1z}]$, where subscript 1 refers to material dominant (fiber) direction, it can be stated that for unidirectional (0º) plies the dominant direction is $[e_{1x} \ e_{1y} \ e_{1z}] = [e_{zx} \ e_{zy} \ e_{zz}]$ and for transversal (90º) plies the dominant direction is $[e_{1x} \ e_{1y} \ e_{1z}] = [e_{yx} \ e_{yy} \ e_{yz}]$. The distance of blue and red dots from the green lines shows the imperfections (undulations). Specifically, waviness (in-plane undulations) and crimping (out-of-plane undulations) are quantified through the principal eigenvector components represented in Figure 2.28.

Table 7 Quantified waviness and crimping values for cross-ply laminates.

Yarn Property (TEX)		L-(0)-1	L-(0)-3	L-(0)-6	L-(0)-8	Average
300	Waviness	0.14658	0.0396	0.15493	0.11763	0.114685
600	Waviness	0.03677	0.0741	0.02555	0.03455	0.0427425
1200	Waviness	0.05685	0.04097	0.2163	0.19019	0.1260775
2400	Waviness	0.04787	0.55538	0.09663	0.02606	0.181485
300	Crimping	0.00686	0.00014	0.00407	0.00293	0.0035
600	Crimping	0.00033	0.00169	0.00031	0.00158	0.0009775
1200	Crimping	0.01022	0.00713	0.00037	0.0117	0.007355
2400	Crimping	0.00495	0.00397	0.00325	0.00347	0.00391
Yarn Property (TEX)		L-(90)-2	L-(90)-4	L-(90)-5	L-(90)-7	Average
300	Waviness	0.04286	0.04529	0.0403	0.03627	0.04118
600	Waviness	0.03631	0.03193	0.04741	0.02987	0.03638
1200	Waviness	0.11069	0.06279	0.07071	0.14782	0.0980025
2400	Waviness	0.1558	0.04046	0.02922	0.03103	0.0641275
300	Crimping	0.00489	0.00533	0.00465	0.00331	0.004545
600	Crimping	0.00218	0.00042	0.00104	0.00439	0.0020075
1200	Crimping	0.00393	0.00132	0.00384	0.00043	0.00238
2400	Crimping	0.00995	0.00127	0.00968	0.0235	0.0111
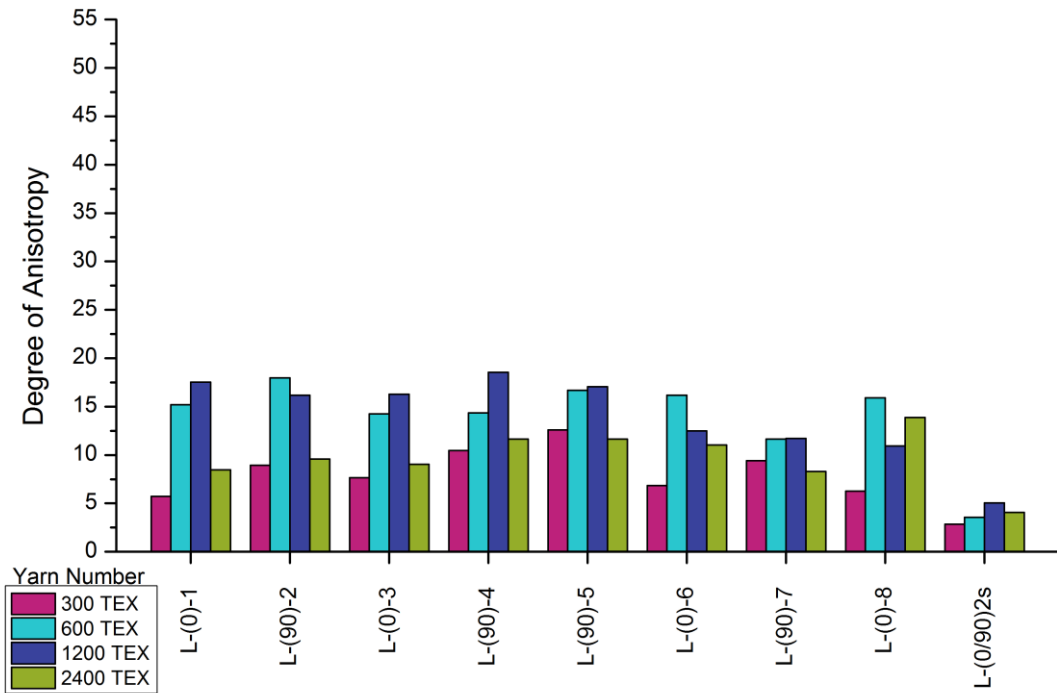
Figure 2.29 Calculated degree of anisotropy for cross-ply laminates and lay-ups.
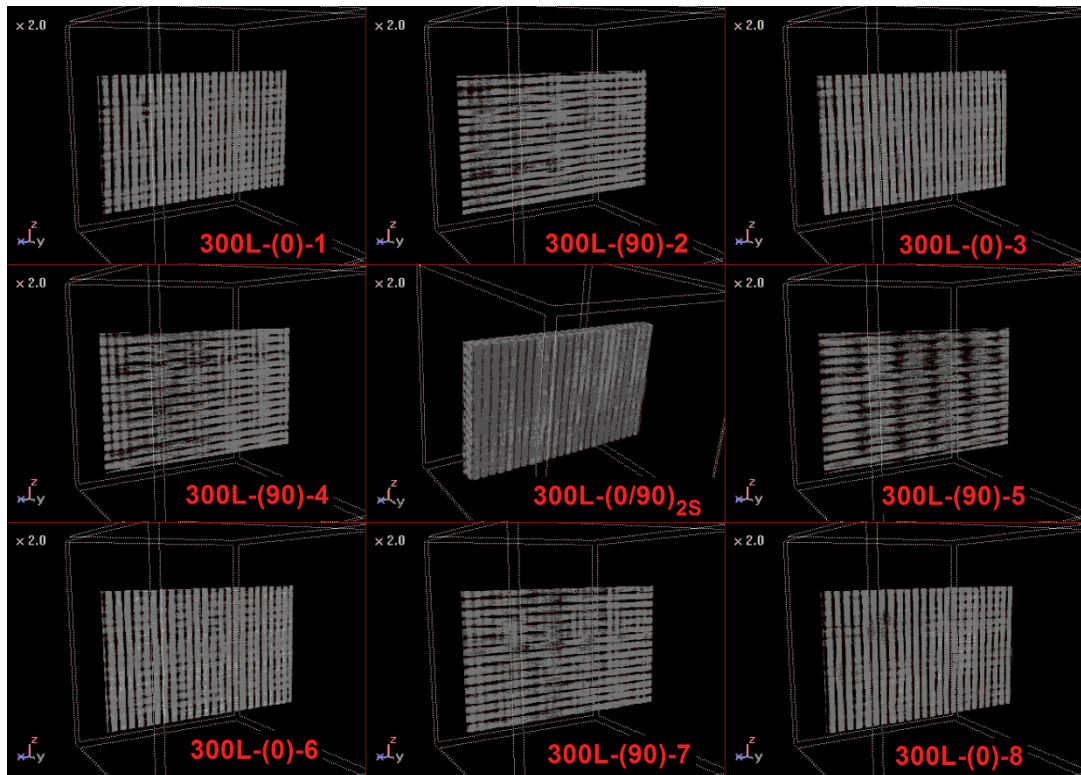
Figure 2.30 Reconstructed 3D images of cross-ply 300 TEX specimen labeled as plies and laminate.
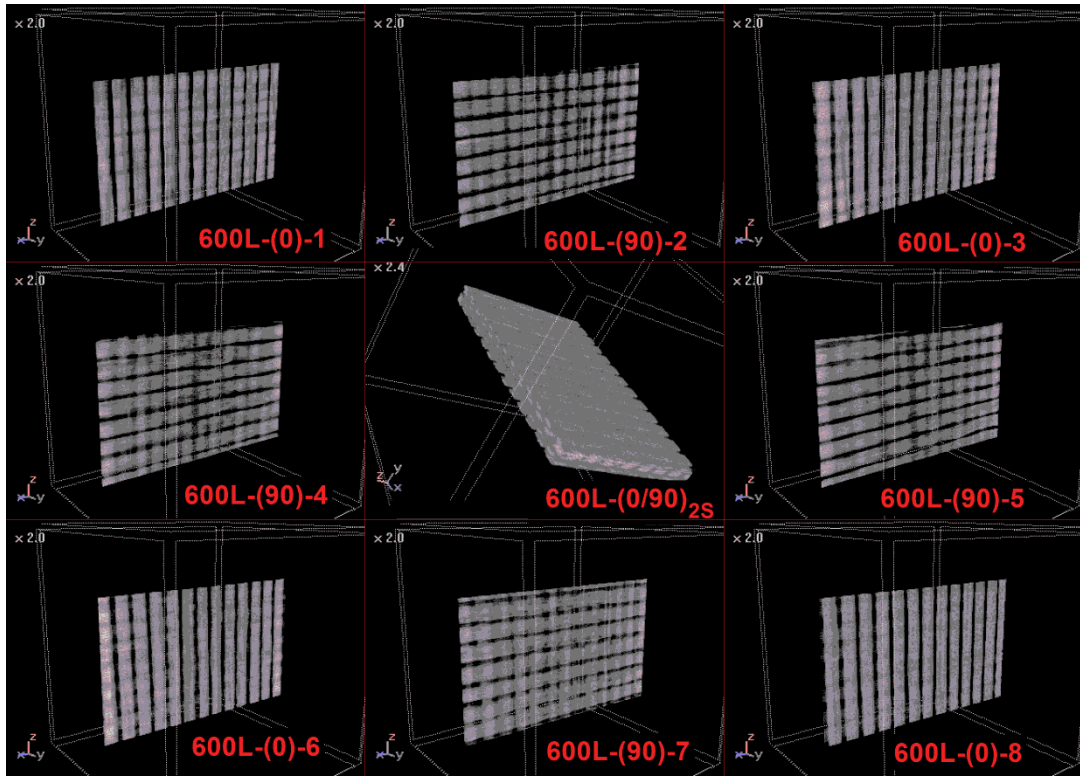
Figure 2.31 Reconstructed 3D images of cross-ply 600 TEX specimen labeled as plies and laminate.
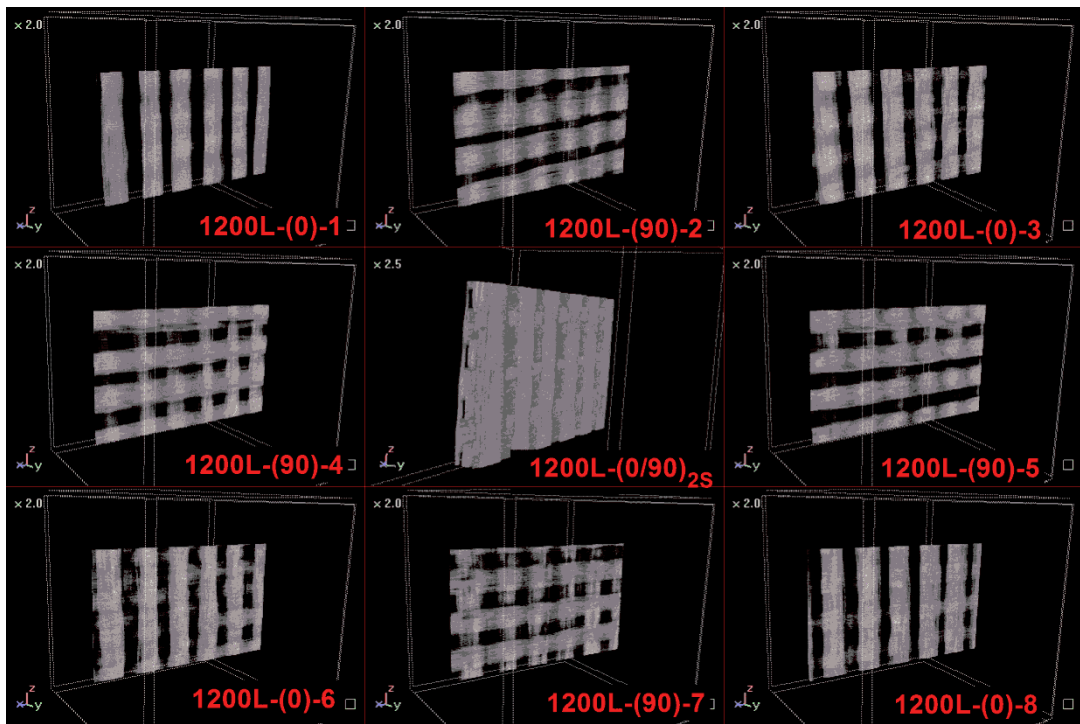
Figure 2.32 Reconstructed 3D images of cross-ply 1200 TEX specimen labeled as plies and laminate.

Figure 2.33 Reconstructed 3D images of cross-ply 2400 TEX specimen labeled as plies and laminate.

2.3.4   In-plane Shear Performance of Composite Laminates (+45/-45)$_{2S}$

The unique failure of [+45/-45]$_{4S}$ laminates under uniaxial tension was dominated by a non-linear behavior following an initial elastic deformation region. Fracture of all the laminates occurred at the midsection and with an angle around 45˚, in the form of a typical shear failure (Figure 2.38b). In the scope of the work, the non-linearity of the stress-stain curves (Figure 2.38d) was observed to be very sensitive to the yarn number of the reinforcement.

The stress-strain curves suggested that the ability to undergo the scissoring like effect via fiber and bundle realignments and overall mechanical behavior were both affected by the yarn number, the associated bundle width, inter-bundle distance, and structure separation. For instance, for (+45/-45)$_{2S}$ laminates that are containing small bundle width and inter-bundle size (such as 300 TEX), the elastic region was followed by a plastic deformation during which the load increase continued till the onset of local permanent deformations via neck formation before failure. On the contrary, the plastic

deformation-like behavior of specimens with 600 TEX was notably more extensive than the ones with 300 TEX. Similar to the samples of 600 TEX, specimens of 1200 TEX were also able to go through extensive plastic deformation before the fracture. However, 1200 TEX specimens were unable to carry higher stress while deforming plastically unlike 600 TEX samples. On the other hand, specimens with 2400 TEX have gone through an early failure at the end of a similar plastic behavior which represents the inefficiency of load transfer capability under shear loading. These differences are mainly attributed to the tendency of fiber bundles to move in-situ, towards the loading direction causing a scissoring effect inside the test specimen.

In addition to the bundle width and interbundle dimension difference between different yarn number NCF composite specimens, the meso-architecture difference between laminates are responsible in differences of the plastic deformation behavior. Because of the scissoring effect inside the specimen during loading, the bundle directions and principal directions of the ply-laminas may affect the nature of plastic deformation. Regarding three-dimensional image analysis results for structure separation in comparison to interbundle distance; as expected the structure separation value increase in parallel to the bundle to bundle distance with the yarn number value of NCF composite (Figure 2.34 and Figure 2.35). Also, the connectivity density (Figure 2.39) shows that during the lamination process, the connected areas of 2400 TEX specimens are higher than other yarn numbers. Moreover, 300 TEX specimen is more connected than 600 TEX specimen since the number of connection made inside the laminate is more than 600 TEX specimen in the same areal weight (Figure 2.42, Figure 2.43, and Figure 2.45). Nevertheless, to understand the meso-architecture of the samples, principal directions in between ply-laminas need to be investigated (Figure 2.40). Principal MIL for $(+45/-45)_{2S}$ plies shows that the directions of the laminas maintain separable in 300 TEX and 600 TEX specimens. However, the principal MIL direction lost its symmetry and wideness for 2400 TEX specimen where it was almost impossible to detect and separate lamina direction. Also, more undulations were quantified for structures with higher yarn numbers such as 1200 TEX and 2400 TEX (Table 9). Further judgment on analysis may be done by looking at the 3D images constructed for separated laminas and composite laminates.
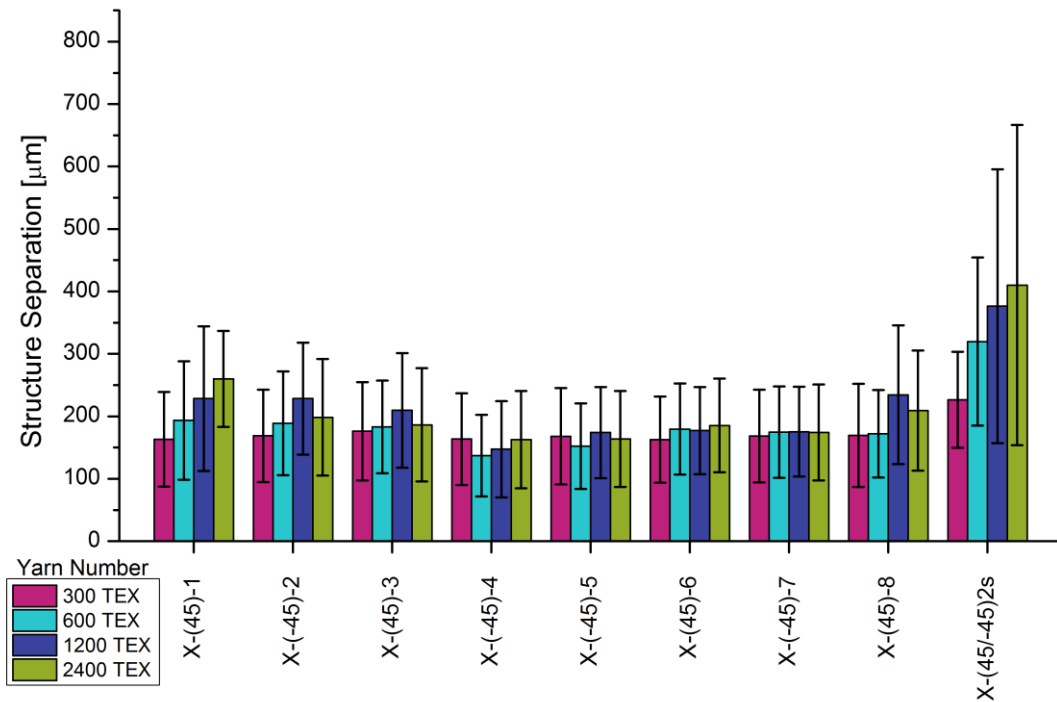
Figure 2.34 Average structure separation representation of (+45/-45)$_{2S}$ laminate and lay-ups with standard deviation values included.
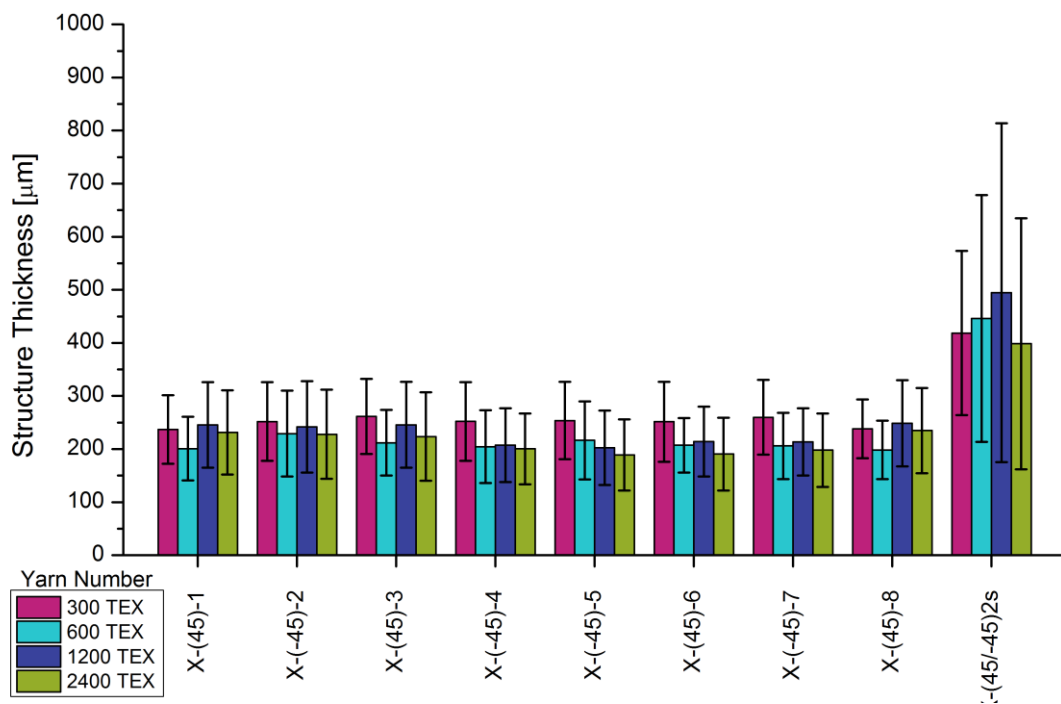
Figure 2.35 Average structure thickness representation of (+45/-45)$_{2S}$ laminate and lay-ups with standard deviation values included.

Table 8 Tensile strength, tensile modulus and V_f of $(+45/-45)_{2S}$ laminated composites.

Yarn Number (TEX)	V_f (%)	Tensile Strength (MPa)	Tensile Modulus (MPa)
300	50	62.9±3.4	6.9±0.6
600	53	**72.4±2.2**	6.9±0.8
1200	52	56.8±1.5	5.4±0.7
2400	49	42.5±2.0	5±0.9
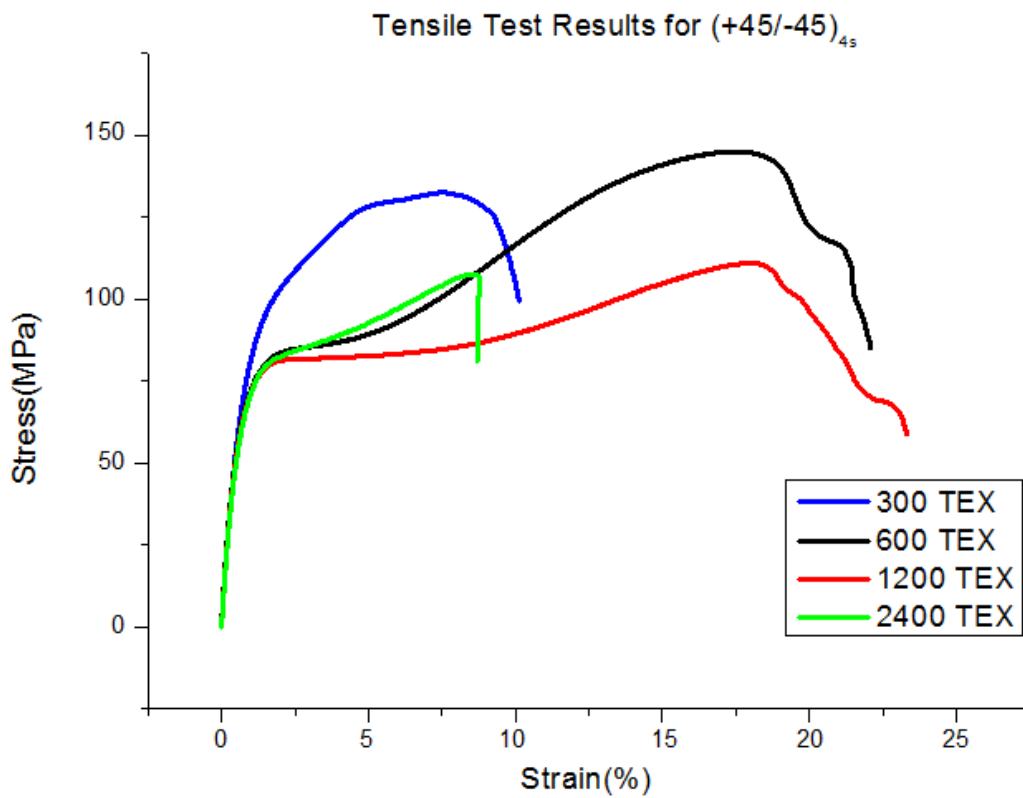
Figure 2.36 Stress-strain curves of $(+45/-45)_{2S}$ laminated composites under tension.
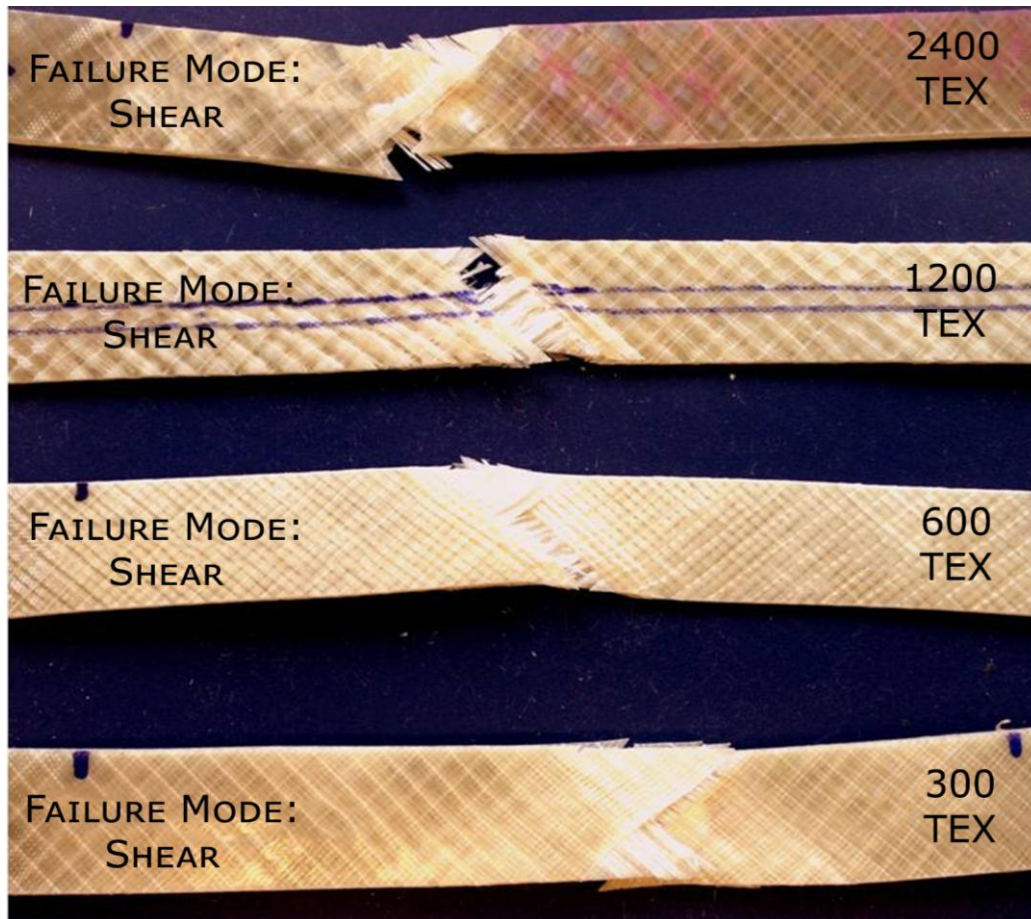
Figure 2.37 Failure modes and images of (+45/-45)$_{2S}$ laminated composites after failure.
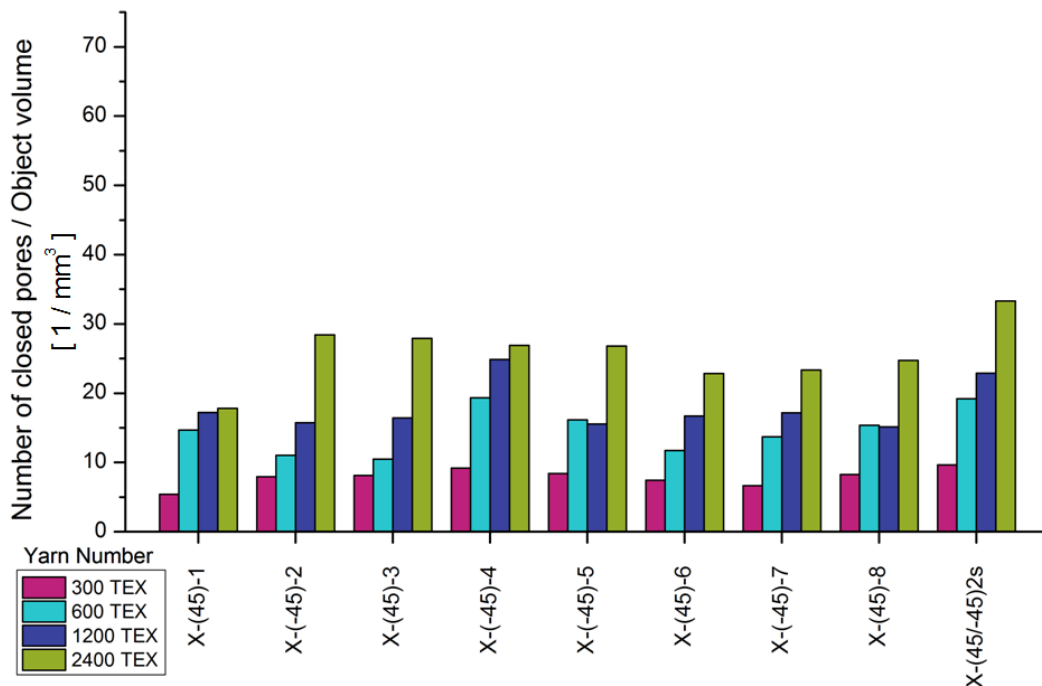
Figure 2.38 The normalized cavity number of (+45/-45)$_{2S}$ samples with different ROIs.
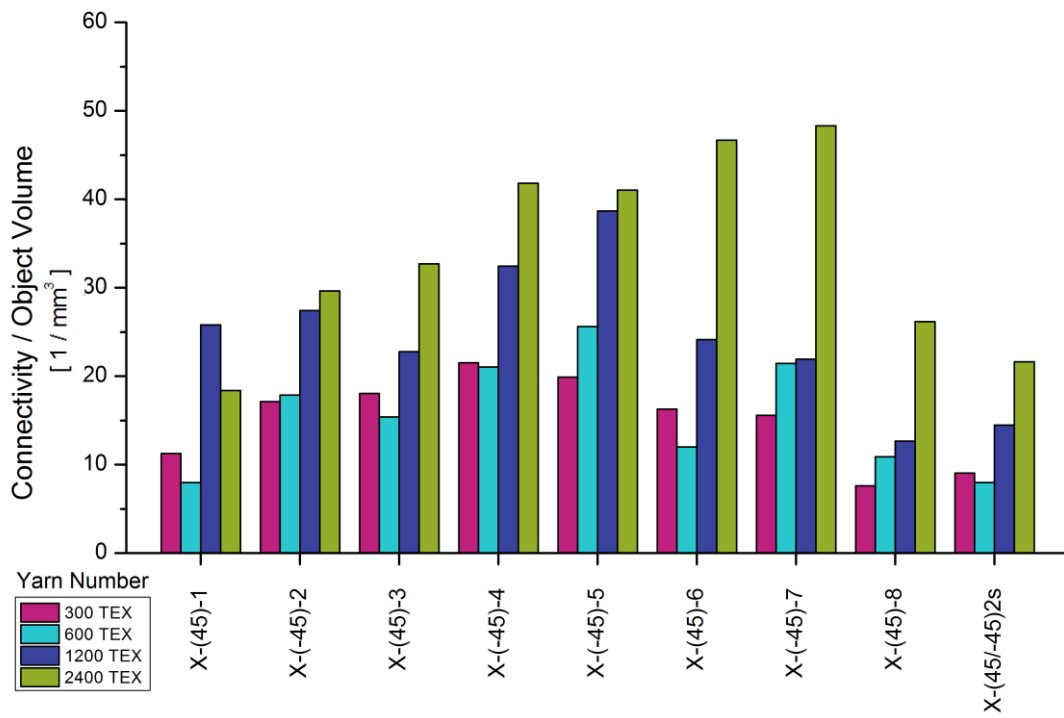
Figure 2.39 Connectivity density of (+45/-45)$_{2S}$ laminates and lay-ups.
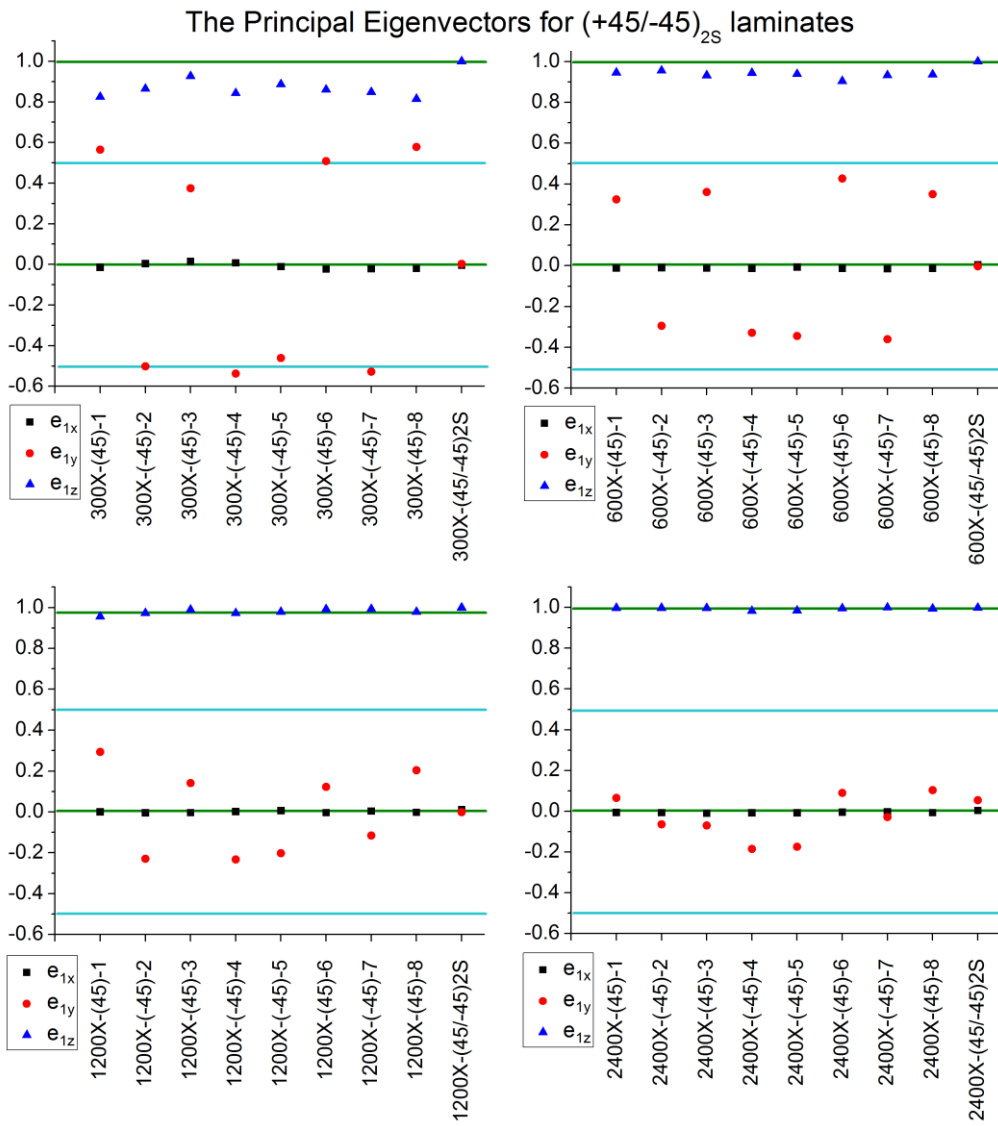
Figure 2.40 Principal eigenvectors of (+45/-45)$_{2S}$ laminates and lay-ups.

Table 9 Quantified waviness and crimping values for (+45/-45)$_{2S}$ laminates.

Yarn Property (TEX)		X-(45)-1	X-(45)-3	X-(45)-6	X-(45)-8	Average
300	Waviness	0.06481	0.12525	0.00878	0.07858	0.069355
600	Waviness	0.17523	0.13879	0.07326	0.14951	0.1341975
1200	Waviness	0.20639	0.35849	0.37722	0.29588	0.309495
2400	Waviness	0.43423	0.56941	0.4096	0.3964	0.45241
300	Crimping	0.0148	0.0144	0.0224	0.0203	0.0180
600	Crimping	0.01211	0.01194	0.01232	0.01221	0.012145
1200	Crimping	0.00064	0.00321	0.00349	0.00192	0.002315
2400	Crimping	0.00587	0.00999	0.00406	0.00629	0.0065525
Yarn Property (TEX)		X-(-45)-2	X-(-45)-4	X-(-45)-5	X-(-45)-7	Average
300	Waviness	0.00148	0.03745	0.0392	0.0282	0.0265825
600	Waviness	0.20557	0.1715	0.15588	0.14012	0.1682675
1200	Waviness	0.27078	0.26748	0.29823	0.38452	0.3052525
2400	Waviness	0.43607	0.31523	0.32607	0.47183	0.3873
300	Crimping	0.00404	0.00763	0.01085	0.02109	0.0109025
600	Crimping	0.0095	0.01246	0.00701	0.01409	0.010765
1200	Crimping	0.00385	0.00194	0.00681	0.0044	0.00425
2400	Crimping	0.00641	0.00755	0.00406	0.00629	0.0060775
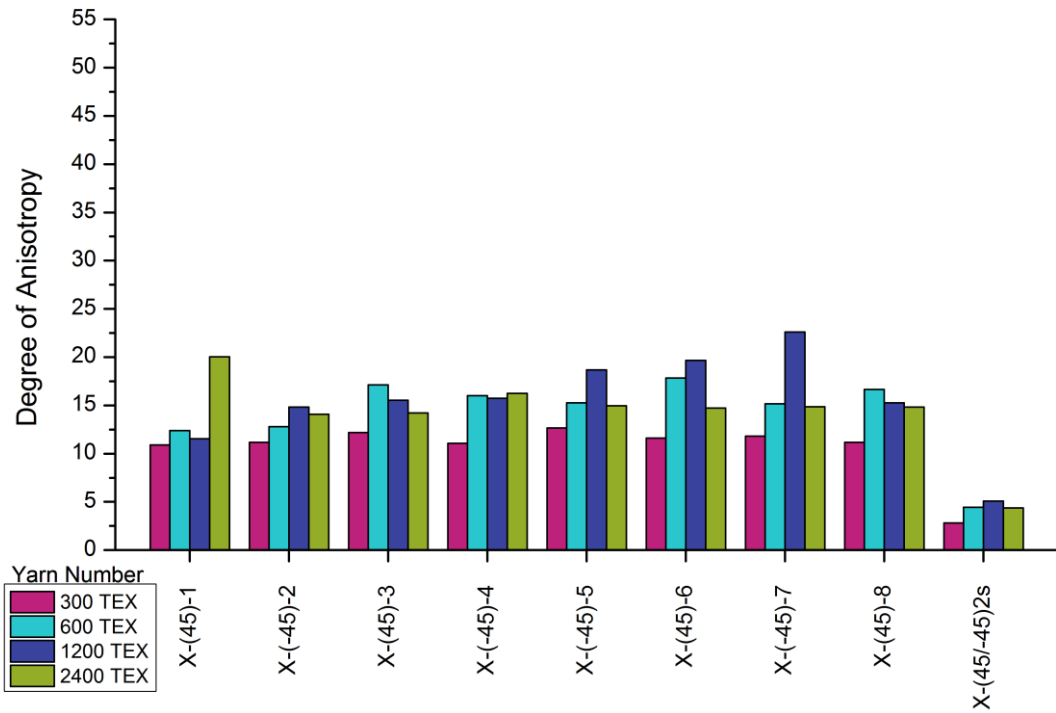
Figure 2.41 Calculated degree of anisotropy of $(+45/-45)_{2S}$ laminate and lay-ups.

Figure 2.42 Reconstructed 3D images of $(+45/-45)_{2S}$ 300 TEX specimen labeled as plies and laminate.

Figure 2.43 Reconstructed 3D images of (+45/-45)$_{2S}$ 600 TEX specimen labeled as plies and laminate.
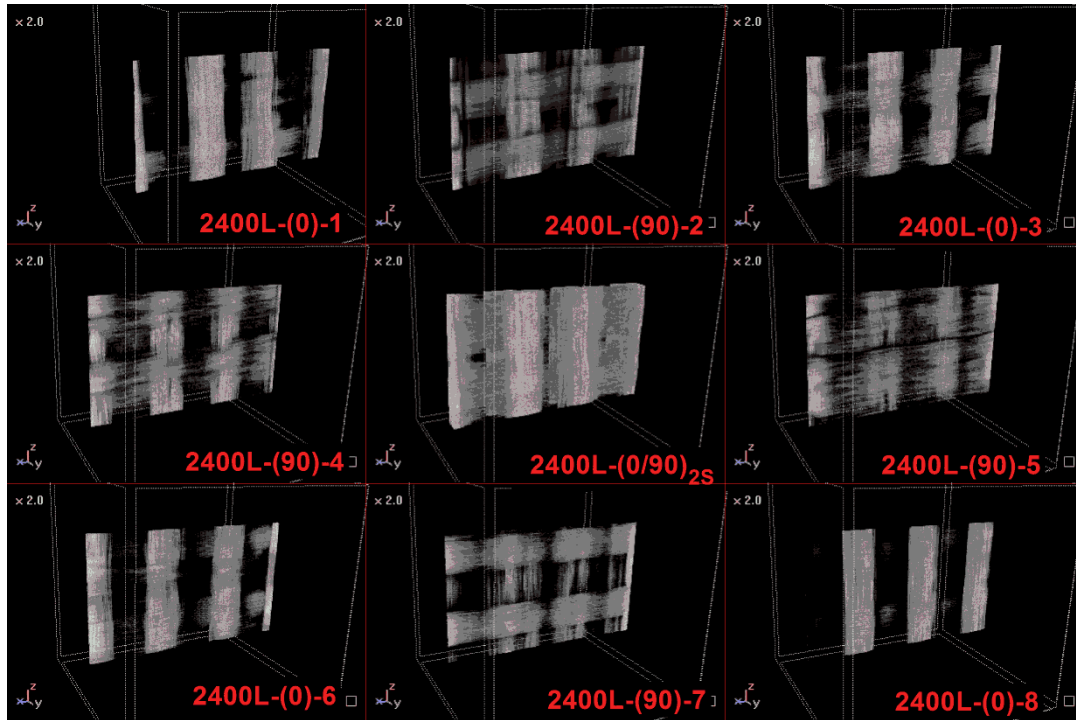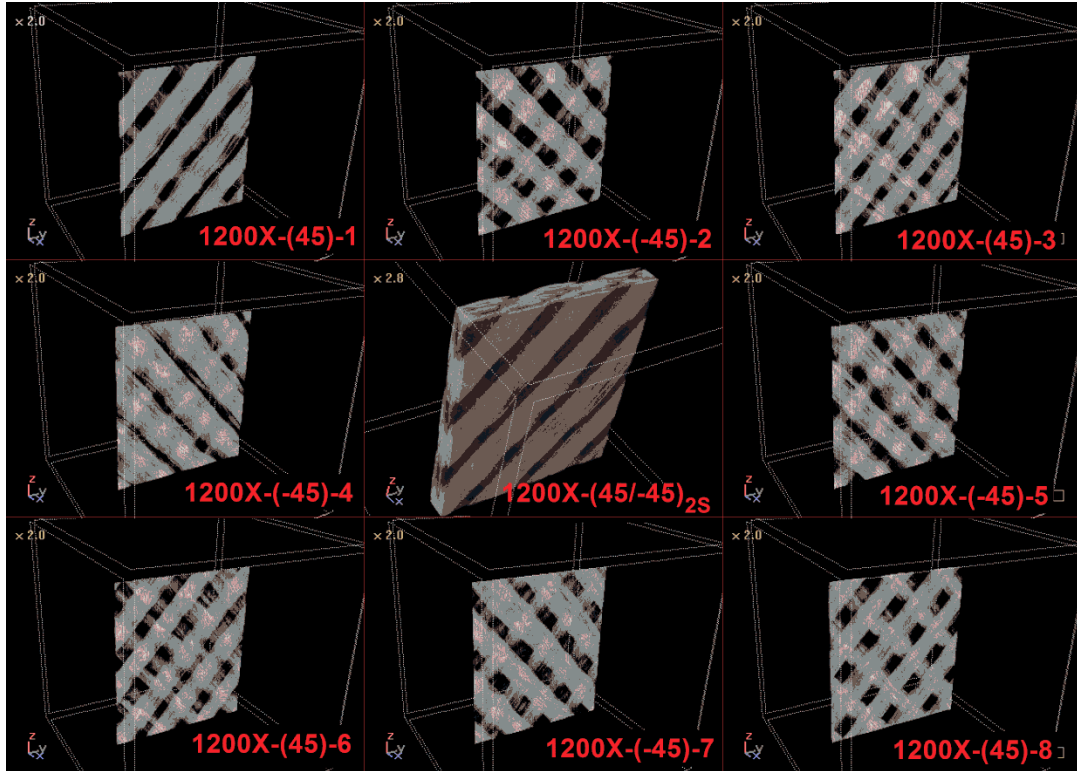

Figure 2.44 Reconstructed 3D images of (+45/-45)$_{2S}$ 1200 TEX specimen labeled as plies and laminate.
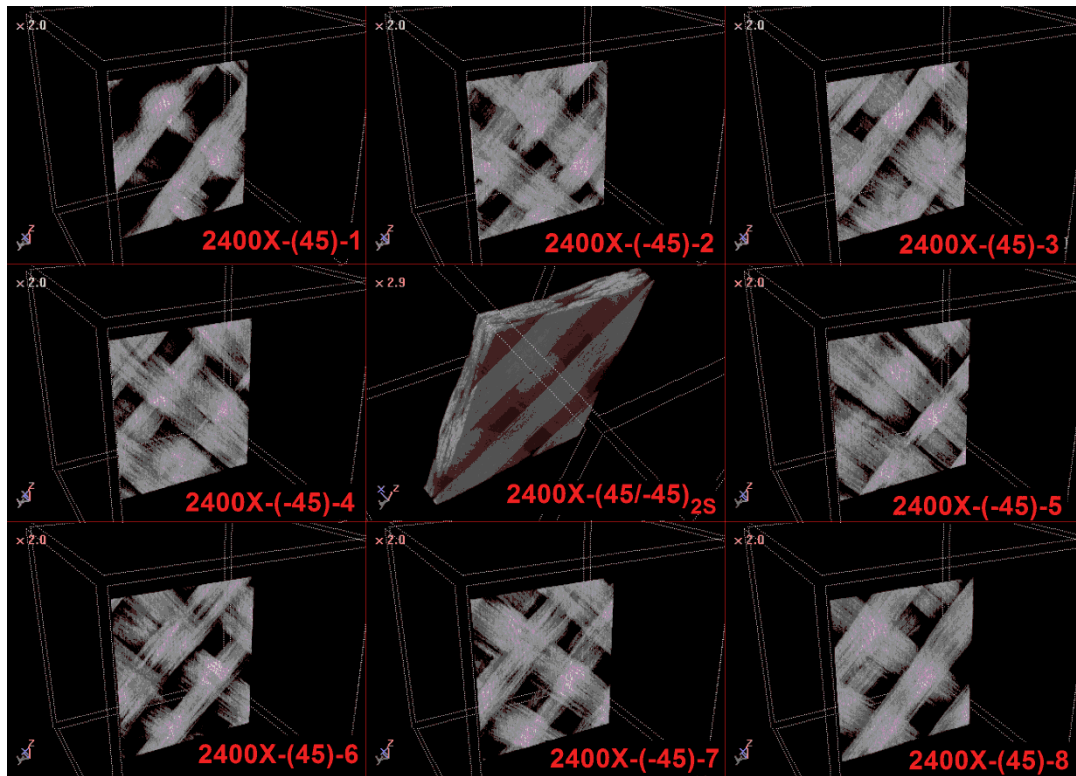
Figure 2.45 Reconstructed 3D images of (+45/-45)₂ₛ 2400 TEX specimen labeled as plies and laminate.

2.3.5 Tensile Performance of Quasi-isotropic Composite Laminates (0/+45/-45/90)ₛ

As a potential combination of all the observed effects, quasi-isotropic laminates contain 0 °, 90° and ±45° plies. Since the yarn number and its interaction with the fiber orientation changes from one ply to the other which were significant as observed in the in-situ behavior of each ply, the failure modes of the quasi-isotropic laminate were also worth to observe and discuss. As it can be seen from Figure 2.46b, the failure mode was dominated by severe shear and delamination failure. The ability of specimens with 600 TEX yarn number to deform under shear was significant as observed in their performance (Figure 2.50) when compared with samples with 300 TEX yarn number. In accordance with previous observations 1200 and 2400 TEX NCF reinforced specimens were not dominated by matrix cracks but resulted in detacthed fiber splitting before the ultimate failure.

By looking at the 3D image analysis of the quasi-isotropic case, one may expect to see isotropic behavior through the laminate. In principal MIL direction analysis and degree of anisotropy calculations compared to the other stacking sequences show that specimens of quasi-isotropic laminates have quite low values for degree of anisotropy (as a design constraint), although fully isotropic structures are not achieved (Figure 2.52 and Figure 2.53). The results of the degree of anisotropy calculation indicate that there are still anisotropic parts inside the three-dimensional image.

Another post-processing property, connectivity density estimation, shows that the connectivity number through the layers (ply-by-ply distribution) shows symmetrical pattern: increasing from the top and the bottom (Q-(0)-1 and Q-(0)-8) laminae with connectivity reaching relatively higher values at mid-plane (Q-(90)-4 and Q-(90)-5) (Figure 2.51). However, 600 TEX specimens have really low values without diplaying symmetry as evident in the graph (Figure 2.52). It also follows based on the laminates that 600-Q-(0/+45/-45/90)$_S$ has abnormally low connectivity.

Based on the structure separation calculations, it follows a linear increase while yarn number of specimen gets higher (Figure 2.46). This correlation shows that the impregnation process completed successfully. On the other hand, structure thickness evaluation indicates that the average thickness for 2400TEX specimens is relatively lower than the other yarn number choices (Figure 2.47). The behavior can be explained in terms of the uncertainties induced by manual image separations as evident in Figure 2.54, Figure 2.55, Figure 2.56, and Figure 2.57. Since the mechanical behavior of the quasi-isotropic laminate is complicated and the separation of 2400 TEX lay-ups is hard and prone to analysis errors due to high structure separation and unexpected undulations (Figure 2.52), the structure thickness results seem to be unexpectedly low.

The lowest cavity number is calculated for 600 TEX specimens, and highest connectivity number is evaluated for 300 TEX and 2400 TEX samples within the quasi-isotropic case as a combination of the other cases (Figure 2.50a). The correlation of the mechanical strength and cavity number as explained above causes the preliminary failure of large yarn number specimens in addition to the mesostructure effect.
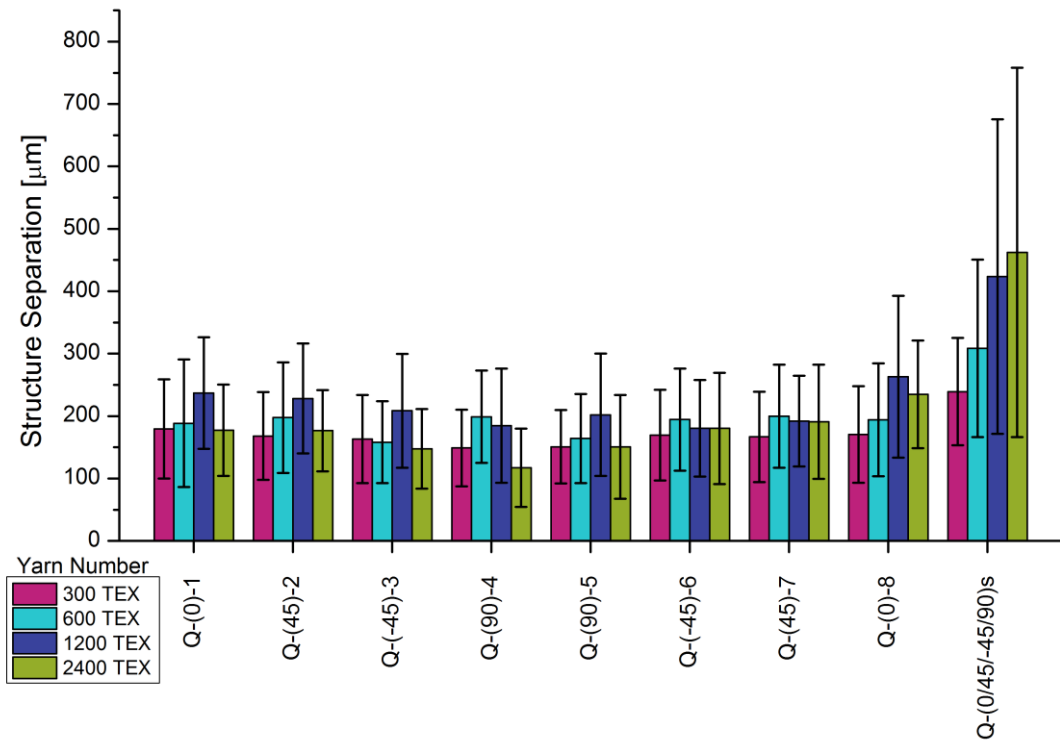
Figure 2.46 Average structure separation representation of quasi-isotropic laminate and lay-ups with one sigma deviation.
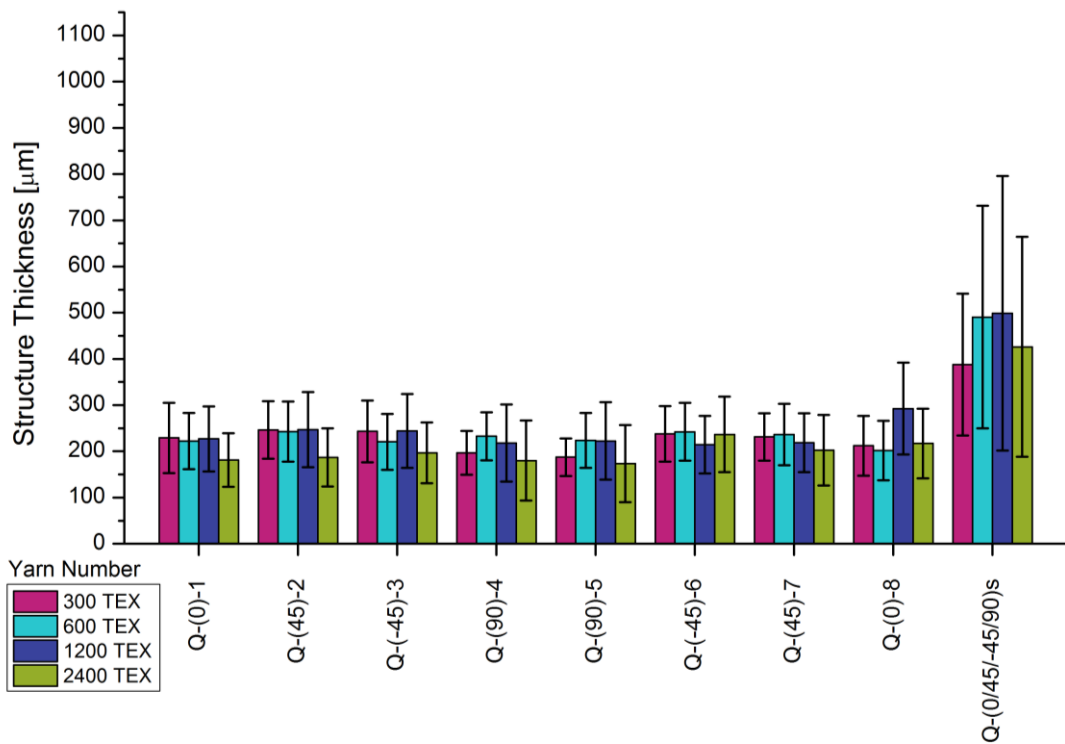
Figure 2.47 Average structure thickness representation of quasi-isotropic laminate and lay-ups with one sigma deviation.

Table 10 Tensile strength, open-hole-tension strength, and V_f of quasi-isotropic laminated composites.

Yarn Number (TEX)	V_f (%)	Tensile Strength (MPa)	OHT Strength (MPa)
300	52	315.5±7.5	208.1±8.9
600	51	**360.1±8.2**	**247.6±5.0**
1200	48	292.8±9.0	206.1±9.3
2400	47	187.9±5.2	179.1±3.0
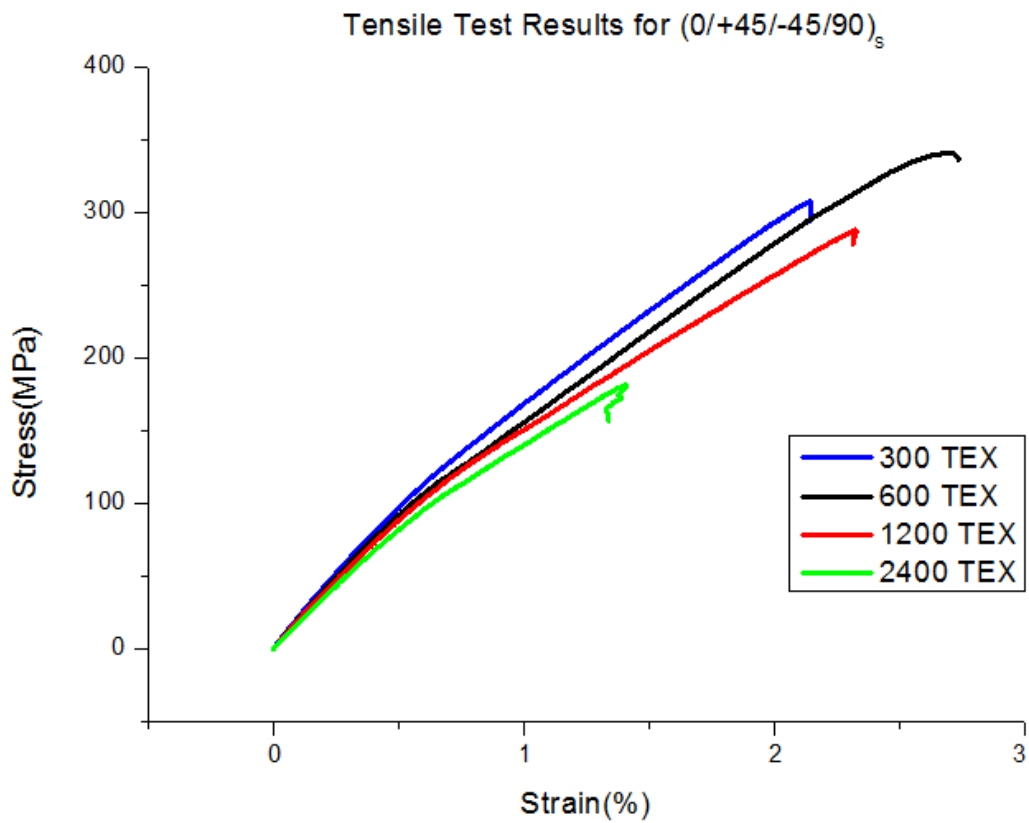
Figure 2.48 Stress-strain curves of quasi-isotropic laminated composites under tension.

Figure 2.49 Failure modes and images of quasi-isotropic laminated composites after failure.
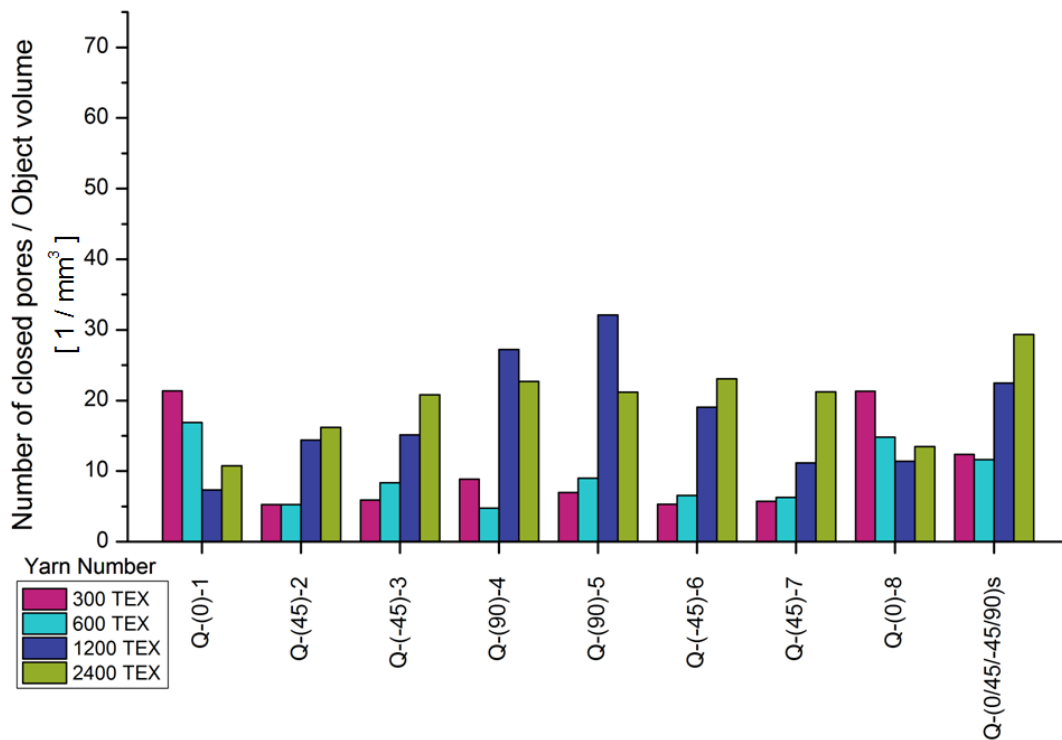
Figure 2.50 The normalized cavity number of quasi-isotropic samples with different ROIs.
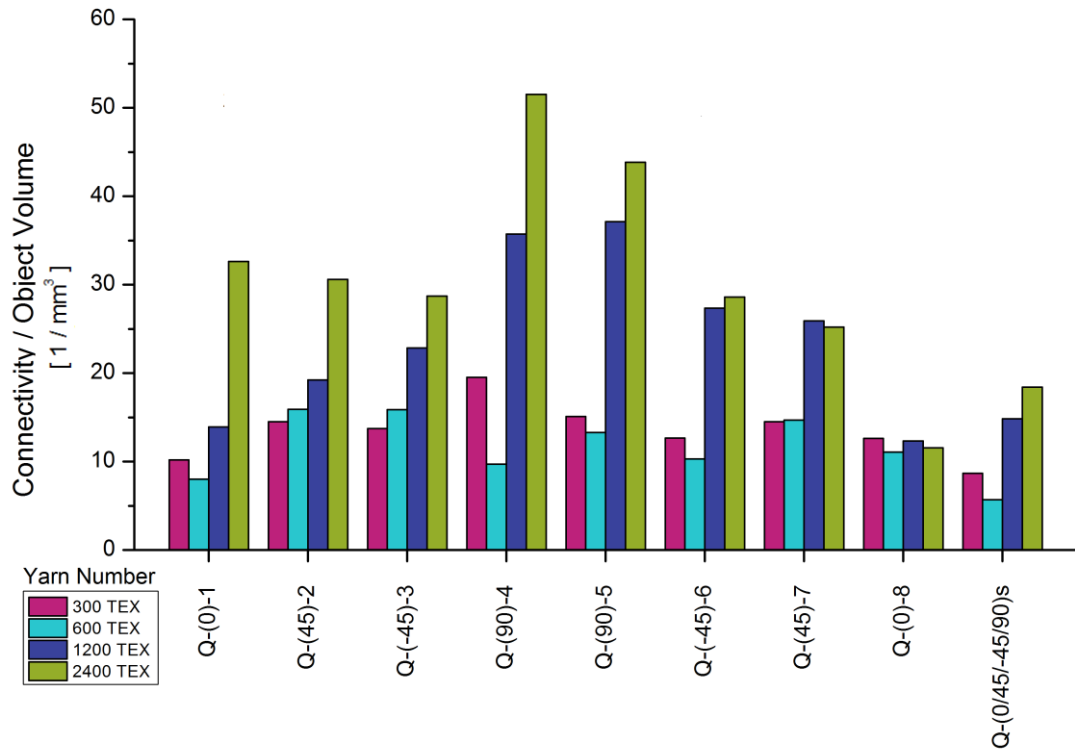
Figure 2.51 Connectivity density of quasi-isotropic laminates and lay-ups.
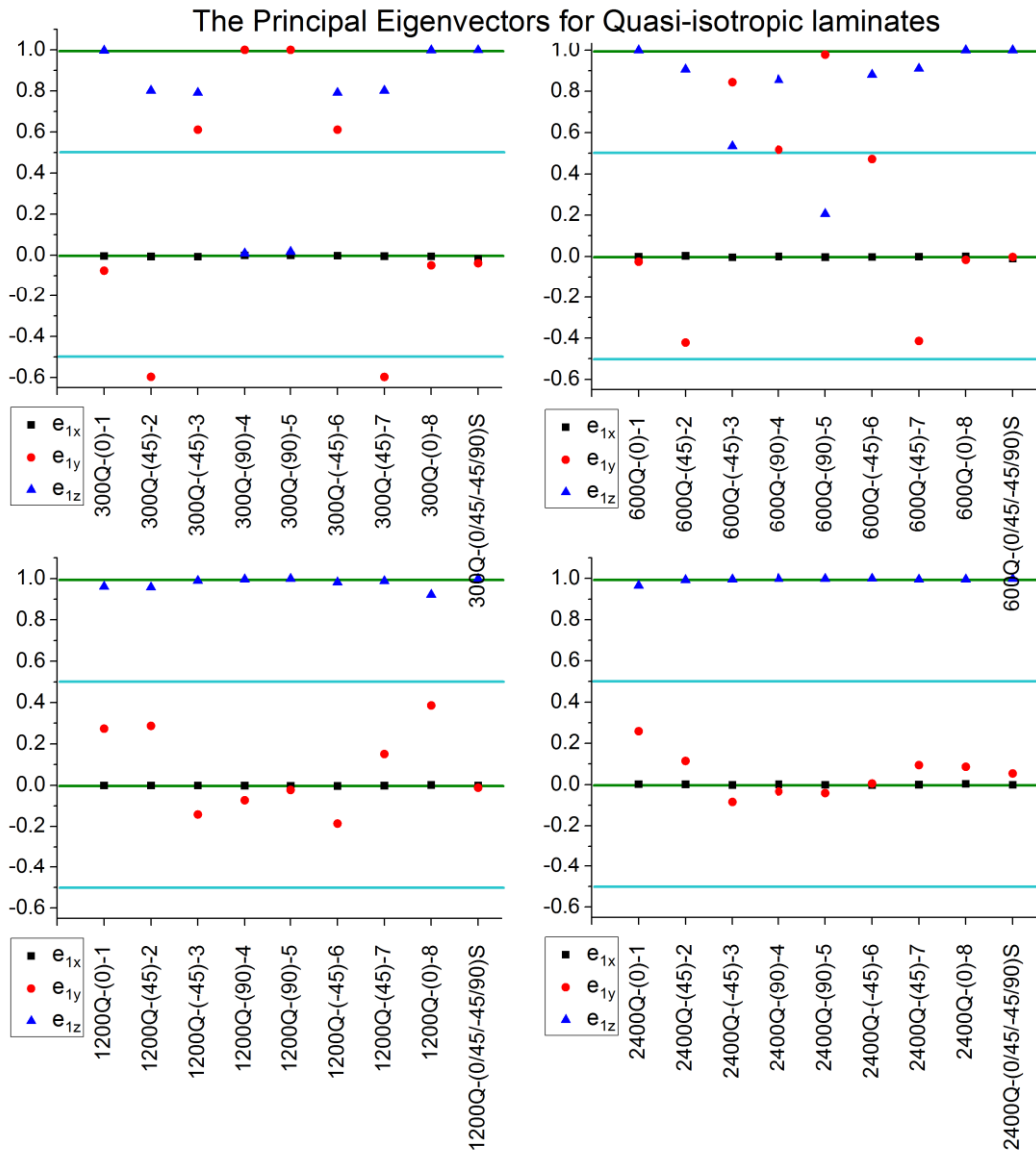
Figure 2.52 Principal eigenvector of quasi-isotropic laminates and lay-ups.
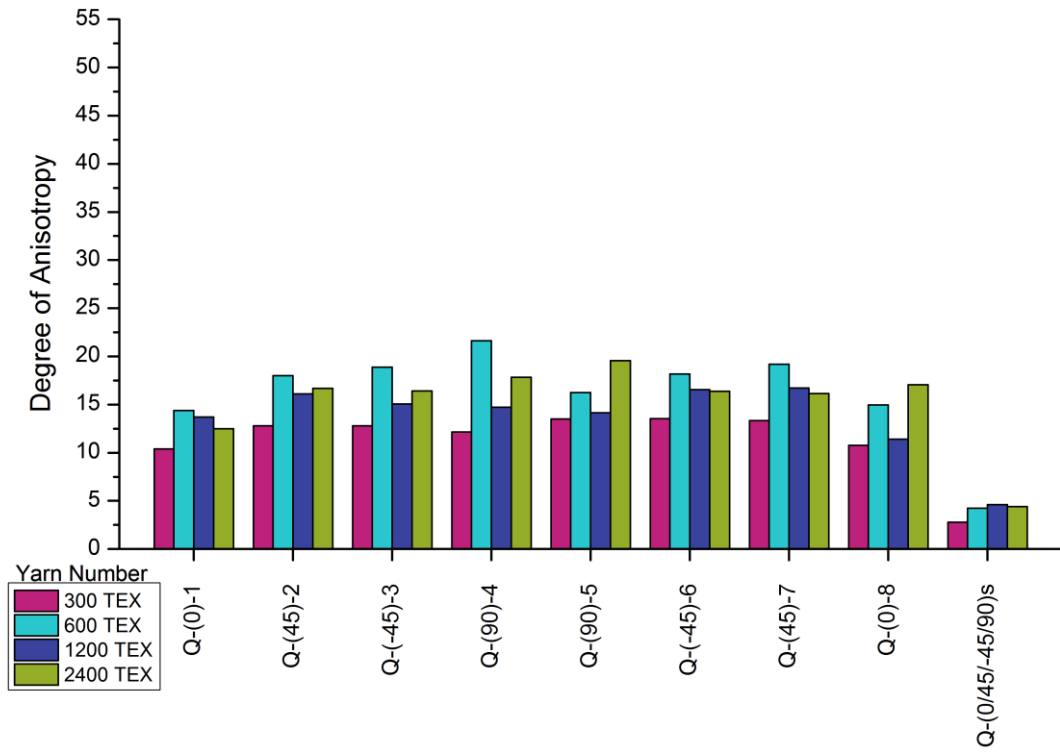
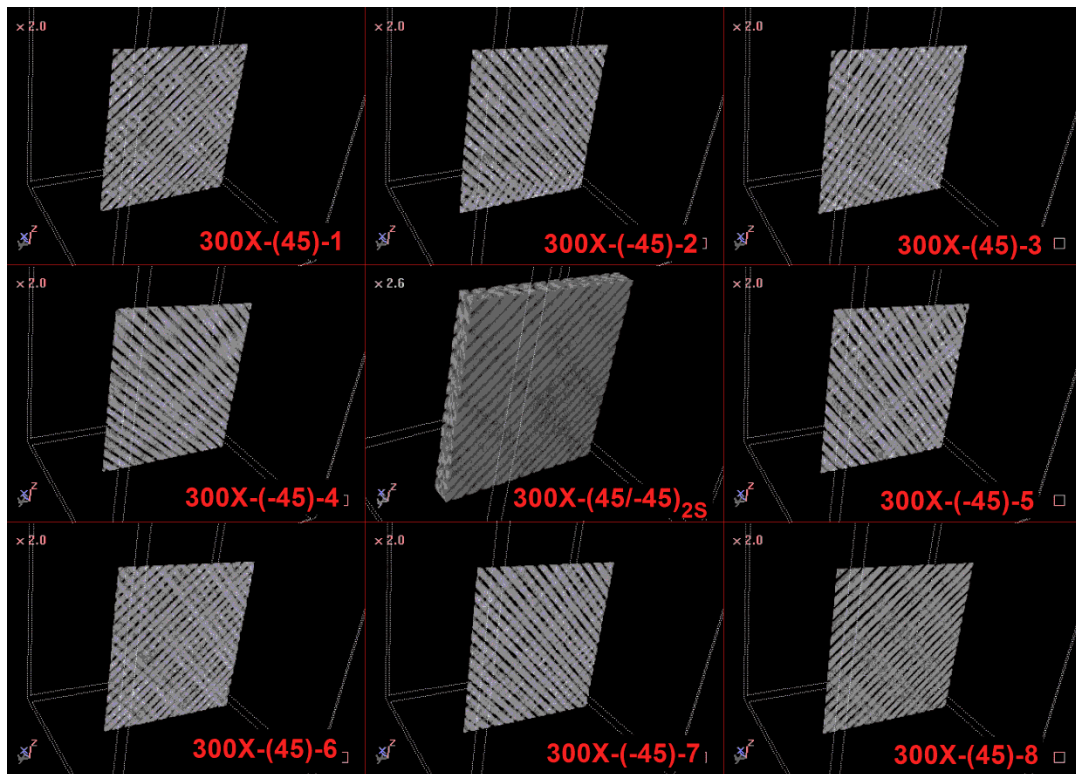Figure 2.53 Calculated degree of anisotropy of quasi-isotropic laminates and lay-ups.
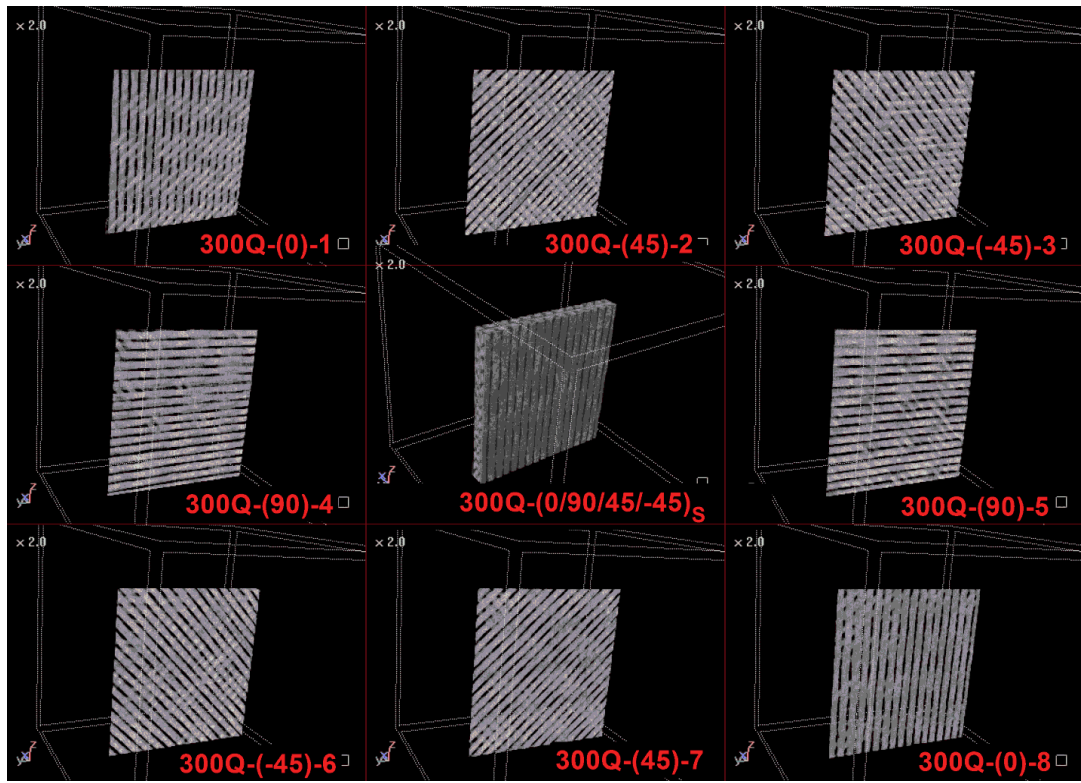
Figure 2.54 Reconstructed 3D images of quasi-isotropic 300 TEX specimen labeled as plies and laminate.
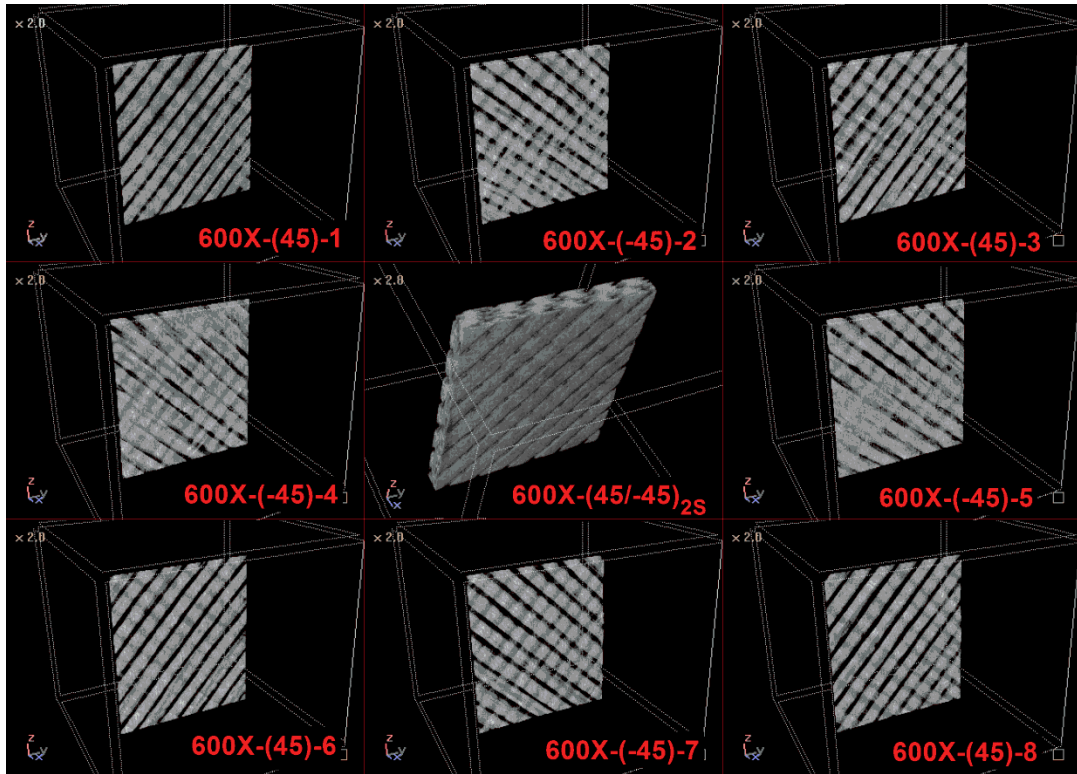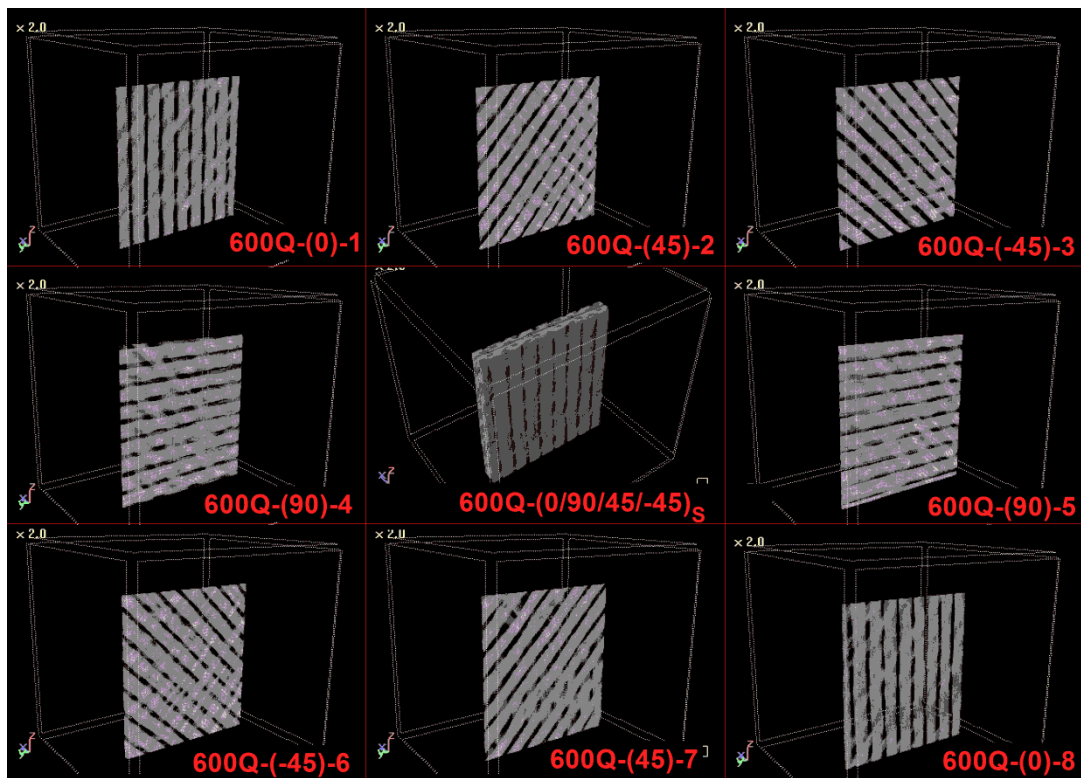

Figure 2.55 Reconstructed 3D images of quasi-isotropic 600 TEX specimen labeled as plies and laminate.
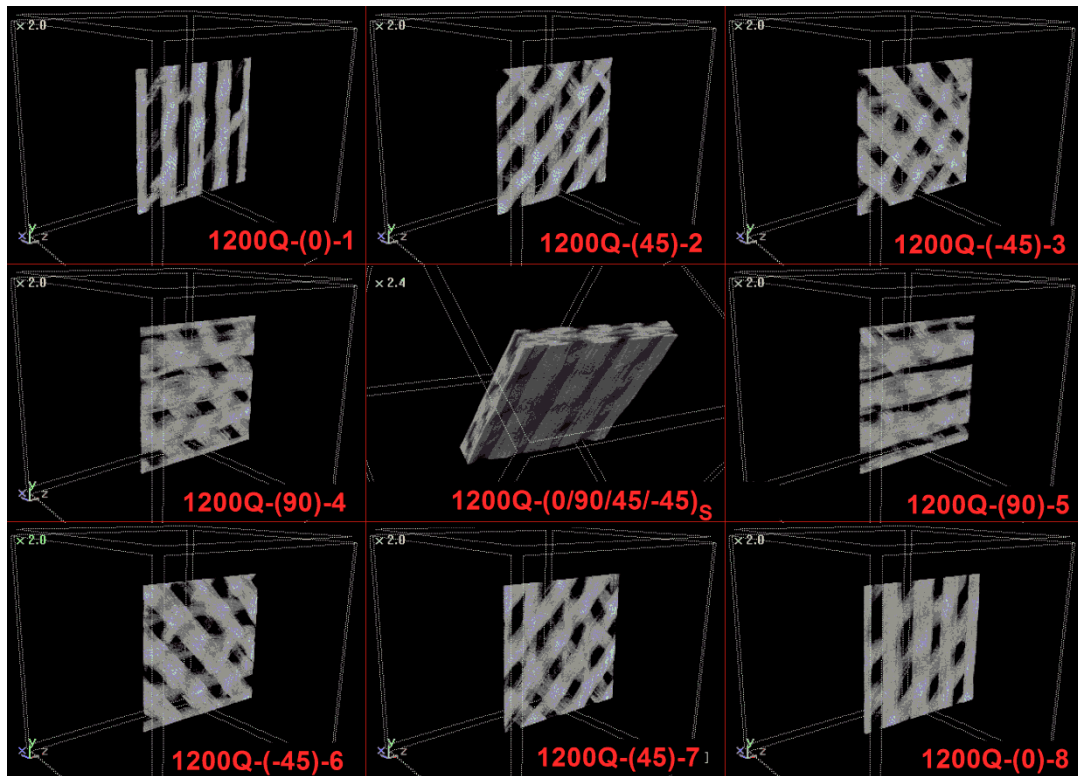
Figure 2.56 Reconstructed 3D images of quasi-isotropic 1200 TEX specimen labeled as plies and laminate.
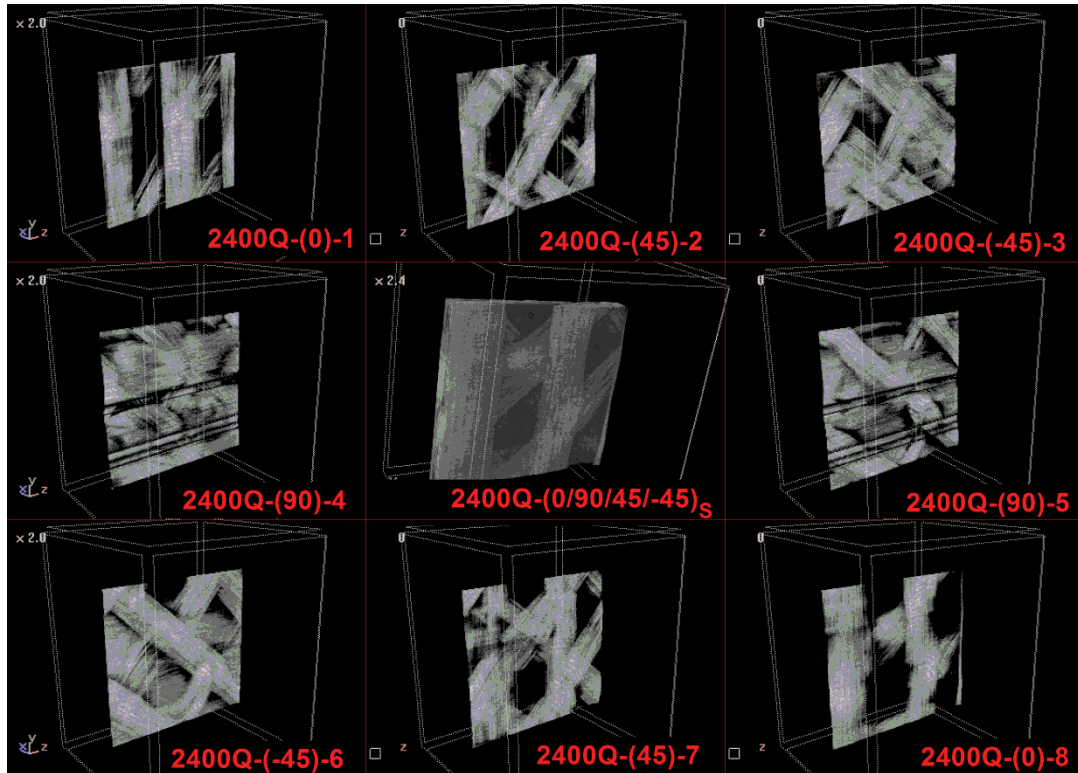
Figure 2.57 Reconstructed 3D images of quasi-isotropic 2400 TEX specimen labeled as plies and laminate.

2.4   Conclusion

This case study focused on the quantification of anomalies of the undamaged non-crimp glass fiber-reinforced composites in the micro and mesoscale via micro-computed tomography. Also the effect of the mesostructure on pre-damage composites containing five different lay-up sequences $[(0)_8, (90)_8, (0/90)_{2S}, (+45/-45)_{2S}$ and $(0/+45/-45/90)_S]$ was analyzed. A comparative analysis of the anomalies with the mechanical strength values and fracture modes under tensile loading were analyzed and possible correlation were reported.

Four different NCF fabrics of different yarn numbers were custom made and tested to observe the yarn effect on tensile behavior. More specifically, in this case study unharmed pre-damage characterization analyses have been conducted by μCT to interpret and understand the mechanical behavior of NCF glass fiber reinforced vinyl ester composites subject to tension. The effect of anomalies such as void content, cavity number and fiber/bundle undulations were characterized with imaging techniques and studied for five different stacking sequences. The unidirectional composite analysis shows that the meso architecture with respect to the choice of yarn number has an overall effect on the strength of the laminate. The placement/self-arrangement of the yarns inside laminate for each ply adjacent to other plies plays a major role in the mechanical behavior of corresponding laminate. Overlapping and the inter-bundle distances through laminae stacking determine the failure and fracture modes of laminate for unidirectional composites. Additionally, the visual inspection obtained for $(90)_8$ laminate is also correlated with the mechanical strength results where there is no clear difference for the samples of different yarn number since the load transfer mainly concentrates on the matrix part of the composite. The investigation of cross-ply composite laminates on the image analysis and mechanical behavior showed quite intriguing characteristics to explain the recorded mechanical behavior. Specifically, the placement of the yarns inside composite and various bundle/inter-bundle sizes have effects on the strength of the laminate. The importance of the symmetry within the lay-ups of the composite was also clearly observed in the image analysis results. Next,

71

(+45/-45)$_{2S}$ specimens under tension were analyzed, and scissoring effect on the in-plane shear performance of the composites was correlated with μCT based NDT. Finally, to understand the interactions of the effects of per basic lay-up cases in one example, quasi-isotropic laminates were studied. The results suggested that the shear performance of the laminates is the predominant factor during fracture of quasi-isotropic laminates.

In conclusion, the results suggest that there should be an optimum inter-bundle and bundle distance as the meso-architecture of the bundles plays a significant role on the tensile behavior of the composite specimens. Also, mechanical performance and fracture modes under tension were shown to correlated with the μCT analysis. Furthermore, the 3D image analysis shows that the amount of anomalies, the inter-bundle size, and bundle width of the NCF yarns affect the mechanical behavior of the composite laminates but more detailed analysis and data is necessary to quantify this relationship in a possible integrated formula.

3 TRACING ACOUSTIC SIGNATURES OF MECHANICAL BEHAVIOR OF COMPOSITES MATERIALS

3.1 Introduction

Transverse matrix cracking can be considered as an initially minor-to-intermediate level failure mode where crack formations occur in relatively weak matrix phase [97]–[100]. Depending on the lamination sequence and loading conditions, the formation of the transverse cracks may lead to ply-by-ply failure, induce delamination [101]–[103] and eventually facilitate the progression to ultimate failure by loss of the effective load transfer between and within the plies [104]–[106]. Hence, real-time detection and posterior study of the formation and growth of these cracks during mechanical testing are of crucial importance to understand and better identify the progressive nature of the fiber reinforced composite materials failure [107]–[110]. Acoustic emission (AE) methodology should be noted as one of the established methods for real-time damage monitoring in loaded composite materials [37], [50]–[53]. This approach typically requires expensive instrumentation, detailed and profound data analysis along with expertise/specialization which may not be standard and readily available for all composite practitioners with testing interests and needs.

An approach that is simple, affordable, easy to incorporate, yet capable of collecting useful information was exercised for this brief technical report named as *Sound-tracking of Failure events in cross-ply composite laminates under tension, K.Bilge, B.Yilmaz, M.Papila, 2016* [111]. This report has been submitted as a collaborative study to demonstrate the newly introduced methodology. The primary focus of the chapter remains in in-situ monitoring of unique sound profiles of laminated composites for the unity of thesis. The data provided and discussed in the scientific

report is not separated from the chapter. Hence, the correlation between in-situ tracking methodologies and fracture mechanics of the cross-ply laminates under tension is demonstrated.

The set-up makes use of a general-purpose noise reducing microphone. It can be attached to the specimens to capture the sound/acoustic signatures associated with the failure events and transmit the signal to a mobile recording device and computer.

Particular attention was given to the family of cross-ply $(0_m/90_n)_S$ laminates where $90°$ ply blocks that are susceptible to transverse cracking under tension [104], [105], [112]. Laminates of $(0/90_5)_S$, $(0_3/90_3)_S$, $(0_5/90)_S$ stacking sequence were tested to capture the effect of different ply-to-ply load distributions changing with the repeats/blocks of $0°$ and $90°$ plies. A lay-up of dispersed ply orientations forming homogenized $(0/90)_{3S}$ laminate was also tested to demonstrate a straightforward example of the matrix crack suppression under tension. Lastly, rather unconventional/non-practical laminates of $(90/0)_{3S}$ and $(90_3/0_3)_S$ layup sequences were studied to enhance the discussion on the differences between the progressive failure on specimens of similar in-plane stiffness. Specific failure events in the damaging regimes were also observed and recorded synchronously by video capturing capable optical microscope.

3.2   Methodology

3.2.1   Specimen Manufacturing

Experimentation strategy herein implemented a test matrix using several $(0_m/90_n)_S$ laminates with m+n=6 and a relatively homogenized laminate of $(0/90)_{3S}$. Overall, four different lay-ups were studied to expedite the transverse cracking in composite laminates [104] each assuming various levels of matrix crack suppression as the $90°$-ply-block thickness (n) varies. All of the composite laminates were manufactured out of unidirectional carbon fiber/epoxy prepreg provided by CMP Composites (CM-Preg–T-C- 150/ CP002-3). Two more choices of lay-ups were also

included, $(90/0)_{3S}$ and $(90_3/0_3)_S$, in order to create free surfaced matrix-cracking prone plies in the specimens.

Stacked plies of composites were vacuum bagged and hot pressed under 135^0C for 2 hours. Reported fiber volume fraction for prepreg plies were around 62%. Composite plates were cut into tensile test specimens per ASTM D3039 by a Diatrim diamond coated disc saw. The tensile tests were carried out using Zwick Roell Z100 Universal Testing Machine with a constant crosshead displacement rate of 1 mm/min.

3.2.2   Sound Amplitude-Based Analyses

The audio data were recorded by a noise-reducing RODE microphone which was attached to the middle of test specimen as barely touching without intruding/restraining the test procedure/sample (Figure 3.1). The analog audio data have been digitized with constant sample rate/frequency of f_s= 44100 Hz, which is almost standard for most general-purpose microphones. This sample frequency allows us to collect the digital sound data with the upper bound of 22050 Hz ($f_s > 2f_{max}$) according to sampling theory [113]. Since the limit of human hearing is between 20 Hz to 20 kHz, maximum frequency of the collected sound data is the limit of the human hearing. Although this broad range of sampling rate gives many advantages to AE data for events occurring at high frequencies, acquired sound data from AE is hard to analyze with simple methods in an efficient time manner. Even though some adaptive techniques in AE can understand the event occurrence and increase the sampling rate before the event to overcome big-data problems [114], the growing complexity of the data makes the sound data analysis complicated. The simplicity and easy access is the key advantage of the proposed methodology.
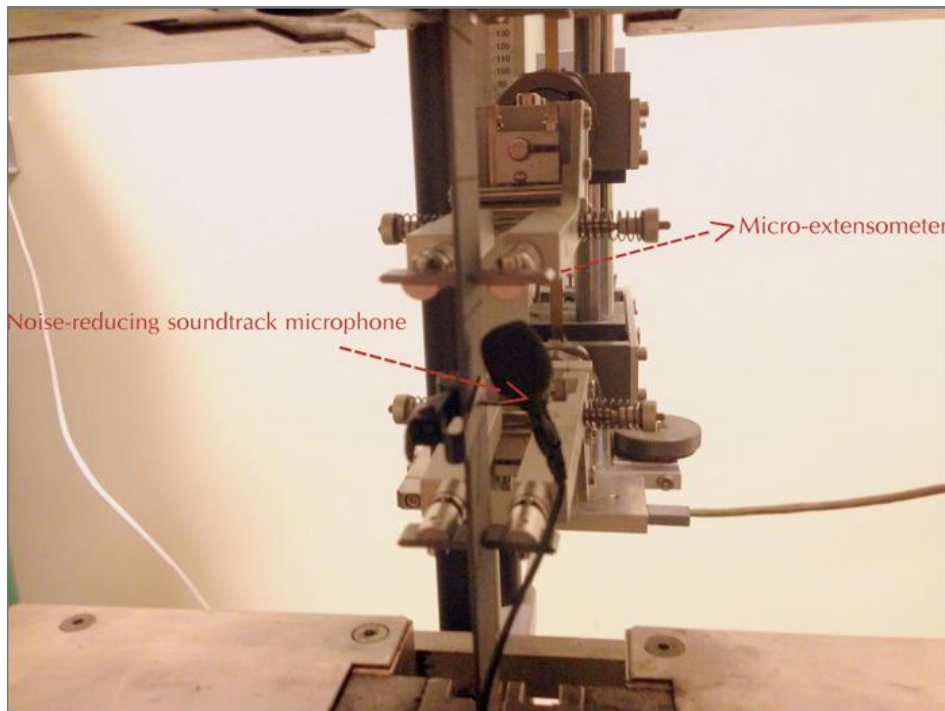
Figure 3.1 Experimental set-up with noise reducing microphone.

Acquired sound or audio data were then post-processed by using an open source software, Sonic Visualiser developed by Queen Mary University [115]. The normalized discrete audio peaks of the failure events reported in this work were reclaimed with Sonic Visualiser built-in acoustic analysis as the following.

For video capturing in the tensile tests, one edge of the specimens carefully polished and the optical video microscope was located in-focus to the middle of the sample. Sound and video recording were started in sync with the tensile loading to retrieve the exact times of cracking events and associate the stress-strain response to the acoustic and visual data. The experimental procedure and audio signal discretization technique of Sonic Visualiser software are summarized in Figure 3.2.
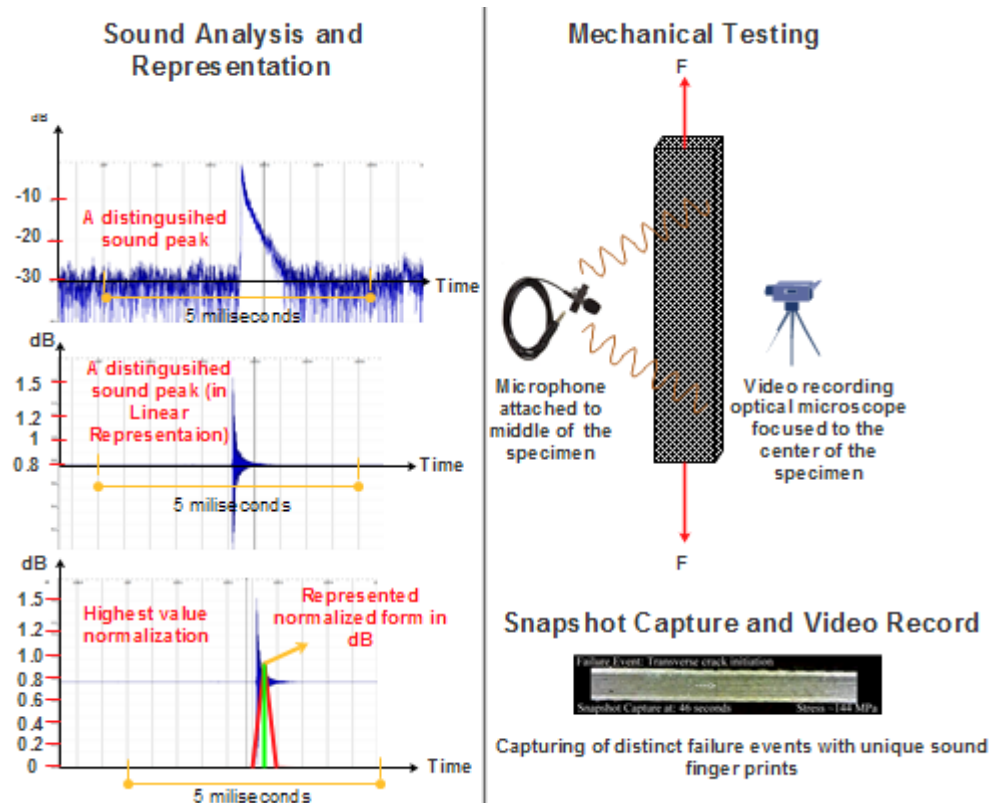
Figure 3.2 Schematic representations of sound-wave analysis and acoustic testing with in-situ microscope imaging.

The progressive failure observed in cross-ply laminates can be grouped into four categories by their specific acoustic signatures and crack characteristics as follows:

Minor Failure Events (Green Circles in Figure 3.4, Figure 3.5, Figure 3.6, and Figure 3.7): The failure of cross-ply laminates is typically initiated by the transverse cracks in 90^0 plies due to lower strength and brittle nature of thermoset resins under tension [112]. These matrix dominated events are typically mode-I cracks [112] and herein called the minor failure events considering their primary and not dominating influences (presented as green circles in Figure 3.4, Figure 3.5, Figure 3.6, and Figure 3.7). They do not cause noticeable drops in standard load-deflection curves (or stress-strain data). From acoustics point of view, however, these cracks generate frequent and low amplitude sound waves that can also be perceived by the human ear. Depending on the laminate stacking sequence, the initiation stress of these cracks and the generated sound amplitude differs.

Intermediate Failure Events (Yellow Squares in Figure 3.4, Figure 3.5, Figure 3.6, and Figure 3.7): With increasing load, the density of the transverse matrix cracks increases along the loading axis as such potential sites for other failure modes are

developed. For instance, another failure regime that can be considered as intermediate failure event typically includes the initiation of local interfacial debonding in 0/90 ply interfaces and narrow 0^0 ply strip splits due to ply interface discontinuities caused by the intensified transverse cracks. As for minor failure events, the intermediate or transitional events were not necessarily revealed by distinct load drops in the typical stress/strain profile. However, they typically generate a sharp and high pitched sound wave produced by specimen energy release, hence with higher wave amplitude as they emerged from the surface (presented as yellow squares in Figure 3.4, Figure 3.5, Figure 3.6, and Figure 3.7).

Major Failure Events (Orange Triangles in Figure 3.4, Figure 3.5, Figure 3.6, and Figure 3.7): Presence of the minor and intermediate failure spots in a laminate translates further into major failure events (presented as orange triangles in Figure 3.4, Figure 3.5, Figure 3.6, and Figure 3.7). They are mostly identifiable also as load drops on the stress/strain profile. The major failure events are typically associated with the 0^0 plies that comprise severe ply splitting along the length of the specimen and extensive delamination at the $0^0/90^0$ ply interfaces which are characteristically mode II cracks [116]. They also generate high amplitude sound waves which are easily collectible/recordable using the general purpose microphone.

Ultimate Fracture (Red Equilateral-quadrangles in Figure 3.4, Figure 3.5, Figure 3.6, and Figure 3.7): Finally, sudden and catastrophic failure occurs in conjunction with all the failure mentioned above modes and is marked by a broader and low pitched sound wave corresponding to simultaneously occurring of several failure events [51].

Note that the sound peaks corresponding to the failure events are already identifiable as unprocessed sound wave output. However, the sound discretization by highest value transformation reported in Figure 3.1 was performed for a better and simple representation in accordance with the stress-strain data.

3.2.3 Sound Frequency-Based Analysis

In previous studies, one-dimensional signal processing methods were applied on AE sound data to identify specific failure modes of the composites with different ply

orientation and lay-ups [2], [36], [51], [114], [117], [118]. Although the most widely used method to characterize failure events of composites amplitude based classification [2], [102], [119], another common method is the identification of frequency analysis. The frequency range for failure mode variations by AE have been allocated in literature with comprehensive experiment series on different lay-up settings and various mechanical tests [51], [114], [117]. In general, matrix cracking has been reported in the low-frequency range and fiber breakage in high frequencies. Classifications of the well-known studies have been reported in the following figure (Figure 3.3).
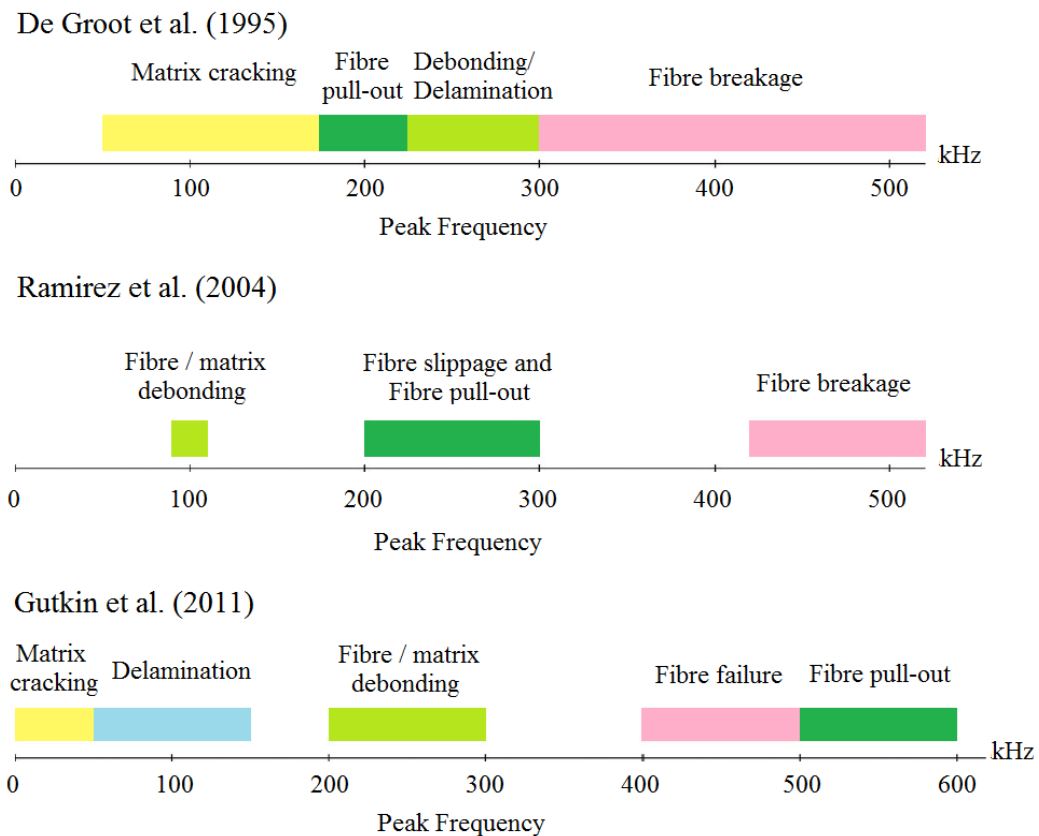
Figure 3.3 Failure mode classifications from previous studies according to peak frequency data obtained by acoustic emission.

3.3 Results and Discussion

3.3.1 Failure of $(0_m/90_n)_S$ Laminates with m=1 n=5 Under Tension

Figure 3.4 reports the applied stress, audio data and several snapshots of the video captured failure events, all acquired in sync during uniaxial tensile testing of $(0/90_5)_S$ laminates. Note that the corresponding visual recording is provided as supplementary video 1. The first set of peaks in the sound data at early stages of the mechanical test suggest that initiation of minor events corresponds to stress around 75 MPa (40 seconds). The data showed the fact that laminate goes through a period of transverse matrix cracking. Smaller amplitude dominated this period, but frequent audio peaks which are attributed to several random transverse cracks occurring in the 90°ply blocks. Also, note that the initiation of these minor cracks was not marked off as load drops in the stress-time curve. Hence, they are arguably undetectable by the basic and typical mechanical stress-strain test data. However, simultaneous recording of acoustic signatures by the microphone effectively captured history/progress of the transverse cracking which continued till the ultimate fracture. In the course of mechanical loading higher amplitude sound peaks emerged beyond 250 MPa (110 seconds). Early such high pitched sound peaks are attributed to localized/narrow 0° ply-strip splitting initiated from the discontinuities due to transverse matrix cracks [112]. The ply-strip splitting events occurred rather randomly in the laminate and did not associate to any load drop mark in the stress-strain curves. The exact timing of these splitting failures was also identified by following the acoustic signatures (e.g. at 122nd and 127th seconds). As the test progresses, a notable load drop occurred in the stress/strain curve which signifies a major failure event in the laminate. This failure event is captured both within the sound data profile (as a high pitch high amplitude sound peak) and the captured video (please see supplementary information). At around 295 MPa (129 seconds); 0° ply-split completely along the specimen length and the load was redistributed within the plies. The specimen was able to sustain increased stress till the next major failure event. The failure progression appeared to continue until the load transfer between the plies was lost and intact 0° plies were loaded for fiber failures resulting in an overall explosive ultimate fracture.

80

Figure 3.4 Stress-strain curve and sound amplitude representation of $(0/90_5)_S$ laminate.

3.3.2 Failure of $(0_m/90_n)_S$ Laminates with m=3 n=3 Under Tension

Figure 3.5 reports the applied stress, audio data and representative snapshots of the captured failure events acquired synchronously during uniaxial tensile testing of $(0_3/90_3)_S$ laminates. Captured video of the tension test is provided in supplementary information labeled as video 2. As the proportion of 0° plies in this laminate was higher than the previous case, load share of matrix cracking prone 90° plies required greater than overall applied stress.
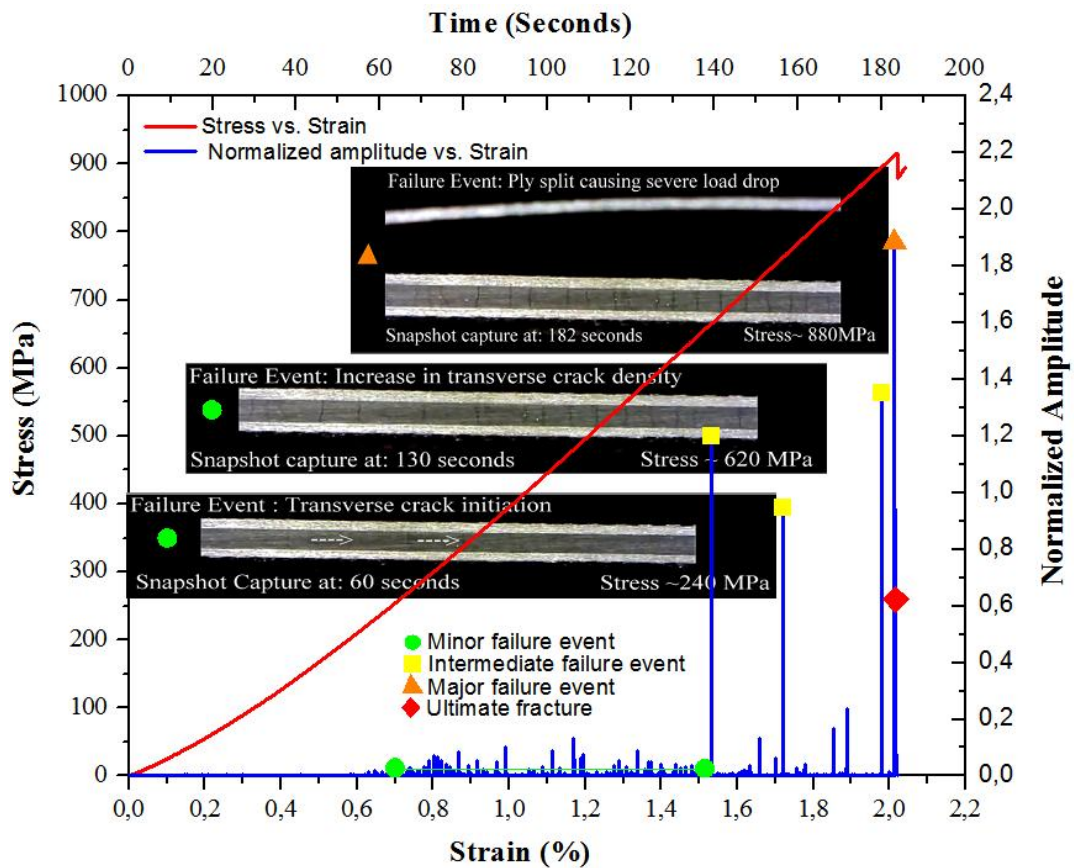
Figure 3.5 Stress-strain curve and sound amplitude representation of $(0_3/90_3)_S$ laminate.

Hence the transverse cracking was initiated at around 220MPa ($\sim 60^{th}$ seconds from the start) and continued to densify along the specimen until the ultimate fracture. The first intermediate failure event was observed at the overall stress of about 500 MPa ($\sim 140^{th}$ seconds). This event can be attributed to a local delamination or ply-split event, but the visual identification was not possible since the failure event occurred outside of the recording window of the focused microscope. Compared to the $(0/90_5)_S$ case, the accumulation of the intermediate failure events for this case was less. The intermediate regime continued with no standing out load drops in the stress-strain profile up until a major event was observed at 880MPa (~ 182 seconds). This major failure event associated with the splitting of a large $0°$ ply strip was adequately captured within the sound signal profile. The tested laminate was not able to redistribute the loading since the damage was severe and total fracture instantaneously occurred just after the major failure event.

3.3.3 Failure of $(0_m/90_n)_S$ Laminates with m=5 n=1 Under Tension

Figure 3.6 reports the audio data and several snapshots of the video captured failure events, all acquired in sync during uniaxial tensile testing of $(0_5/90)_S$ laminates. Visual recording of the tension test is provided in video 3. For this case, 90^0 ply blocks were two plies thick and centered at the laminate midplane. The failure sequence was initiated by transverse cracking at about 800MPa (~140 seconds). Since the matrix crack prone ply block thickness was smaller, sound peaks associated with the transverse cracks had relatively low amplitudes. However, it is still distinguishable within the audio data profile. The data also suggested that intermediate failure events corresponding to local delamination and ply splits were more frequent than the previous cases. A good example of a local delamination initiation from transverse cracks was captured at around 1320 MPa (~214 seconds) although it did not cause any load drops in the stress-strain profile. The observations suggest that the delamination occurs on the 0/90 ply interface which then propagates and translates into a major failure event. At around 1475 MPa (~227 seconds) 0° and 90° ply blocks have been fully separated from each other. Second major event around 1480 MPa (~234 seconds) was also noted when a severe delamination occurred in the 0° plies. These two failure events were clearly distinguishable both in the captured video (video 3) and the sound data profile. Upon redistribution of the stresses in the laminate, the specimen was still able to sustain loads. Following these events, several ply strip splits have occurred in 0° ply blocks, and the final fracture was explosive.
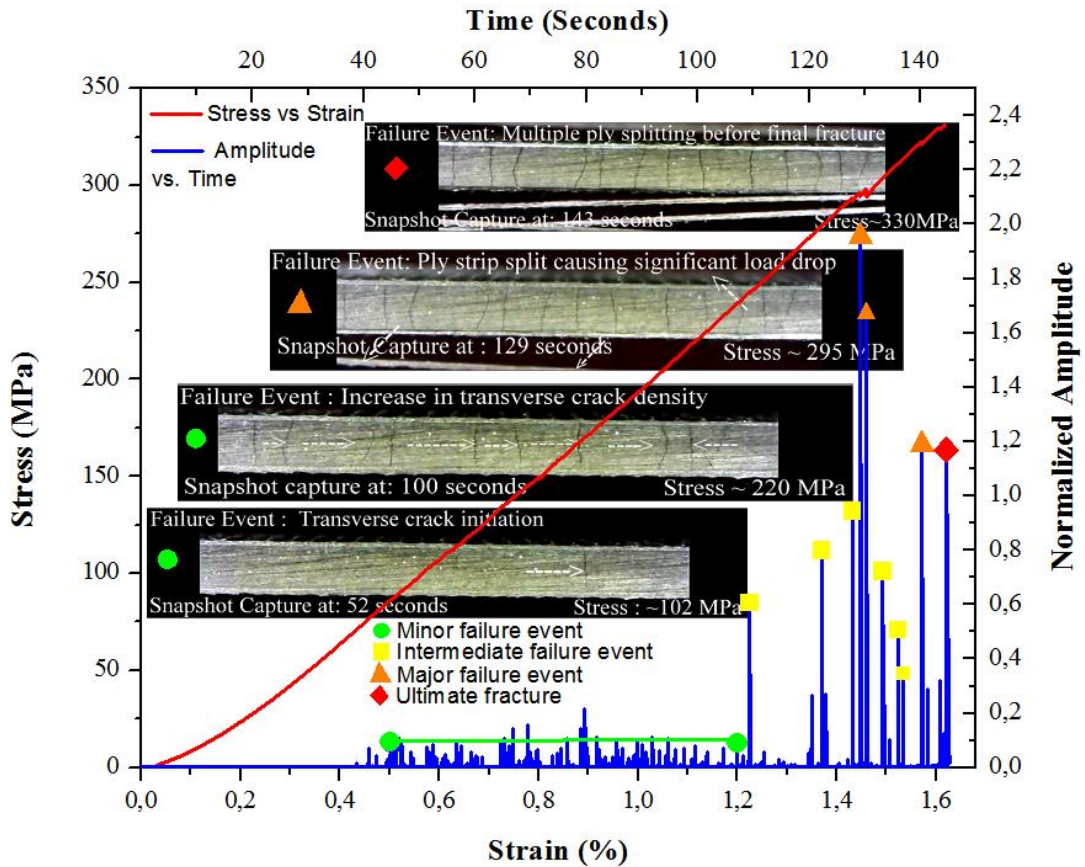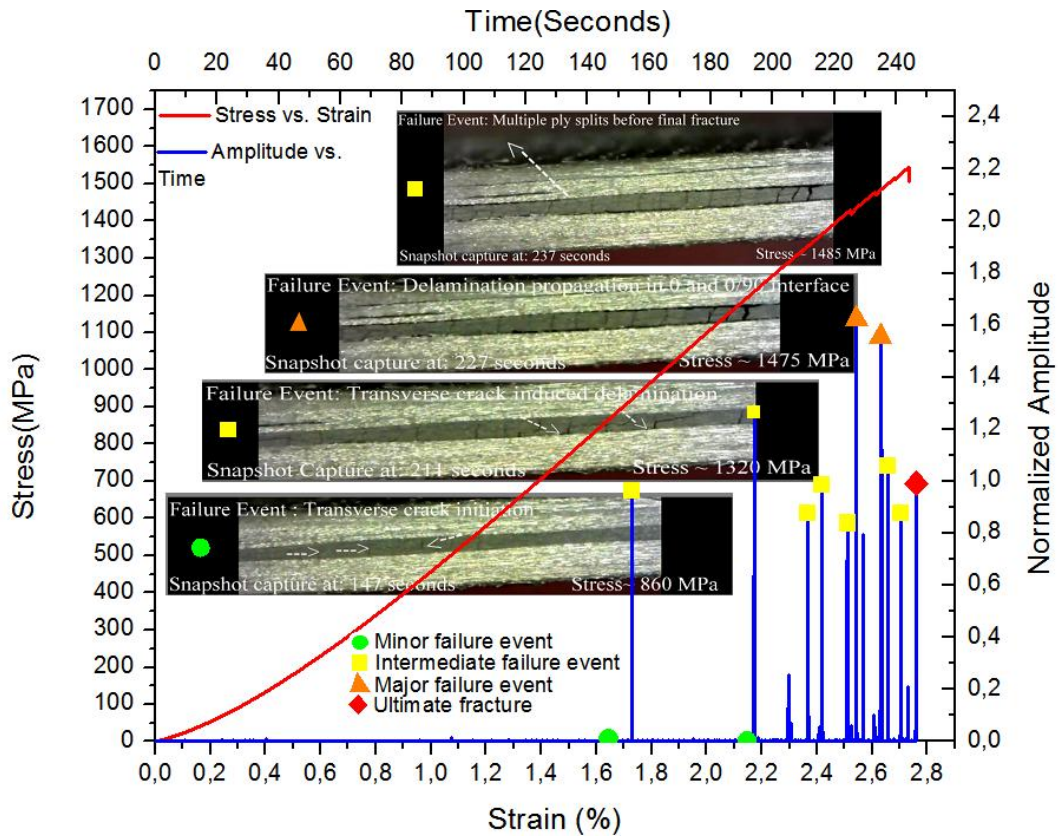
Figure 3.6 Stress-strain curve and sound amplitude representation of $(0_5/90)_S$ laminate.

3.3.4 Failure of $(0/90)_{mS}$ Laminates with m=3(=n) Under Tension

Figure 3.7 reports the applied stress along with synchronous audio data and selected snapshots of the captured failure events during uniaxial tensile testing of $(0/90)_{3S}$ laminates. The visual record of the test is presented in video 4 of the supplementary section. Note that 0°-90° plies were stacked subsequently so that the thick block of multiple 90° plies were avoided except at the mid-plane, a block of 2 plies due to symmetry. The lay-up of dispersed plies creates more homogenized load distribution in the laminate. The audio and video-assisted mechanical test results suggested the occurrence of the intermediate and major failure events due to transverse cracking were suppressed. The absence of the high amplitude peaks is clearly notable in the audio data profile. Instead, the transverse cracking that was initiated around 300 MPa (~85 seconds) continued and densified within the dispersed 90 plies until the final fracture. Note that two laminates of the same in-plane stiffness [$(0/90)_{3S}$ vs. $(0_3/90_3)_S$]

were remarkably different regarding the damage progression. From this perspective, a homogenized laminate of $(0/90)_{mS}$ can be considered as a demonstration case where damage suppression was uniquely identified by the simple audio signature capturing method exercised at this moment.
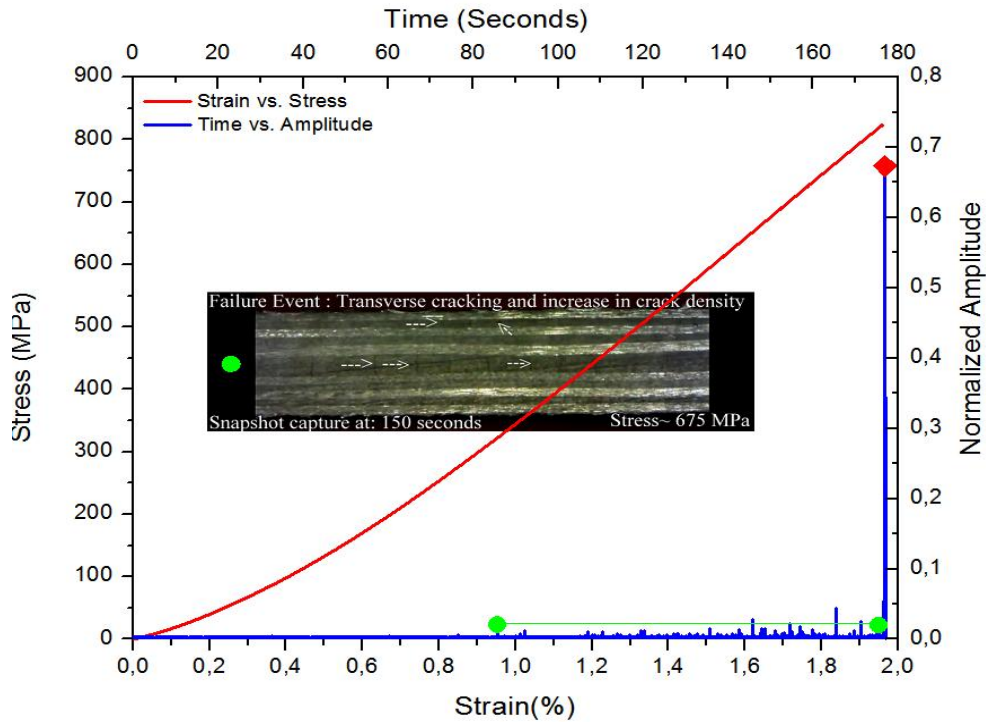
Figure 3.7 Stress-strain curve and sound amplitude representation of $(0/90)_{3S}$ laminate.

3.3.5 Failure of $(90_m/0_n)_S$ and $(90/0)_{mS}$ Laminates with m=3 n=3 Under Tension

Two more, rather unconventional test cases with $(90_3/0_3)_S$ and $(90/0)_{3S}$ lay-up sequences which also result in the same in-plane stiffness with the cases of section 3.4. They were notably included to investigated what happens if the matrix-cracked, failing plies were rather at the surfaces than being sandwiched between the 0^0 plies. As depicted in Figure 3.8 and video 5 of the supplementary section, the sound amplitudes acquired from $(90_3/0_3)_S$ specimens were rather high with respect to previous cases since the failure events associated with the 90° plies were also open to the free top and bottom surfaces of the specimens. First transverse cracking began at around 200 MPa (~60 seconds). Failure in the 90° plies continued and multiplied randomly throughout the

specimens until around 160 seconds where blocks of the 90º plies were gotten separated from each other. Delamination at the 0/90 interfaces was then observed. This failure event caused a significant load drop in the stress-strain profile. However, this particular event could not be identified with microphone based approach as it was successfully captured in previous cases where 90º plies were embedded between 0º plies. This is attributed to the fact that the sound output already spreading from the surface was intense and dominating. No fracture at the 0º plies occurred for this case.
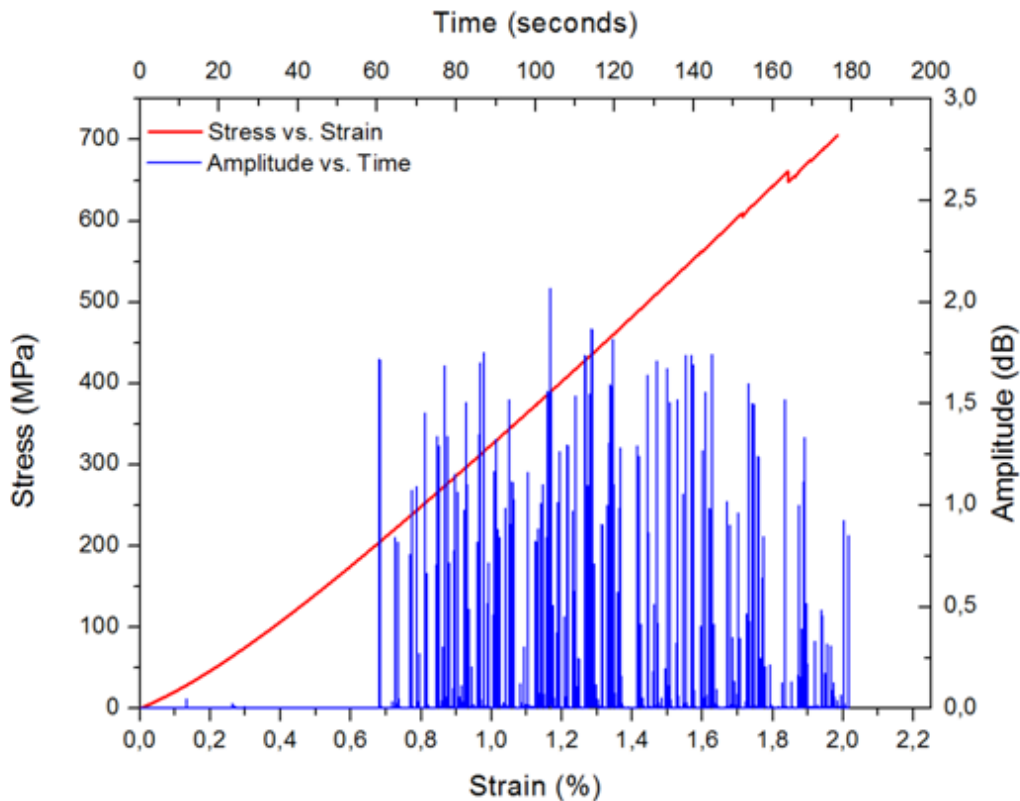
Figure 3.8 Stress-strain curve and sound amplitude representation of $(90_3/0_3)_S$ laminate.

On the other hand, the failure profile of the $(90/0)_{3S}$ specimens was quite similar to $(0/90)_{3S}$ where the failure was initiated by transverse cracking in 90º plies and finished with a sudden fracture at similar loads (Figure 3.9, video 6). The comparison of these two cases suggests the following about the proposed methodology: the amplitude based sound analysis is distance and lay-up sequence (hence the load distribution) sensitive. Large 90º ply blocks open to the specimen top and bottom free surfaces and the ones embedded inside generate different sound profiles. When the load distribution is more homogenized as in the case of $(0/90)_{3S}$ and $(90/0)_{3S}$ the discrete fracture events were prevented, and the sound output generated from the specimens are nearly identical.

This alone points out the advantage of the homogenized laminates of dispersed ply angles.
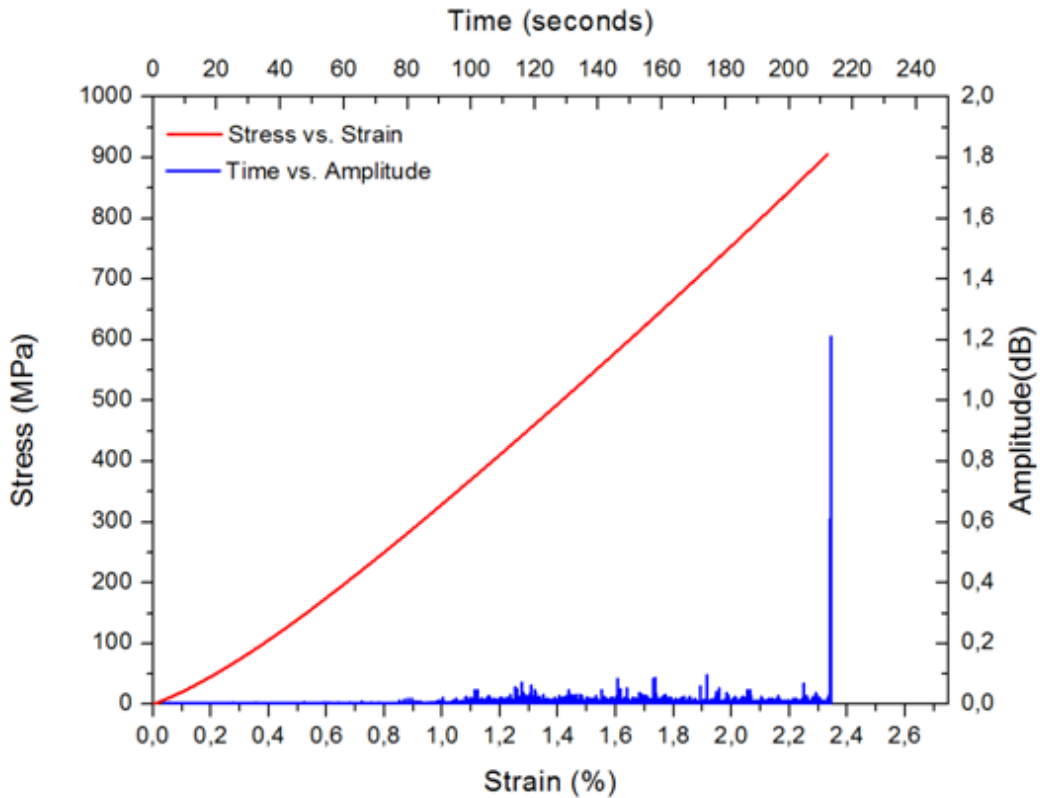
Figure 3.9 Stress-strain curve and sound amplitude representation of $(90/0)_{3S}$ laminate.

3.3.6   Frequency Response of Laminates

Before starting frequency analysis, it is important to understand how frequency is calculated on discrete time signals. The average frequency of one acoustic hit is defined as the peak count on discrete audio data divided by duration of the hit. Also, peak frequency is determined as the frequency value which has the highest amplitude of power spectrum inside that time period [120]. The reason behind the difference in maximum frequency obtained by acoustic emission and microphone can be explained by the duration differences in the discrete time domain. At the same time interval, standard acoustic emission collects almost 23 times more data than standard microphone according to sample frequency ratio (1 MHz/ 44.1 kHz = 22.68). While analyzing frequency for the same particular event, collected discrete data depends on

the sample rate of the signal collector property. The ratio between sample frequencies may generalize in the frequency domain, and categorization of the failure types may be determined according to previous studies of De Groot et al. [51], Ramirez et al. [114], and Gutkin et. al. [117] (Figure 3.3).

The failure mode characterizations in previous studies are modified through their sampling rate ratio (23 times) to the microphone used in this study. Following figures shows that there is a strong correlation between individual cases and some may not fit well with the data we have obtained from tensile testing of six different cross-ply laminates. Also, they will open discussions on the failure mode-frequency correlations in general, and that alone would hinder our primary motivation

Firstly, the oldest study of the three associations that are dicussed in this study ([51], [114], [117]) has been shown as color labels in Figure 3.11, Figure 3.12, Figure 3.13, Figure 3.14, Figure 3.15, and Figure 3.16 for six different stacking sequences. The classification of failure modes according to De Groot's study [51] is shown in Figure 3.10. Even though the pattern of frequency data seems to overlap with the frequency between 6000 Hz and 14000 Hz, the lower frequency ranges are not significantly separated with color classifications of [51].

Figure 3.10 Color coded failure modes according to De Groot et al.'s study [51].

Figure 3.11 Time vs. frequency graph for $(0/90_5)_S$, color labels are presented according to the classification of [51].

Figure 3.12 Time vs. frequency graph for $(0_3/90_3)_S$, color labels are presented according to the classification of [51].

Figure 3.13 Time vs. frequency graph for $(0_5/90)_S$, color labels are presented according to the classification of [51].

Figure 3.14 Time vs. frequency graph for $(0/90)_{3S}$, color labels are presented according to the classification of [51].

Figure 3.15 Time vs. frequency graph for $(90_3/0_3)_S$, color labels are presented according to the classification of [51].

Figure 3.16 Time vs. frequency graph for $(90/0)_{3S}$, color labels are presented according to the classification of [51].

The second correlation of the obtained frequency data has been classified according to [114] (Figure 3.17). The given frequency range has been downsized with the ratio of noise reduced microphone's sampling rate and acoustic emission sampling rate. The given results (Figure 3.18, Figure 3.19, Figure 3.20, Figure 3.21, Figure 3.22, and Figure 3.23) indicate that the relationship between the frequency data and Ramirez et al.'s classification [114] is not strongly correlated for the specimens with fewer 90° plies than the others. The reason behind this weak correlation can be explained by the difference in the type of fiber reinforcement for discussed study and current one.
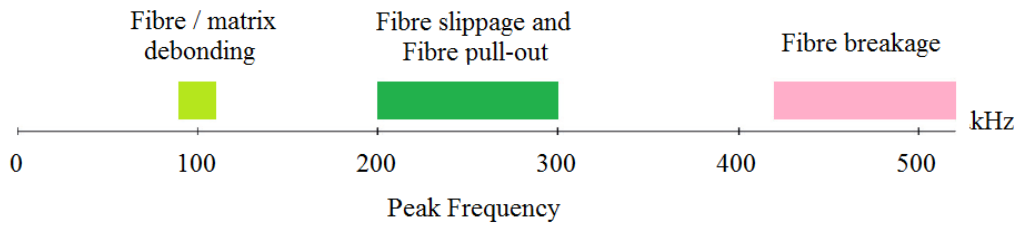
Figure 3.17 Color coded failure modes according to [114].

Figure 3.18 Time vs. frequency graph for $(0/90_5)_S$, color labels are presented according to the classification of [114].

Figure 3.19 Time vs. frequency graph for $(0_3/90_3)_S$, color labels are presented according to the classification of [114].

Figure 3.20 Time vs. frequency graph for $(0_5/90)_S$, color labels are presented according to the classification of [114].

Figure 3.21 Time vs. frequency graph for $(0/90)_{3S}$, color labels are presented according to the classification of [114].
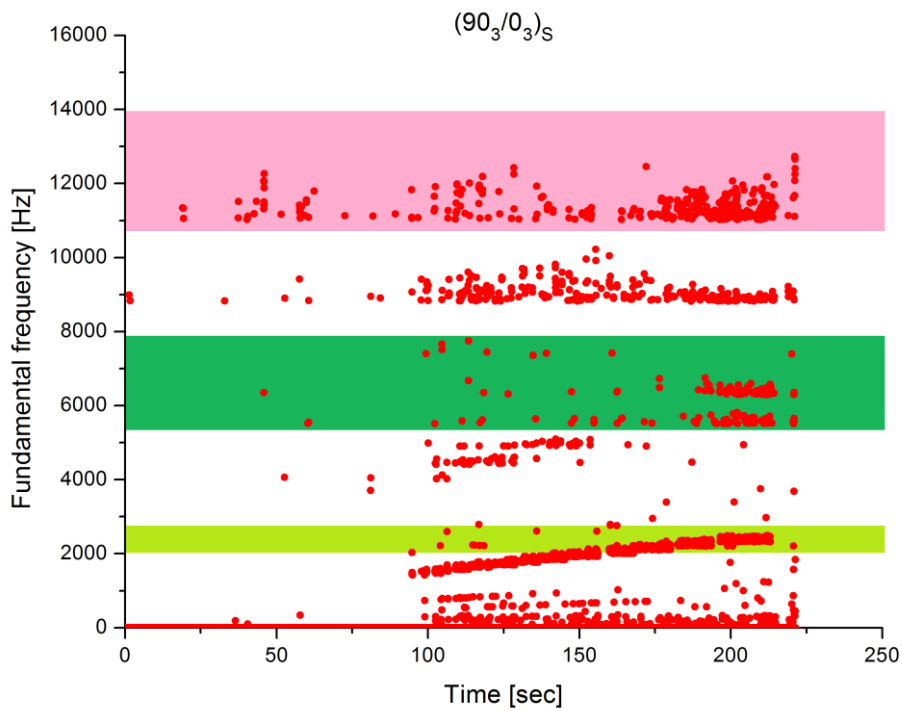
Figure 3.22 Time vs. frequency graph for $(90_3/0_3)_S$, color labels are presented according to the classification of [114].
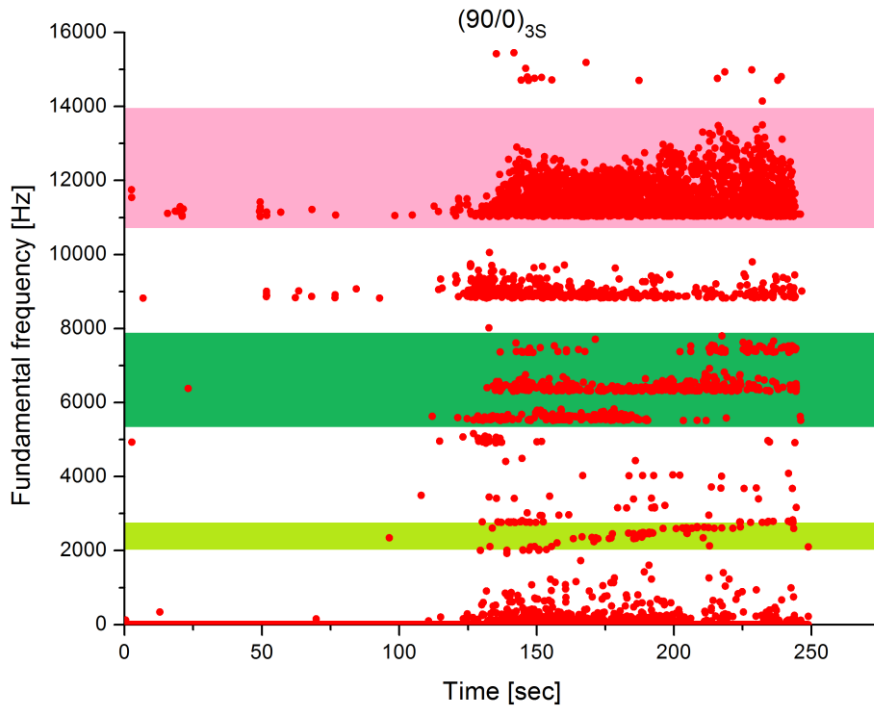
Figure 3.23 Time vs. frequency graph for (90/0)$_{3S}$, color labels are presented according to the classification of [114].

Last but not least, the correlation of the frequency data has been color coded according to Gutkin et al.'s study [117] (Figure 3.24). This classification shows highly correlated fracture events with the observed one (Figure 3.25, Figure 3.26, Figure 3.27, Figure 3.28, Figure 3.29, and Figure 3.30). Specifically, frequencies lower than 4000 Hz shows that the matrix cracking and delamination observed on the laminates have been correlated with the obtained sound signal data. The higher frequency range also shows a similar pattern with the proposed color labeled classification of [117]. even though there is an apparent shift on the graphs.
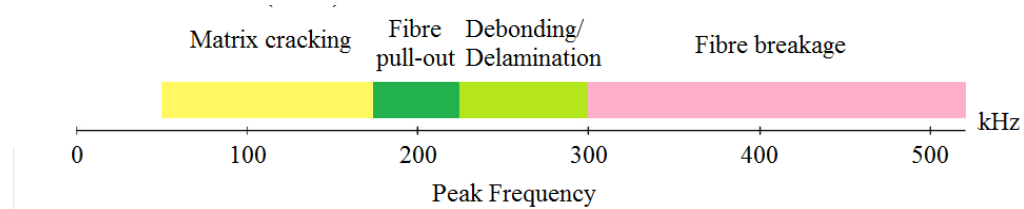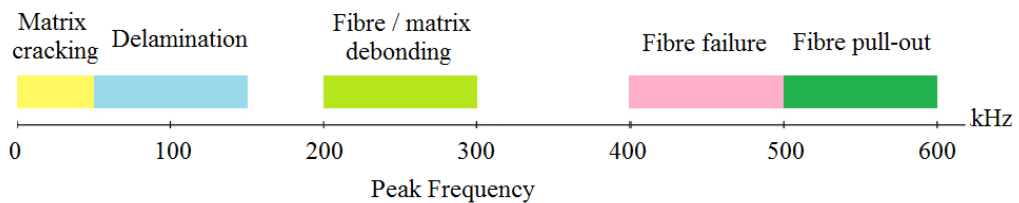

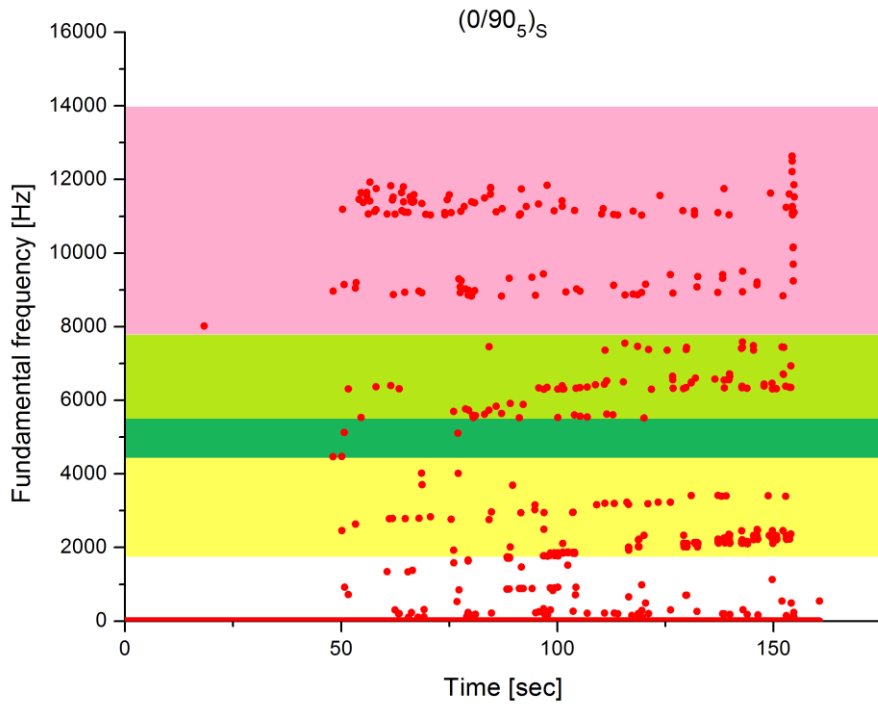Figure 3.24 Color coded failure modes according to [117].
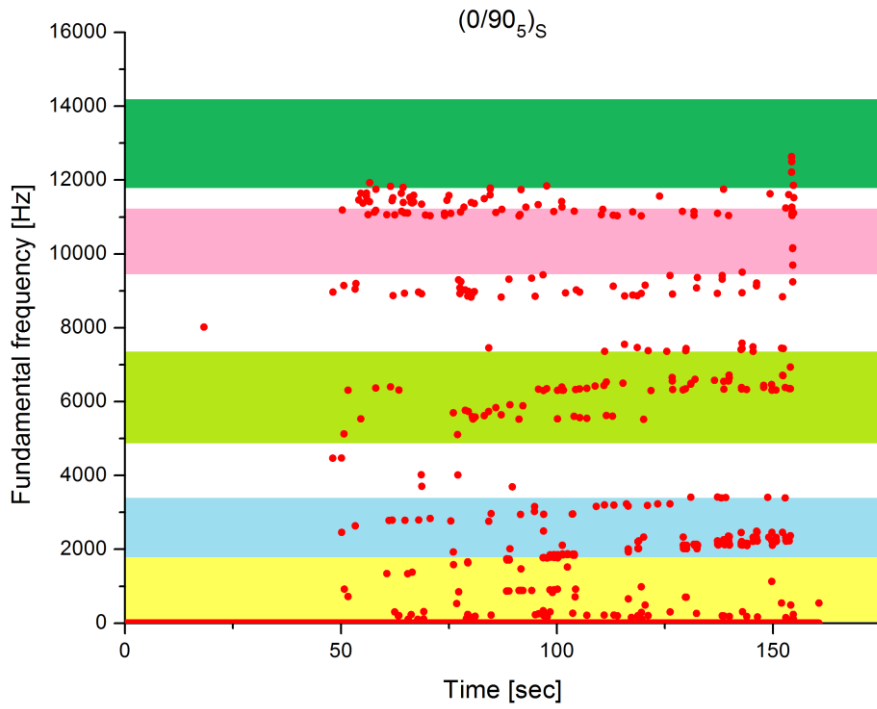
Figure 3.25 Time vs. frequency graph for $(0/90_5)_S$, color labels are presented according to the classification of [117].
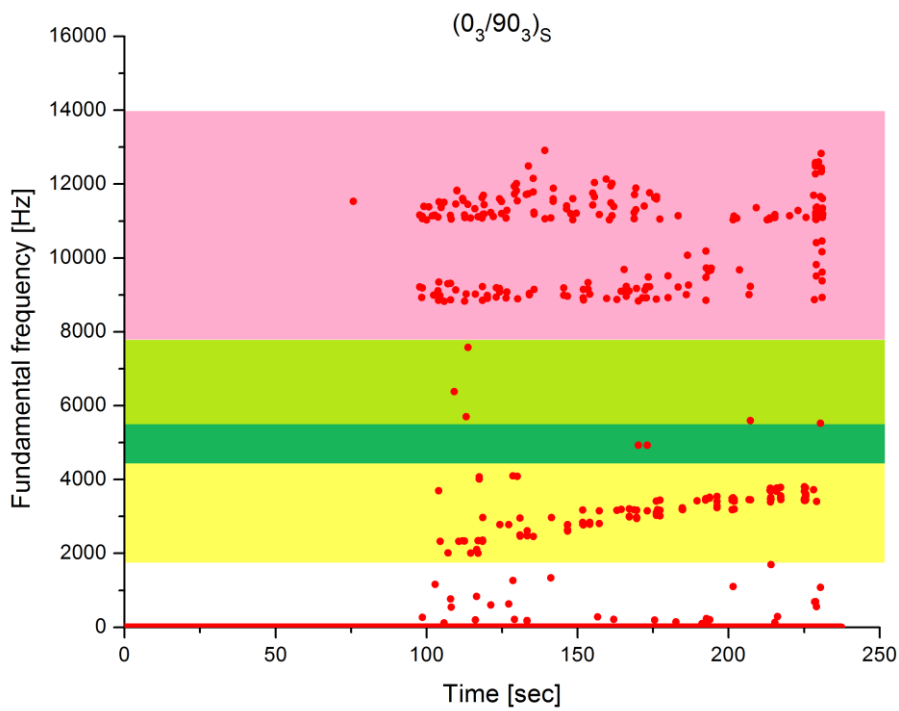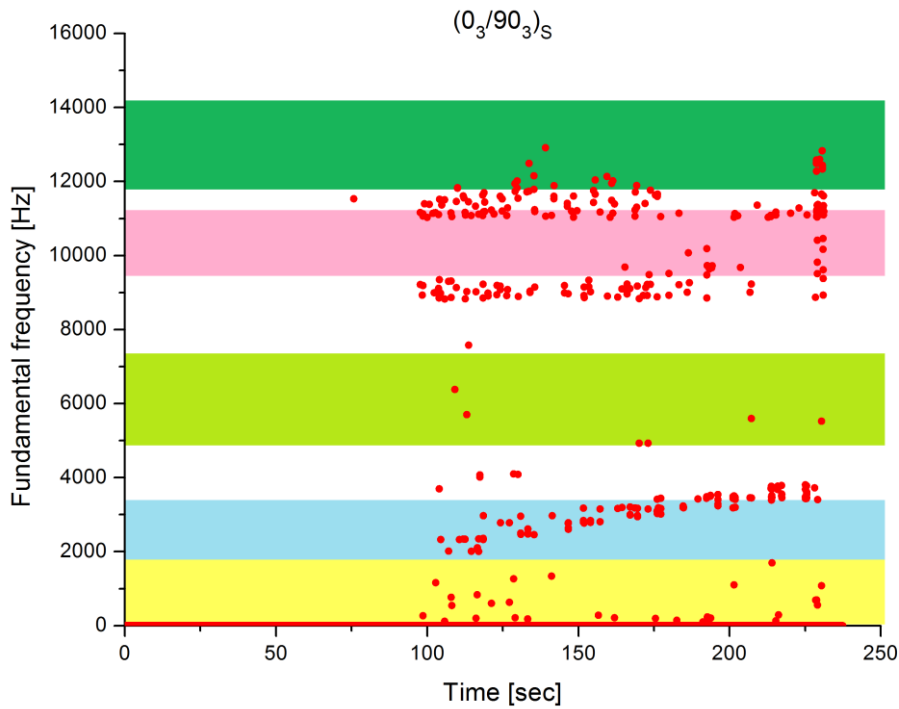

Figure 3.26 Time vs. frequency graph for $(0_3/90_3)_S$, color labels are presented according to the classification of [117].
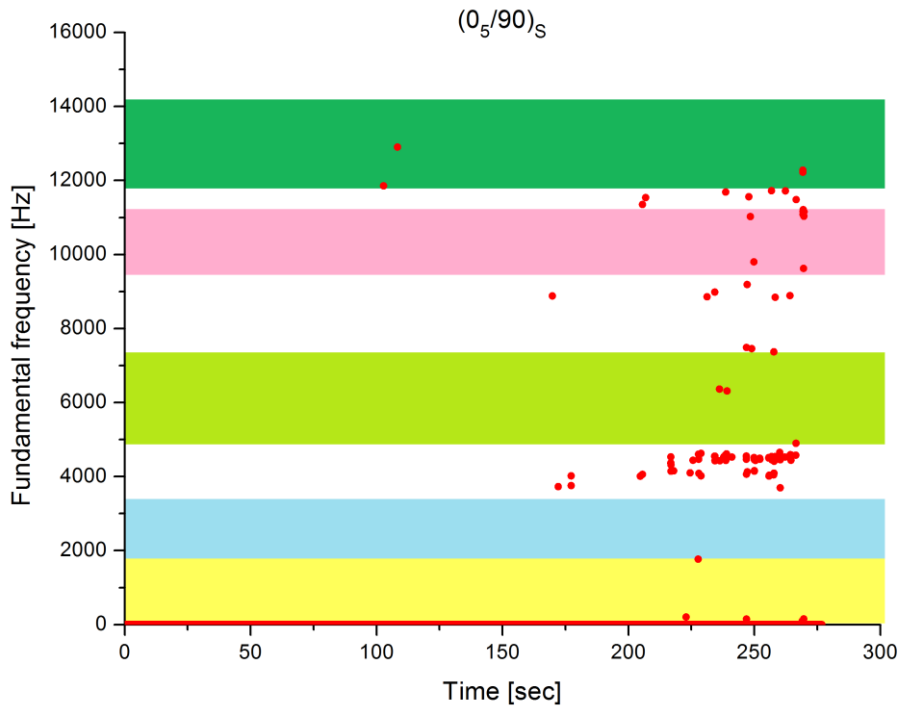
Figure 3.27 Time vs. frequency graph for $(0_5/90)_S$, color labels are presented according to the classification of [117].
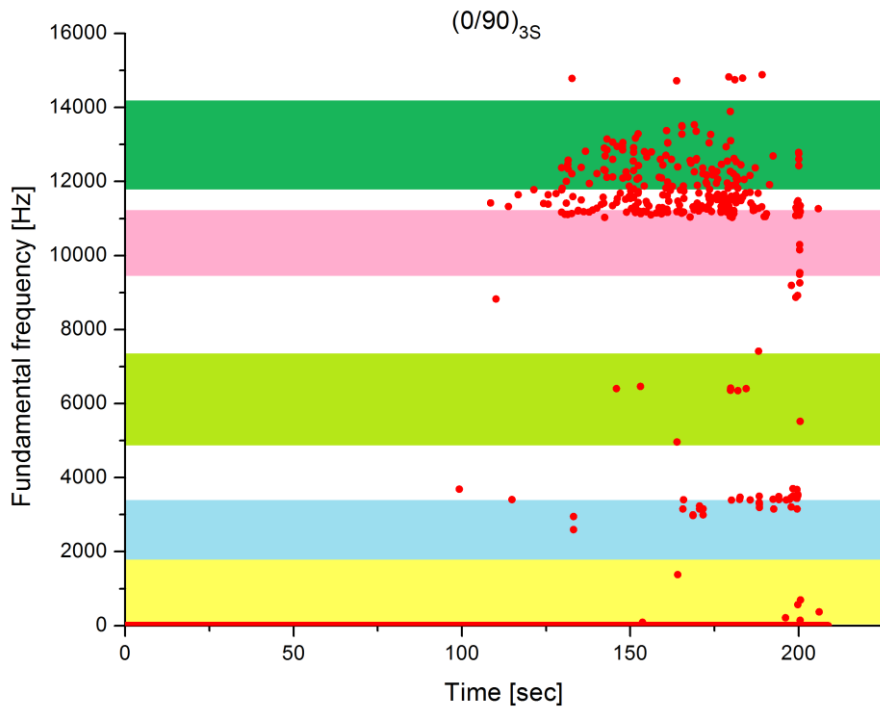
Figure 3.28 Time vs. frequency graph for $(0/90)_{3S}$, color labels are presented according to the classification of [117].
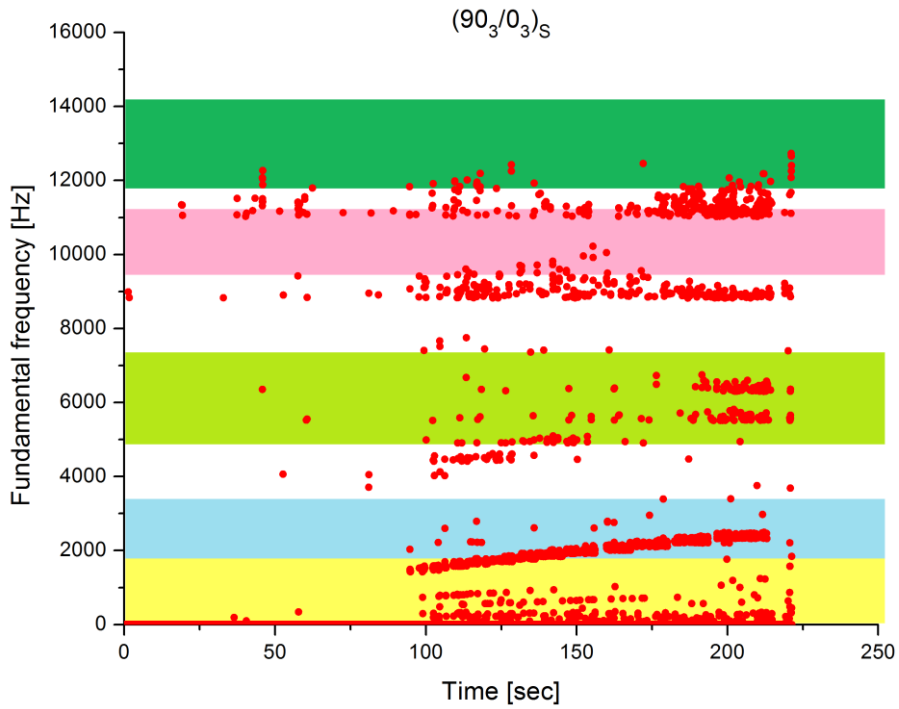
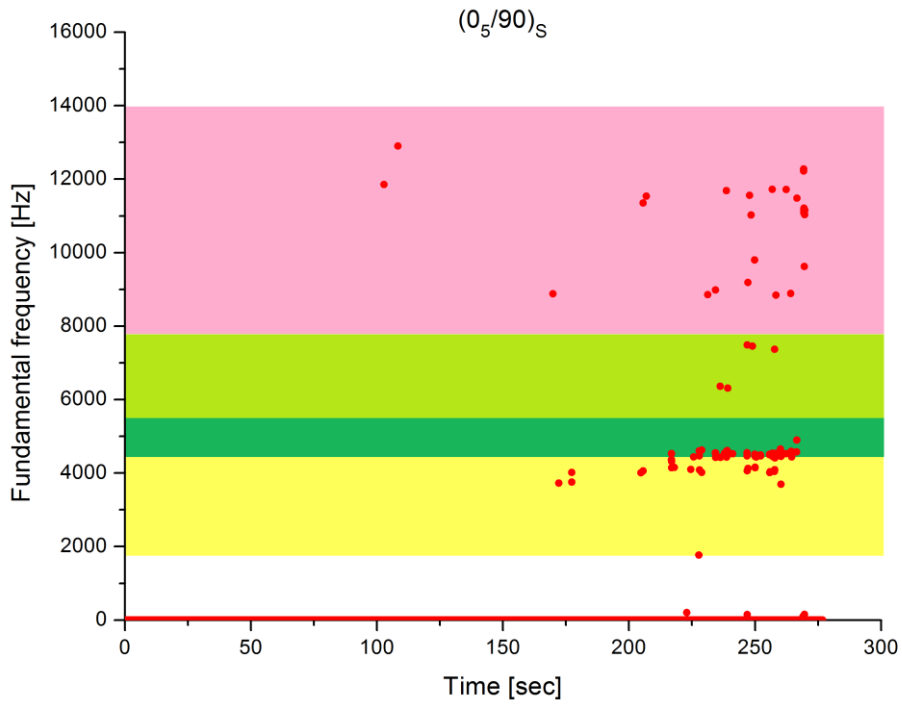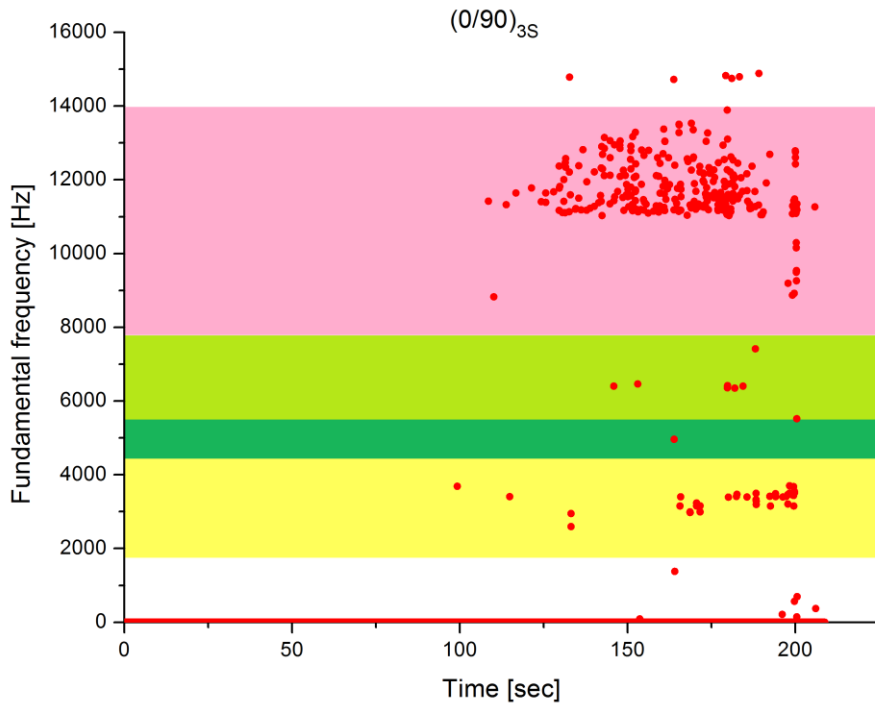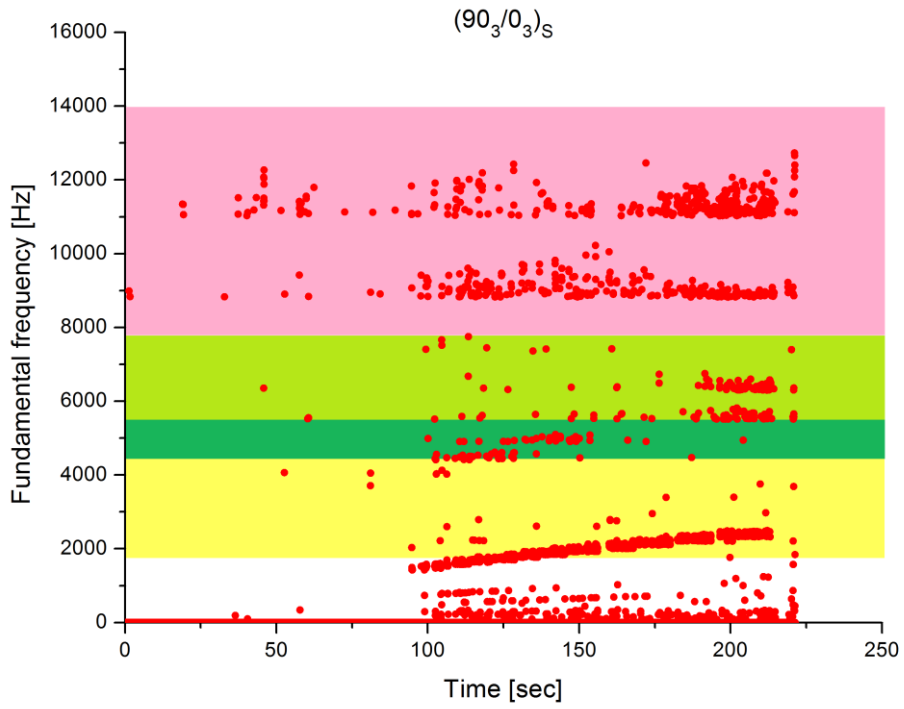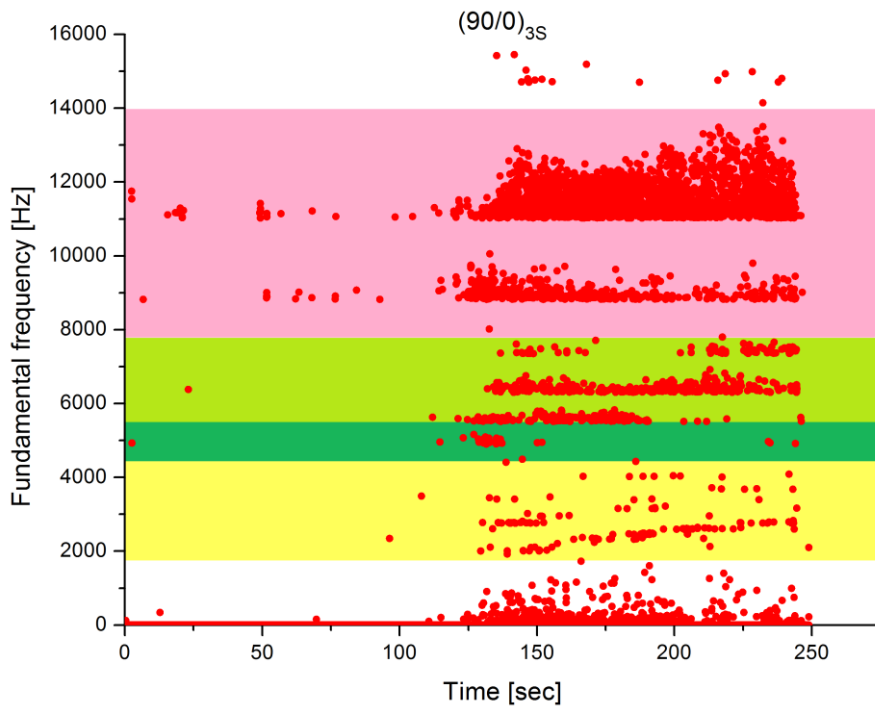Figure 3.29 Time vs. frequency graph for $(90_3/0_3)_S$, color labels are presented according to the classification of [117].
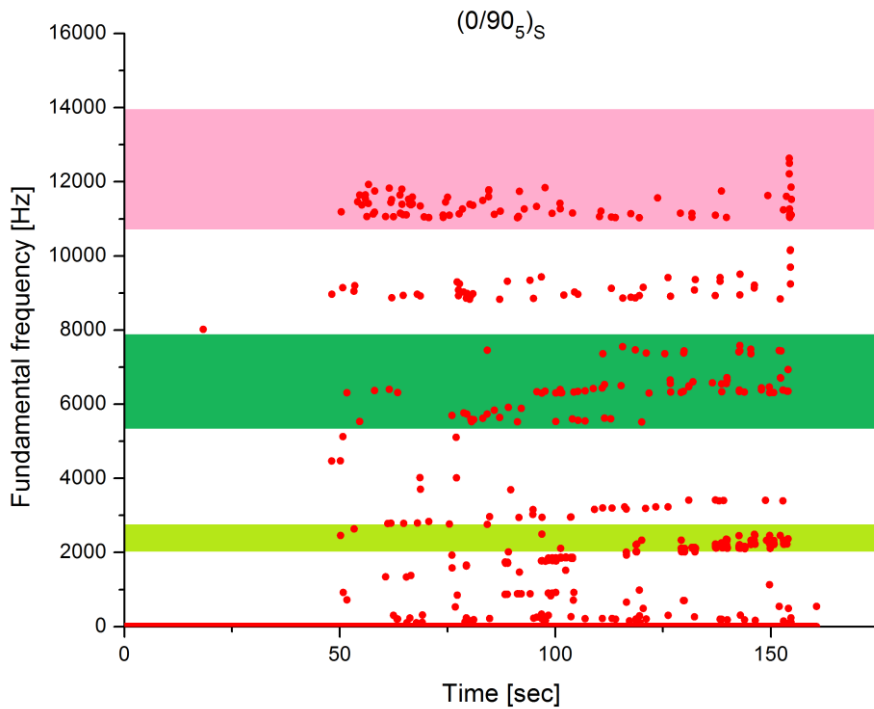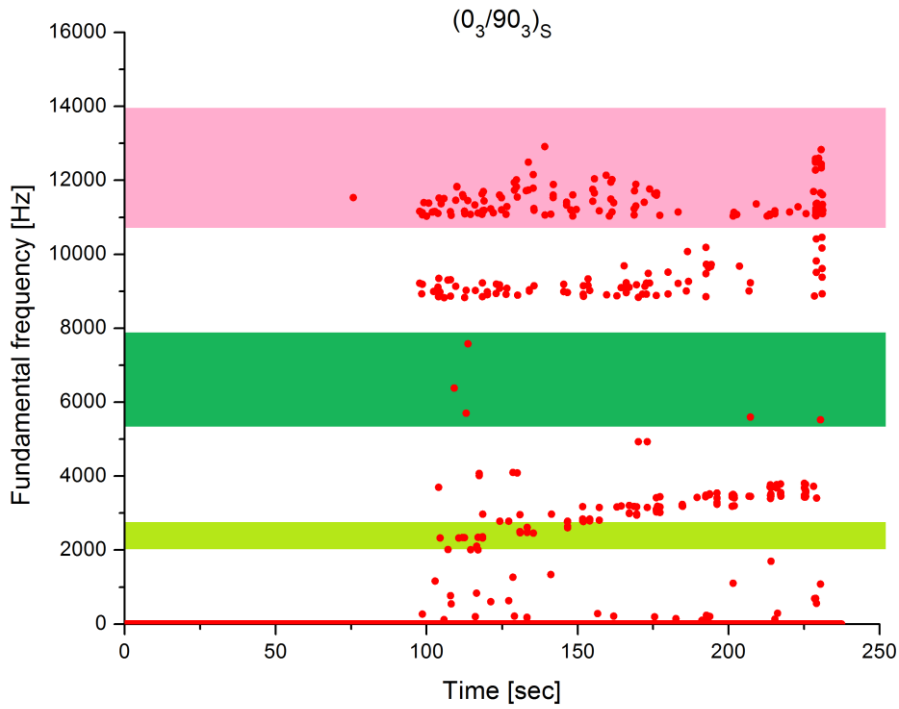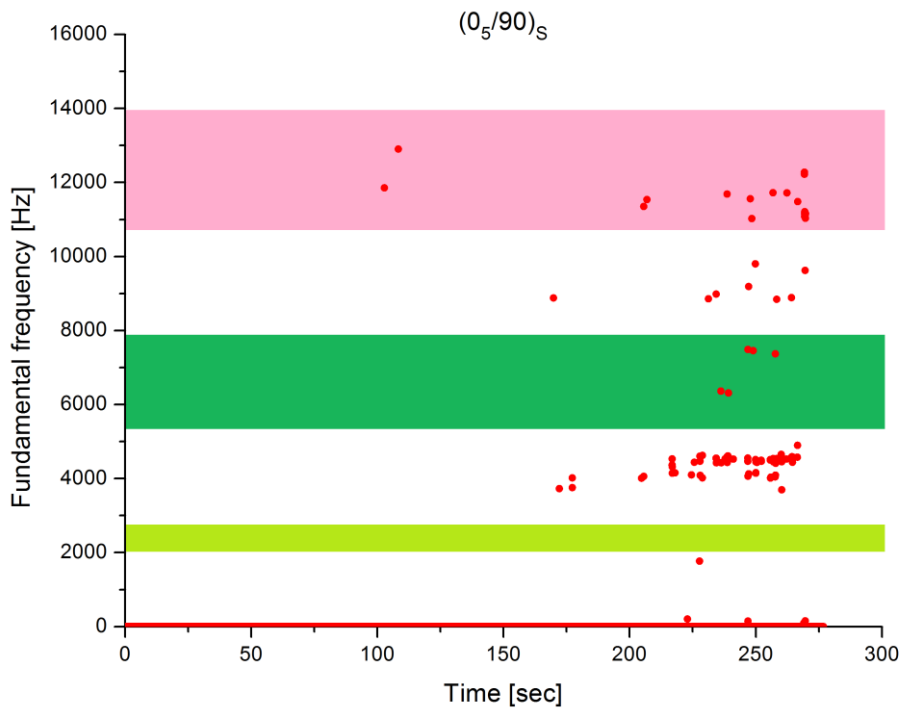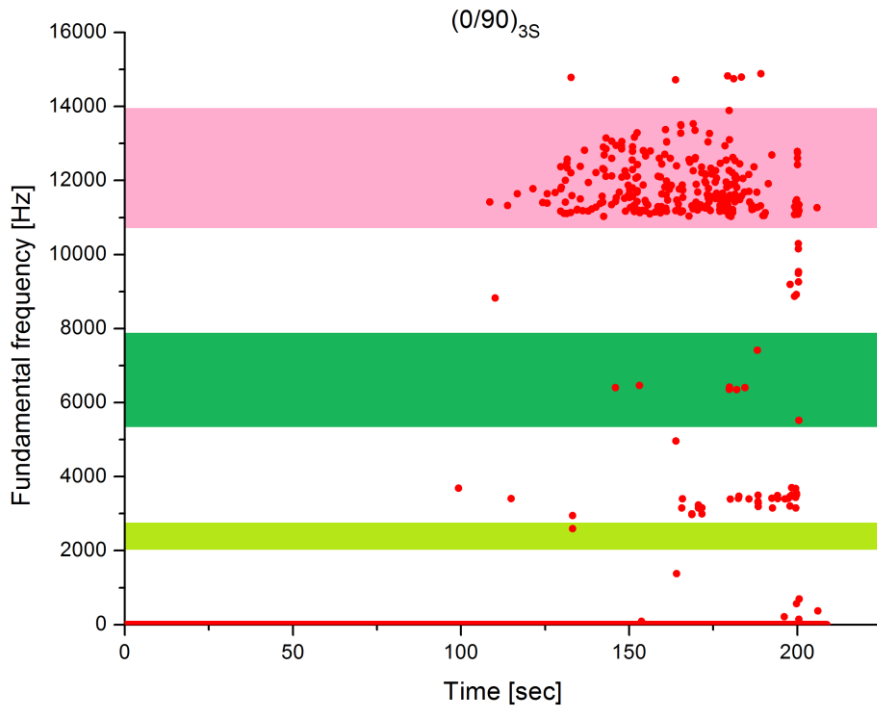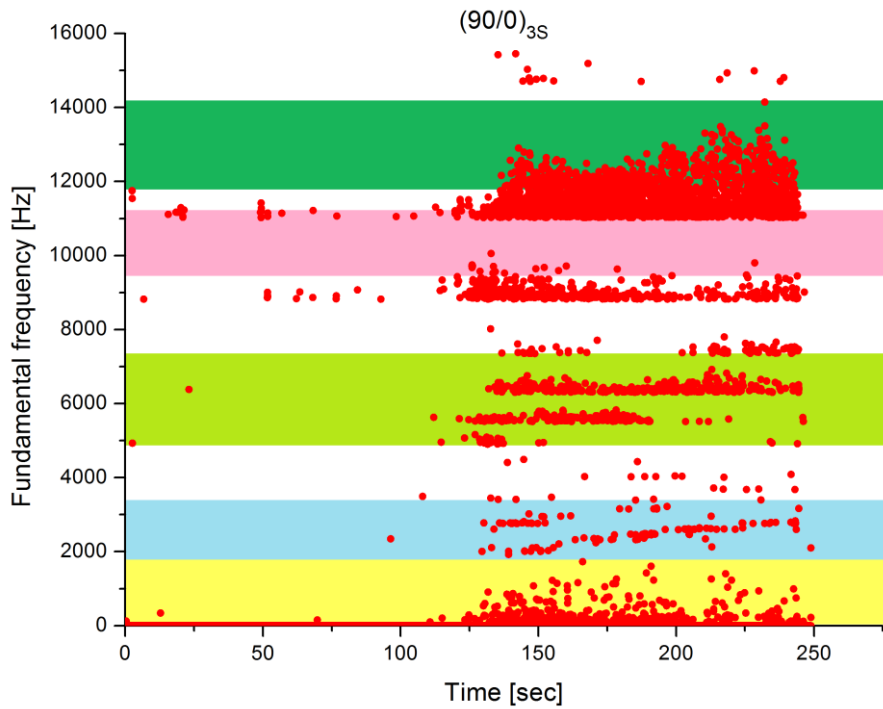

Figure 3.30 Time vs. frequency graph for $(90/0)_{3S}$, color labels are presented according to the classification of [117].

During the ultimate fracture event, several failure events occur simultaneously and instantaneously. So the characterization of this event is prone to confusions both with amplitude and frequency based approaches as also pointed out by [117]. A sound peak with high amplitude corresponds to high-pitched, thin sounds, but the ultimate fracture in our cases is rather explosive. Hence, it created a small amplitude sound. To our knowledge, this issue is also reported for AE systems. The reason why amplitude data is peaked as the primary output response was that it is somewhat a direct measure for human senses. So the proposed approach basically visualizes and gives meaning to the microphone outputs that may also be perceived by the human ear.

3.4   Conclusion

The progressive failure of $(0_m/90_n)_S$ laminates was expertly captured by a microphone assisted sound-tracking approach. Simultaneous video capturing of the polished specimen edges confirmed that the present simplified method is capable of capturing minor, intermediate, major and ultimate failure events as they produce sound fingerprints of their own. Audio and video-assisted mechanical testing of $(0/90_5)_S$, $(0_3/90_3)_S$, $(0_5/90)_S$, $(0/90)_{3S}$, $(90/0)_{3S}$ and $(90_3/0_3)_S$ also demonstrated that the occurrence of the potent failure events and the corresponding sound outputs were significantly dependent on the lay-up sequence. This affordable, easy to set-up and quick method was found to be quite feasible, yet simple, practical and affordable as it provided valuable information, and therefore can be considered in the absence of a sophisticated acoustic emission set-up.

On the other hand in order to categorize the failure modes with frequency analysis, additional case studies should be investigated. The fact that different groups reported different frequency ranges for the distinct fracture event; we believe these comparisons are not conclusive. Arguably the best way to correlate our approach with sophisticated and established AE based data/knowledge would be to repeat the work by also incorporating the AE sensors and simultaneous data collection from the specimens. However, it is to highlight the simplicity and affordability of our methodology which is not to substitute AE when available.

4 CONCLUSIONS AND FUTURE WORK

This thesis is an effort to show the importance of visual and acoustic tracing of composite materials to explain the mechanical behavior. Special effort was given to correlate failure mechanisms and strength with the collected visual and acoustic data.

The first case focused on the influence of meso-structure of composite materials, self-arrangement of fiber bundle packages of different yarn numbers on the mechanical behavior of laminated composites. Particularly, the anomalies, void numbers and misplacement of fiber bundles, of the pre-damaged non-crimp glass fiber-reinforced composites in the micro and mesoscale were reported via micro-computed tomography. Also, the effect of the mesostructure on pre-damage composites containing five different lay-up sequences was evaluated. The relationships among the anomalies, meso-architecture, the mechanical strength, and fracture modes were reported. The effect of yarn number and associated bundle interactions on the tensile behavior of non-crimp fiber reinforced laminates was discussed. Four different yarn numbers, representative of varying fiber linear density as 300, 600, 1200, and 2400 TEX, of glass fiber in the form of unidirectional (UD) non-crimp fabrics (NCF) were studied. In order to investigate the bundle packaging impact on tensile behavior, the laminates at a fixed fiber volume fraction (V_f) containing different stacking sequences of $(0)_8$, $(90)_8$, $(0/90)_{2S}$, $(+45/-45)_{2S}$ and $(0/45/-45/90)_S$ were studied. The meso-architecture of the laminates were analyzed using micro-focus computed tomography (μCT) to further detect the void presence and in-situ deviations from ideal yarn structures (e.g. yarn waviness and crimping). Results revealed that the yarn number is directly affecting the behavior of NCF laminates under tension in terms of bundle/inter bundle size, micro-void presence, waviness, and crimping. In a follow-up of this case study, further investigation can be carried out by a control group of laminae analysis and stacked three-dimensional image analysis via post-processing tools. Also, modelling efforts are

necessary to discuss results further after a three-dimensional image analysis of fiber packages. For a consistent comparison, the perfectly aligned composite materials, containing minumum anomalies, should be studied before and after impregnation. The imperfections due to vacuum infusion in the manufacturing process presents another potential future research topic for the investigation of yarn number effect via μCT imaging technique.

In the second case study, the mechanical behavior of cross-ply like laminated carbon fiber-reinforced composites containing various lay-up sequences was reported. The acoustic signatures were obtained by in-situ sound collection in conjunction with a digital video microscope in order to characterize the progressive failure mechanisms. The progressive failure events during mechanical testing were marked as minor, intermediate, major and ultimate correlated with the unique sound profiles. The amplitude and fundamental frequency properties of acoustic data were reported. For further implications, the combination of AE with the proposed method can be a good study to compare unique sound profiles where failure mode characterization can be based and compared to previous studies.

Overall, it is concluded that non-destructive testing and in-situ monitoring to understand mechanical behavior of the laminated composite materials are very useful and can be incorporated as effective methodology in order to explain complex failure mechanisms of composite materials. This study suggested two different applications to correlate the mechanical behavior of composite materials, namely micro-computed tomography and acoustic data collection. Results of two exemplified cases demonstrated the importance and capabilities of the suggested methodologies.

5 REFERENCES

[1]   A. T. Nettles, "Basic Mechanics of Laminated Composite Plates," *NASA Ref. pulication*, no. October, p. 107, 1994.

[2]   D. Valentin, P. Bonniau, and A. R. Bunsell, "Failure mechanism discrimination in carbon fibre-reinforced epoxy composites," *Composites*, vol. 14, no. 4, pp. 345–351, 1983.

[3]   A. E. Scott, I. Sinclair, S. M. Spearing, M. N. Mavrogordato, and W. Hepples, "Influence of voids on damage mechanisms in carbon/epoxy composites determined via high resolution computed tomography," *Compos. Sci. Technol.*, vol. 90, pp. 147–153, 2014.

[4]   L. Maragoni, P. A. Carraro, and M. Quaresimin, "Effect of voids on the crack formation in a [45/-45/0]s laminate under cyclic axial tension," *Compos. Part A Appl. Sci. Manuf.*, no. June, 2016.

[5]   M. Sugimori and F. Lam, "Macro-void distribution analysis in strand-based wood composites using an X-ray computer tomography technique," *J. Wood Sci.*, vol. 45, pp. 254–257, 1999.

[6]   J. Lambert, A. R. Chambers, I. Sinclair, and S. M. Spearing, "3D damage characterisation and the role of voids in the fatigue of wind turbine blade materials," *Compos. Sci. Technol.*, vol. 72, no. 2, pp. 337–343, 2012.

[7]   S. M. Sisodia, S. C. Garcea, A. R. George, D. T. Fullwood, S. M. Spearing, and E. K. Gamstedt, "High-resolution computed tomography in resin infused woven carbon fibre composites with voids," *Compos. Sci. Technol.*, vol. 131, no. May, pp. 12–21, 2016.

[8]   T. Ponikiewski, J. Katzer, M. Bugdol, and M. Rudzki, "Determination of 3D porosity in steel fibre reinforced SCC beams using X-ray computed tomography," *Constr. Build. Mater.*, vol. 68, pp. 333–340, 2014.

[9]   A. A. Somashekar, S. Bickerton, and D. Bhattacharyya, "Compression deformation of a biaxial stitched glass fibre reinforcement: Visualisation and image analysis using X-ray micro-CT," *Compos. Part A Appl. Sci. Manuf.*, vol. 42, no. 2, pp. 140–150, 2011.

[10]   A. Petriccione *et al.*, "A stiffness volume averaging based approach to model non-crimp fabric reinforced composites," *Compos. Sci. Technol.*, vol. 72, no. 2, pp. 360–369, 2012.

[11]   L. M. Ferreira, E. Graciani, and F. París, "Modelling the waviness of the fibres in non-crimp fabric composites using 3D finite element models with straight tows," *Compos. Struct.*, vol. 107, pp. 79–87, 2014.

[12]   L. K. Jain and Y.-W. Mai, "On the effect of stitching on mode I delamination toughness of laminated composites," *Compos. Sci. Technol.*, vol. 51, no. 3, pp. 331–345, 1994.

[13]   A. E. Bogdanovich, M. Karahan, S. V. Lomov, and I. Verpoest, "Quasi-static tensile behavior and damage of carbon/epoxy composite reinforced with 3D non-crimp orthogonal woven fabric," *Mech. Mater.*, vol. 62, pp. 14–31, 2013.

[14]   A. González, E. Graciani, and F. París, "Prediction of in-plane stiffness properties of non-crimp fabric laminates by means of 3D finite element analysis," *Compos. Sci. Technol.*, vol. 68, no. 1, pp. 121–131, 2008.

[15]   F. Edgren, D. Mattsson, L. E. Asp, and J. Varna, "Formation of damage and its effects on non-crimp fabric reinforced composites loaded in tension," *Compos. Sci. Technol.*, vol. 64, no. 5, pp. 675–692, 2004.

[16]   F. Edgren and L. E. Asp, "Approximate analytical constitutive model for non-crimp fabric composites," *Compos. Part A Appl. Sci. Manuf.*, vol. 36, no. 2 SPEC. ISS., pp. 173–181, 2005.

[17] E. Marklund, L. E. Asp, and R. Olsson, "Transverse strength of unidirectional non-crimp fabric composites: Multiscale modelling," *Compos. Part B Eng.*, vol. 65, pp. 47–56, 2014.

[18] D. Mattsson, R. Joffe, and J. Varna, "Damage in NCF composites under tension: Effect of layer stacking sequence," *Eng. Fract. Mech.*, vol. 75, no. 9, pp. 2666–2682, 2008.

[19] F. Edgren, L. E. Asp, and R. Joffe, "Failure of NCF composites subjected to combined compression and shear loading," *Compos. Sci. Technol.*, vol. 66, no. 15, pp. 2865–2877, 2006.

[20] M. G. R. Sause, "Failure of Fiber-Reinforced Composites," in *In Situ Monitoring of Fiber-Reinforced Composites*, 1st ed., vol. 242, Cham: Springer International Publishing, 2016, pp. 5–55.

[21] K. Bilge, E. Ozden-Yenigun, E. Simsek, Y. Z. Menceloglu, and M. Papila, "Structural composites hybridized with epoxy compatible polymer/MWCNT nanofibrous interlayers," *Compos. Sci. Technol.*, vol. 72, no. 14, pp. 1639–1645, 2012.

[22] K. Bilge, S. Venkataraman, Y. Z. Menceloglu, and M. Papila, "Global and local nanofibrous interlayer toughened composites for higher in-plane strength," *Compos. Part A Appl. Sci. Manuf.*, vol. 58, pp. 73–76, 2014.

[23] K. Bilge and M. Papila, "Interlayer toughening mechanisms of composite materials," in *Toughening Mechanisms in Composite Materials*, Elsevier, 2015, pp. 263–294.

[24] M. Knops, *Analysis of failure in fiber polymer laminates: The theory of alfred puck*. 2008.

[25] A. J. Comer, K. B. Katnam, W. F. Stanley, and T. M. Young, "Characterising the behaviour of composite single lap bonded joints using digital image correlation," *Int. J. Adhes. Adhes.*, vol. 40, pp. 215–223, 2013.

[26] D. Kiefel, R. Stoessel, and C. Grosse, "Quantitative impact characterization of aeronautical CFRP materials with non-destructive testing methods," *41ST Annu. Rev. Prog. Quant. Nondestruct. Eval. Vol. 34*, vol. 1650, pp. 591–598, 2015.

[27] R. Cuntze, *Comparison between experimental and theoretical results using Cuntze's "failure mode concept" model for composites under triaxial loadings- Part B of the second world-wide failure exercise*, vol. 47, no. 6–7. 2013.

[28] S. Gholizadeh, "A review of non-destructive testing of composite materials," *Procedia Struct. Integr.*, vol. 1, pp. 50–57, 2016.

[29] T. Lu, Y. Zhang, H. Li, L. Pan, Y. Li, and Z. Sun, "Electrochemical behaviors of graphene-ZnO and graphene-SnO2 composite films for supercapacitors," *Electrochim. Acta*, vol. 55, no. 13, pp. 4170–4173, 2010.

[30] K. T. Tan, N. Watanabe, and Y. Iwahori, "X-ray radiography and micro-computed tomography examination of damage characteristics in stitched composites subjected to impact loading," *Compos. Part B Eng.*, vol. 42, no. 4, pp. 874–884, 2011.

[31] S. Topal *et al.*, "Late-stage fatigue damage in a 3D orthogonal non-crimp woven composite: An experimental and numerical study," *Compos. Part A Appl. Sci. Manuf.*, vol. 79, pp. 155–163, 2015.

[32] K. Vallons, S. V. Lomov, and I. Verpoest, "Fatigue and post-fatigue behaviour of carbon/epoxy non-crimp fabric composites," *Compos. Part A Appl. Sci. Manuf.*, vol. 40, no. 3, pp. 251–259, 2009.

[33] E. Bayraktar, S. D. Antolovich, and C. Bathias, "New developments in non-destructive controls of the composite materials and applications in manufacturing engineering," *J. Mater. Process. Technol.*, vol. 206, no. 1–3, pp. 30–44, 2008.

[34] H. Heuer and M. H. Schulze, "Eddy Current Testing of Carbon Fiber Materials by High Resolution Directional Sensors," *Proc NDT Canada*, pp. 1–13, 2011.

[35] C. U. Grosse, *Acoustic Emission Testing*. 2008.

[36] N. Godin, S. Huguet, R. Gaertner, and L. Salmon, "Clustering of acoustic emission signals collected during tensile tests on unidirectional glass/polyester composite using supervised and unsupervised classifiers," *NDT E Int.*, vol. 37, no. 4, pp. 253–264, 2004.

[37] M. Surgeon and M. Wevers, "Modal analysis of acoustic emission signals from CFRP laminates," *NDT E Int.*, vol. 32, no. 6, pp. 311–322, 1999.

[38] Y. Feng *et al.*, "Micro-CT characterization on porosity structure of 3D Cf/ SiCm composite," *Compos. Part A Appl. Sci. Manuf.*, vol. 42, no. 11, pp. 1645–1650, 2011.

[39] A. Stamopoulos, K. Tserpes, P. Prucha, and D. Vavrik, "Evaluation of porosity effects on the mechanical properties of carbon fiber-reinforced plastic unidirectional laminates by X-ray computed tomography and mechanical testing," *J. Compos. Mater.*, no. August, p. 0021998315602049-, 2015.

[40] S. M. Sisodia, S. C. Garcea, A. R. George, D. T. Fullwood, S. M. Spearing, and E. K. Gamstedt, "High-resolution computed tomography in resin infused woven carbon fibre composites with voids," *Compos. Sci. Technol.*, vol. 131, pp. 12–21, 2016.

[41] J. Pazmino, V. Carvelli, and S. V. Lomov, "Micro-CT analysis of the internal deformed geometry of a non-crimp 3D orthogonal weave E-glass composite reinforcement," *Compos. Part B Eng.*, vol. 65, pp. 147–157, 2014.

[42] A. Yoshimura, R. Hosoya, and J. Koyanagi, "X-ray computed tomography used to measure fiber orientation in CFRP laminates * Corresponding author X-ray computed tomography used to measure fiber orientation in CFRP laminates," vol. 3046, no. June, 2016.

[43] L. P. Djukic, I. Herszberg, W. R. Walsh, G. A. Schoeppner, B. Gangadhara Prusty, and D. W. Kelly, "Contrast enhancement in visualisation of woven composite tow architecture using a MicroCT Scanner. Part 1: Fabric coating and resin additives," *Compos. Part A Appl. Sci. Manuf.*, vol. 40, no. 5, pp. 553–565, 2009.

[44] J. S. U. Schell, M. Renggli, G. H. van Lenthe, R. Müller, and P. Ermanni,

"Micro-computed tomography determination of glass fibre reinforced polymer meso-structure," *Compos. Sci. Technol.*, vol. 66, no. 13, pp. 2016–2022, 2006.

[45]   P. Badel, E. V. Sallé, E. Maire, and P. Boisse, "Simulation and tomography analysis of textile composite reinforcement deformation at the mesoscopic scale," *Int. J. Mater. Form.*, vol. 2, no. SUPPL. 1, pp. 189–192, 2009.

[46]   L. P. Djukic, G. M. Pearce, I. Herszberg, M. K. Bannister, and D. H. Mollenhauer, "Contrast enhancement of microct scans to aid 3D modelling of carbon fibre fabric composites," *Appl. Compos. Mater.*, vol. 20, no. 6, pp. 1215–1230, 2013.

[47]   S. Kalafat, A.-M. Zelenyak, and M. G. R. Sause, "In-situ monitoring of composite failure by computing tomography and acoustic emission," *20th Int. Conf. Compos. Mater.*, no. October, pp. 1–8, 2015.

[48]   N. Naouar, E. Vidal-Salle, J. Schneider, E. Maire, and P. Boisse, "3D composite reinforcement meso F.E. analyses based on X-ray computed tomography," *Compos. Struct.*, vol. 132, pp. 1094–1104, 2015.

[49]   D. Mattsson, R. Joffe, and J. Varna, "Methodology for characterization of internal structure parameters governing performance in NCF composites," *Compos. Part B Eng.*, vol. 38, no. 1, pp. 44–57, 2007.

[50]   D. G. Aggelis, N.-M. Barkoula, T. E. Matikas, and A. S. Paipetis, "Acoustic structural health monitoring of composite materials : Damage identification and evaluation in cross ply laminates using acoustic emission and ultrasonics," *Compos. Sci. Technol.*, vol. 72, no. 10, pp. 1127–1133, 2012.

[51]   P. J. de Groot, P. A. M. Wijnen, and R. B. F. Janssen, "Real-time frequency determination of acoustic emission for different fracture mechanisms in carbon/epoxy composites," *Compos. Sci. Technol.*, vol. 55, no. 4, pp. 405–412, 1995.

[52]   Y. Mizutani, K. Nagashima, M. Takemoto, and K. Ono, "Fracture mechanism characterization of cross-ply carbon-fiber composites using acoustic emission analysis," *NDT E Int.*, vol. 33, no. 2, pp. 101–110, 2000.

[53]   C. Baker, G. N. Morscher, V. V. Pujar, and J. R. Lemanski, "Transverse cracking in carbon fiber reinforced polymer composites: Modal acoustic emission and peak frequency analysis," *Compos. Sci. Technol.*, vol. 116, pp. 26–32, 2015.

[54]   K. Bilge, "Multi-scale nature of composite materials: three case studies," Sabanci University, 2012.

[55]   E. De Bilbao *et al.*, "Experimental study of bending behaviour of reinforcements To cite this version :," 2011.

[56]   M. Papila, "Design of and with thin-ply non-crimp fabric (NCF) as building blocks for composites," *Sci. Eng. Compos. Mater.*, no. mm, pp. 1–16, 2016.

[57]   K. Dransfield, C. Baillie, and Y.-W. Mai, "Improving the delamination resistance of CFRP by stitching—a review," *Compos. Sci. Technol.*, vol. 50, no. 3, pp. 305–317, 1994.

[58]   K. A. Dransfield, L. K. Jain, and Y.-W. Mai, "On the effects of stitching in CFRPs—I. mode I delamination toughness," *Compos. Sci. Technol.*, vol. 58, no. 6, pp. 815–827, 1998.

[59]   L. K. Jain, K. A. Dransfield, and Y.-W. Mai, "On the effects of stitching in CFRPs—II. Mode II delamination toughness," *Compos. Sci. Technol.*, vol. 58, no. 6, pp. 829–837, 1998.

[60]   K. Vallons, A. Behaeghe, S. V. Lomov, and I. Verpoest, "Impact and post-impact properties of a carbon fibre non-crimp fabric and a twill weave composite," *Compos. Part A Appl. Sci. Manuf.*, vol. 41, no. 8, pp. 1019–1026, 2010.

[61]   S. V. Lomov, E. B. Belov, T. Bischoff, S. B. Ghosh, T. Truong Chi, and I. Verpoest, "Carbon composites based on multiaxial multiply stitched preforms. Part 1. Geometry of the preform," *Compos. Part A Appl. Sci. Manuf.*, vol. 33, no. 9, pp. 1171–1183, 2002.

[62]   S. V. Lomov, I. Verpoest, M. Barburski, and J. Laperre, "Carbon composites based on multiaxial multiply stitched preforms. Part 2. KES-F characterisation of

the deformability of the preforms at low loads," *Compos. Part A Appl. Sci. Manuf.*, vol. 34, no. 4, pp. 359–370, 2003.

[63] S. V. Lomov *et al.*, "Carbon composites based on multiaxial multiply stitched preforms. Part 3: Biaxial tension, picture frame and compression tests of the preforms," *Compos. Part A Appl. Sci. Manuf.*, vol. 36, no. 9, pp. 1188–1206, 2005.

[64] T. C. Truong, M. Vettori, S. Lomov, and I. Verpoest, "Carbon composites based on multi-axial multi-ply stitched preforms. Part 4. Mechanical properties of composites and damage observation," *Compos. Part A Appl. Sci. Manuf.*, vol. 36, no. 9, pp. 1207–1221, 2005.

[65] R. Loendersloot, S. V. Lomov, R. Akkerman, and I. Verpoest, "Carbon composites based on multiaxial multiply stitched preforms. Part V: Geometry of sheared biaxial fabrics," *Compos. Part A Appl. Sci. Manuf.*, vol. 37, no. 1, pp. 103–113, 2006.

[66] K. Vallons, M. Zong, S. V. Lomov, and I. Verpoest, "Carbon composites based on multi-axial multi-ply stitched preforms - Part 6. Fatigue behaviour at low loads: Stiffness degradation and damage development," *Compos. Part A Appl. Sci. Manuf.*, vol. 38, no. 7, pp. 1633–1645, 2007.

[67] T. C. Truong, D. S. Ivanov, D. V. Klimshin, S. V. Lomov, and I. Verpoest, "Carbon composites based on multi-axial multi-ply stitched preforms. Part 7: Mechanical properties and damage observations in composites with sheared reinforcement," *Compos. Part A Appl. Sci. Manuf.*, vol. 39, no. 9, pp. 1380–1393, 2008.

[68] K. Vallons, I. Duque, S. V. Lomov, and I. Verpoest, "Loading direction dependence of the tensile stiffness, strength and fatigue life of biaxial carbon/epoxy NCF composites," *Compos. Part A Appl. Sci. Manuf.*, vol. 42, no. 1, pp. 16–21, 2011.

[69] L. E. Asp, F. Edgren, and S. Anders, "Effects of stitch pattern on the mechanical properties of non-crimp fabric composites," *Eur. Conf. Compos. Mater. ECCM11, Rhodes, Greece*, 2004.

[70] S. Drapier and M. R. Wisnom, "Finite-element investigation of the compressive

strength of non-crimp-fabric-based composites," *Compos. Sci. Technol.*, vol. 59, no. 8, pp. 1287–1297, 1999.

[71] S. Drapier and M. R. Wisnom, "A finite-element investigation of the interlaminar shear behaviour of non-crimp-fabric-based composites," *Compos. Sci. Technol.*, vol. 59, no. 16, pp. 2351–2362, 1999.

[72] H. Heß and N. Himmel, "Structurally stitched NCF CFRP laminates. Part 2: Finite element unit cell based prediction of in-plane strength," *Compos. Sci. Technol.*, vol. 71, no. 5, pp. 569–585, 2011.

[73] L. G. Zhao, N. A. Warrior, and A. C. Long, "Finite element modelling of damage progression in non-crimp fabric reinforced composites," *Compos. Sci. Technol.*, vol. 66, no. 1, pp. 36–50, 2006.

[74] S. Bel, N. Hamila, P. Boisse, and F. Dumont, "Finite element model for NCF composite reinforcement preforming: Importance of inter-ply sliding," *Compos. Part A Appl. Sci. Manuf.*, vol. 43, no. 12, pp. 2269–2277, 2012.

[75] S. Bel, P. Boisse, and F. Dumont, "Analyses of the deformation mechanisms of non-crimp fabric composite reinforcements during preforming," *Appl. Compos. Mater.*, vol. 19, no. 3–4, pp. 513–528, 2012.

[76] P. Tan, L. Tong, and G. . Steven, "Modelling for predicting the mechanical properties of textile composites—A review," *Compos. Part A Appl. Sci. Manuf.*, vol. 28, no. 11, pp. 903–922, 1997.

[77] R. Böhm *et al.*, "A quantitative comparison of the capabilities of in situ computed tomography and conventional computed tomography for damage analysis of composites," *Compos. Sci. Technol.*, vol. 110, pp. 62–68, 2015.

[78] D. J. Bull, L. Helfen, I. Sinclair, S. M. Spearing, and T. Baumbach, "A comparison of multi-scale 3D X-ray tomographic inspection techniques for assessing carbon fibre composite impact damage," *Compos. Sci. Technol.*, vol. 75, pp. 55–61, 2013.

[79] A. Stamopoulos, K. Tserpes, P. Prucha, and D. Vavrik, "Evaluation of porosity

effects on the mechanical properties of carbon fiber-reinforced plastic unidirectional laminates by X-ray computed tomography and mechanical testing," *J. Compos. Mater.*, p. 0021998315602049-, 2015.

[80]   J. Kastner, B. Plank, D. Salaberger, and J. Sekelja, "Defect and Porosity Determination of Fibre Reinforced Polymers by X-ray Computed Tomography," *NDT Aerosp. 2010 - We.1.A.2*, pp. 1–12, 2010.

[81]   F. Desplentere, S. V. Lomov, D. L. Woerdeman, I. Verpoest, M. Wevers, and A. Bogdanovich, "Micro-CT characterization of variability in 3D textile architecture," *Compos. Sci. Technol.*, vol. 65, no. 13, pp. 1920–1930, 2005.

[82]   A. E. Scott, M. Mavrogordato, P. Wright, I. Sinclair, and S. M. Spearing, "In situ fibre fracture measurement in carbon-epoxy laminates using high resolution computed tomography," *Compos. Sci. Technol.*, vol. 71, no. 12, pp. 1471–1477, 2011.

[83]   A. E. E. Scott, I. Sinclair, S. M. M. Spearing, M. Mavrogordato, A. R. Bunsell, and A. Thionnet, "Comparison of the accumulation of fibre breaks occurring in a carbon/epoxy composite identified in a multi-scale micro-mechanical model with that of experimental observations using high resolution computed tomography," in *Actes Matériaux 2010*, 2010.

[84]   T. Allen, A. E. Scott, W. Hepples, S. M. Spearing, P. A. Reed, and I. Sinclair, "Investigating damage resistance of hybrid composite-metallic structures using multi-scale computed tomography," in *16th European Conference on Composite Materials, ECCM 2014*, 2014.

[85]   P. J. Schilling, B. R. Karedla, A. K. Tatiparthi, M. A. Verges, and P. D. Herrington, "X-ray computed microtomography of internal damage in fiber reinforced polymer matrix composites," *Compos. Sci. Technol.*, vol. 65, no. 14, pp. 2071–2078, 2005.

[86]   A. J. Moffat, P. Wright, J. Y. Buffiere, I. Sinclair, and S. M. Spearing, "Micromechanisms of damage in 0 degrees splits in a 90/0 (s) composite material using synchrotron radiation computed tomography," *Scr. Mater.*, vol. 59, no. 10, pp. 1043–1046, 2008.

[87]   P. Wright, A. Moffat, I. Sinclair, and S. M. Spearing, "High resolution

tomographic imaging and modelling of notch tip damage in a laminated composite," *Compos. Sci. Technol.*, vol. 70, no. 10, pp. 1444–1452, 2010.

[88]   P. Wright, A. Moffat, A. Renault, I. Sinclair, and S. M. Spearing, "High resolution computed tomography for modelling laminate damage," *Proc. ...*, 2009.

[89]   P. Wright Fu, X., Sinclair, I., Spearing, S.M., P. Wright, X. Fu, I. Sinclair, and S. M. Spearing, "Ultra high resolution computed tomography of damage in notched carbon fiber-epoxy composites," *J. Compos. Mater.*, vol. 42, no. 19, pp. 1993–2002, 2008.

[90]   L. a. Feldkamp, L. C. Davis, and J. W. Kress, "Practical cone-beam algorithm," *J. Opt. Soc. Am. A*, vol. 1, no. 6, p. 612, 1984.

[91]   R. Kandwal, A. Kumar, and S. Bhargava, "Review: Existing Image Segmentation Techniques," *Int. J. Adv. Res. Comput. Sci. Softw. Eng.*, vol. 4, no. 4, pp. 153–156, 2014.

[92]   M. L. Bouxsein, S. K. Boyd, B. A. Christiansen, R. E. Guldberg, K. J. Jepsen, and R. Müller, "Guidelines for assessment of bone microstructure in rodents using micro-computed tomography," *Journal of Bone and Mineral Research*, vol. 25, no. 7. pp. 1468–1486, 2010.

[93]   A. Odgaard, "Three-dimensional methods for quantification of cancellous bone architecture," *Bone*, vol. 20, no. 4, pp. 315–328, 1997.

[94]   A. Odgaard, J. Kabel, B. Van Rietbergen, M. Dalstra, and R. Huiskes, "Fabric and elastic principal directions of cancellous bone are closely related," *J. Biomech.*, vol. 30, no. 5, pp. 487–495, 1997.

[95]   ASTM INTERNATIONAL, "Astm D3039/D3039M," *Annu. B. ASTM Stand.*, pp. 1–13, 2014.

[96]   International Organization for Standardization, "ISO Standards - ISO," *[Company Website]*. 2014.

[97] P. P. Camanho, C. G. Dávila, S. T. Pinho, L. Iannucci, and P. Robinson, "Prediction of in situ strengths and matrix cracking in composites under transverse tension and in-plane shear," *Compos. Part A Appl. Sci. Manuf.*, vol. 37, no. 2, pp. 165–176, 2006.

[98] Z. C. Xia, R. R. Carr, and J. W. Hutchinson, "Transverse cracking in fiber-reinforced brittle matrix, cross-ply laminates," *Acta Metall. Mater.*, vol. 41, no. 8, pp. 2365–2376, 1993.

[99] J. Tong, F. J. Guild, S. L. Ogin, and P. A. Smith, "ON MATRIX CRACK GROWTH IN QUASI-ISOTROPIC LAMINATES-I. EXPERIMENTAL INVESTIGATION," *Compos. Sci. Technol. Elsevier Sci. Ltd.*, vol. 57, no. 97, pp. 1527–1535, 1997.

[100] N. Takeda and S. Ogihara, "In situ observation and probabilistic prediction of microscopic failure processes in CFRP cross-ply laminates," *Compos. Sci. Technol.*, vol. 52, no. 2, pp. 183–195, 1994.

[101] N. Takeda and S. Ogihara, "Initiation and growth of delamination from the tips of transverse cracks in CFRP cross-ply laminates," *Compos. Sci. Technol.*, vol. 52, no. 3, pp. 309–318, 1994.

[102] J.-M. Berthelot, "Transverse cracking and delamination in cross-ply glass-fiber and carbon-fiber reinforced plastic laminates: Static and fatigue loading," *Appl. Mech. Rev.*, vol. 56, no. 1, pp. 111–147, 2003.

[103] S. Ogihara and N. Takeda, "Interaction between transverse cracks and delamination during damage progress in CFRP cross-ply laminates," *Compos. Sci. Technol.*, vol. 54, no. 4, pp. 395–404, 1995.

[104] P. JOHNSON and F.-K. CHANG, "Characterization of Matrix Crack-Induced Laminate Failure-Part I: Experiments," *J. Compos. Mater.*, vol. 35, no. 22, pp. 2009–2035, 2001.

[105] P. Johnson and F.-K. Chang, "Characterization of Matrix Crack-Induced Laminate Failure-Part II: Analysis and Verifications," *J. Compos. Mater.*, vol. 35, no. 22, pp. 2037–2074, 2001.

[106] E. Greenhalgh, M. Hiley, and C. Meeks, "Failure Analysis and Fractography of Polymer Composites," *Analysis*, no. March, p. 595, 2010.

[107] F. Aymerich and S. Meili, "Ultrasonic evaluation of matrix damage in impacted composite laminates," *Compos. Part B Eng.*, vol. 31, no. 1, pp. 1–6, 2000.

[108] G. J. Dvorak and N. Laws, "Analysis of Progressive Matrix Cracking In Composite Laminates II. First Ply Failure," *J. Compos. Mater.*, vol. 21, no. 4, pp. 309–329, 1987.

[109] T. E. Tay, G. Liu, V. B. C. Tan, X. S. Sun, and D. C. Pham, "Progressive Failure Analysis of Composites," *J. Compos. Mater.*, vol. 42, no. 18, pp. 1921–1966, 2008.

[110] K. C. Jen and C. T. Sun, "Matrix Cracking and Delamination Prediction in Graphite/Epoxy Laminates," *J. Reinf. Plast. Compos.*, vol. 11, no. 10, pp. 1163–1175, 1992.

[111] K. Bilge, B. Yilmaz, and M. Papila, "Sound-tracking of failure events in cross-ply composite laminates under tension," 2016.

[112] L. Zubillaga, A. Turon, J. Renart, J. Costa, and P. Linde, "An experimental study on matrix crack induced delamination in composite laminates," *Compos. Struct.*, vol. 127, pp. 10–17, 2015.

[113] J. G. Proakis and D. G. Monolakis, "Digital signal processing: principles, algorithms, and applications," *Pentice Hall*, pp. 1–42, 1996.

[114] C. R. Ramirez-Jimenez, N. Papadakis, N. Reynolds, T. H. Gan, P. Purnell, and M. Pharaoh, "Identification of failure modes in glass/polypropylene composites by means of the primary frequency content of the acoustic emission event," *Compos. Sci. Technol.*, vol. 64, no. 12, pp. 1819–1827, 2004.

[115] C. Cannam, C. Landone, and M. Sandler, "Sonic Visualiser : An Open Source Application for Viewing, Analysing, and Annotating Music Audio Files," in *Proceedings of the ACM Multimedia 2010 International Conference*, 2010, pp. 1467--1468.

[116] D. G. Aggelis, N. M. Barkoula, T. E. Matikas, and a S. Paipetis, "Acoustic emission monitoring of degradation of cross ply laminates.," *J. Acoust. Soc. Am.*, vol. 127, no. 6, p. EL246-L251, 2010.

[117] R. Gutkin, C. J. Green, S. Vangrattanachai, S. T. Pinho, P. Robinson, and P. T. Curtis, "On acoustic emission for failure investigation in CFRP: Pattern recognition and peak frequency analyses," *Mech. Syst. Signal Process.*, vol. 25, no. 4, pp. 1393–1407, 2011.

[118] J. M. Berthelot and J. Rhazi, "Acoustic Emission in Carbon Fibre Composites," *Compos Sci Technol*, vol. 37, pp. 411–428, 1990.

[119] S. Granger, A. Loukili, G. Pijaudier-Cabot, and G. Chanvillard, "Experimental characterization of the self-healing of cracks in an ultra high performance cementitious material: Mechanical tests and acoustic emission analysis," *Cem. Concr. Res.*, vol. 37, no. 4, pp. 519–527, 2007.

[120] M. Ohtsu, "A review of acoustic emission in civil engineering with emphasis on concrete," *J. Acoust. Emiss.*, vol. 8, no. 4, pp. 93–98, 1989.